NUMERICAL STUDY FOR THE DESIGN OF A FLUIDIZED BED REACTOR FOR BIOMASS GASIFICATION

FREDRICK IRUNGU NJUGUNA

DOCTOR OF PHILOSOPHY

(Mechanical Engineering)

JOMO KENYATTA UNIVERSITY

OF

AGRICULTURE AND TECHNOLOGY

2024

Numerical Study for the Design of a Fluidized Bed Reactor for Biomass Gasification

Fredrick Irungu Njuguna

A Thesis Submitted in Partial Fulfillment of the Requirements for the Degree of Doctor of Philosophy in Mechanical Engineering of the Jomo Kenyatta University of Agriculture and Technology

2024

DECLARATION

This thesis is my original work and has not been presented for a degree in any other university.

Signature ....Date ....

Fredrick Irungu Njuguna

This thesis has been submitted for examination with our approval as the university supervisors.

Signature ....Date ....

Dr. (Eng.) Hiram M. Ndiritu, PhD
JKUAT, Kenya

Signature ....Date ....

Dr. Benson B. Gathitu, PhD
JKUAT, Kenya

Signature ....Date ....

Dr. Meshack Hawi, PhD
JKUAT, Kenya

Signature ....Date ....

Dr. Jotham M. Munyalo, PhD
JKUAT, Kenya

DEDICATION

To my wife, our children, my parents, and my siblings

ACKNOWLEDGEMENT

I would like to recognize the Almighty God for His grace and sustenance that enabled me to carry out this research. I express my sincere gratitude to my supervisors Dr. (Eng.) Hiram Ndiritu, Dr. Benson Gathitu, Dr. Meshack Hawi, and Dr. Jotham Munyalo for their invaluable guidance, mentorship, and outstanding leadership throughout my research journey. The technical team at the JKUAT mechanical engineering workshops provided great assistance, and I extend my special thanks to Mr. Joseph Muigai and Mr. Erick Waiyaki of Thermodynamics Lab, as well as Mr. David Chitayi of the Welding Workshop, for their invaluable support.

I am also deeply grateful to German Academic Exchange Service (DAAD) for awarding me the scholarship that enabled me to study at JKAUT. Additionally, I would like to express my appreciation to Japan International Cooperation Agency (JICA) through AFRICA-ai-JAPAN Project for their financial support, which played a crucial role in conducting the experimental work.

Lastly, I would like to express my heartfelt thanks to my parents and siblings for their unwavering support throughout my academic journey. A special appreciation goes to my beloved wife, Teresia, for her patience and understanding during the entire period of my study. Finally, I would like to acknowledge my children for their unconditional love and unwavering support.

TABLE OF CONTENTS

LIST OF TABLES

LIST OF FIGURES

LIST OF APPENDICES

ACRONYMS AND ABBREVIATIONS

ANOVA	Analysis of Variance
BFB	Bubbling Fluidized Bed
CFB	Circulating Fluidized Bed
CFD	Computational Fluid Dynamics
CV	Calorific Value
DB	Dry Basis
DEM	Discrete Element Method
DOE	Design of Experiment
ER	Equivalence Ratio
FBG	Fluidized Bed Gasifier
GCV	Gross Calorific Value
HHV	Higher Heating Value (MJ/Nm^3)
IEA	International Energy Agency
KM	Kinetic Modeling
KTGF	Kinetic Theory Of Granular Flow
LCV	Lower Calorific Value
MAE	Mean Absolute Error
PAH	Polycyclic Aromatic Hydrocarbons
PID	Proportional Integral Derivative
RMSE	Root Mean Square Error
RNG	Re-Normalization Group
RSM	Response Surface Methodology
TDH	Total Disengaging Height
TEM	Thermodynamic Equilibrium Modeling
TFM	Two Fluid Model
VOF	Volume Of Fraction

LIST OF SYMBOLS

Ar	Archimedes Number
$\boldsymbol{\sigma}$	Total Uncertainty
$\boldsymbol{\beta_o}$	Regression Coefficient for Intercept
$\boldsymbol{\beta_i}$	Linear Regression Coefficient
$\boldsymbol{\beta_{ii}}$	Quadratic Regression Coefficient
$\boldsymbol{\beta_{ij}}$	Interaction Terms
$\boldsymbol{\phi}$	Residual
$\mathbf{AF_{act}}$	Actual Air-Fuel Ratio
$\mathbf{AF_{stoich}}$	stoichiometric Air-Fuel Ratio
ar	As Received
Bxi	Systematic Uncertainty
C	Carbon
$\mathbf{CH_4}$	Methane
CO	Carbon Monoxide
$\mathbf{CO_2}$	Carbon Dioxide
dp	Particle Diameter
H	Hydrogen
$\mathbf{H_2}$	Hydrogen Gas
$\mathbf{H_2O}$	Water

mf	Biomass Flow Rate (kg/h)
Q	Air flow Rate (kg/h)
y	Syngas Yield (Nm^3/kg)
z	Regression Model Output Response
σs	Surface Tension of the Solid (N/m)
k_{gs}	Drag function
g_0	Radial Distribution Function
h_i	Enthalpy (kg m^2 s^2)
I	Unit Tensor
Kgs	Interphase Momentum Exchange Coefficient
K_i	Kinetic Energy (kg m^2 s^2)
Ps,f	Particle Frictional Pressure (Pa)
Re	Reynolds Number
t	Time (s)
T	Transpose
α_{eff}	Effective Thermal Diffusivity (kg m^2 s^2)
ΔP	ΔP Pressure Drop (Pa)
Δt	Δt Time step (s^{-1})
Δx	Δx Cell size (m)

Ur	Relative Velocity Through the Cell (m s^{-1})
φ_{gs}	Fluctuating Interphase Energy (kg m^{2} s^{2})
μ	Air viscosity (Kg m^{1} s^{-1})
μ_{g}	Gas Viscosity (Kg m^{1} s^{-1})
μ_{s}	Solid Shear Viscosity (Kg m^{1} s^{-1})
$\mu_{s,f}$	Particle Frictional Viscosity (Pa.S)
λ_{p}	Solid Bulk Viscosity (Kg m^{1} s^{-1})
ν_{g}	Velocity of Gas Phase (m s^{-1})
ν'_{g}	Gas Velocity Fluctuations (m s^{-1})
ν'_{s}	Particle Velocity Fluctuations m s^{-1})
θ	Granular Temperature (m^{2} s^{-2})
Φ	Specularity Coefficient
ϕ	Internal Frictional Angle

ABSTRACT

In biomass waste gasification, raw atmospheric air is commonly used as the gasification agent due to its affordability and availability. This leads to syngas with a low heating value and high tar content, limiting its industrial application. While fluidized bed gasifiers are the prefered gasification technology due to their enhanced heat and mass transfer rates, experimenally investigating their hydrodynamic parameters and optimizing the gasification process is challenging. The high temperatures involved, reaching of up to 1000 ^{o}C, complicate fluidized bed experiments, making numerical simulations valuable for such investigations. Existing simulation models are tailored for room temperature, rendering them inadequate for high-temperature applications. This study aimed to numerically investigate the fluidized bed hydrodynamics at high temperatures and optimize the gasification process to maximize syngas quality while reducing the amount of tar. The first part of the study investigated fluidized bed hydrodynamics at high temperatures. Computational fluid dynamics simulations were conducted using OpenFOAM. A 3D model based on the Eulerian-Eulerian approach was developed. Inert sand particles of three sizes (233, 335, and 500 μm) were used as the bed material, with temperatures ranging from 25 to 400 ^{o}C. The simulation results were validated using experiments conducted in a laboratory-scale fluidized bed unit under the same temperature and particle size range. It was found that the temperature of the bed materials significantly affected the fluidized bed hydrodynamics. Increasing the temperature from 25 to 400 °C led to a 40 % decrease in the minimum fluidization velocity, while increasing the particle size from 233 to 500 μm resulted in a 61 % increase in the the minimum fluidization velocity. Additionally, the bed porosity at the minimum fluidization point increased by 4.6 % while the bed height increased by 17 % over the same temperature range. The simulation results were in good agreement with the experimental results, with a percentage mean absolute error of 6.1 %. The second part of the study was a sensitivity analysis on the effect of gasification input variables on the gasifier outputs using Aspen Plus. The optimal ranges for the equivalence ratio, air preheating temperature, and gasifier pressure were 0.15-0.33, 25-625 ^{o}C, and 1-4 atm, respectively. A multi-objective optimization using the Box-Behnken design response surface methodology was then conducted within these optimal ranges to maximize syngas composition and higher heating value while minimizing tar. The analysis of variance revealed that the equivalence ratio had the most impact on hydrogen and methane production, higher heating value, and tar content, while pressure had the least influence. Conversely, air temperature was the most influential factor in carbon dioxide production, whereas the equivalence ratio had the least effect. Two optimal solutions were obtained for gasifiers. The first solution is a pressurized gasifier, operating at 4 atm.The optimal values for hydrogen, carbon monoxide, methane, higher heating value, and tar were 11.41 %, 14.41 %, 2.19 %, 4.30 MJ/Nm^3, and 23.68 g/Nm^3, respectively. The most optimized points for the equivalence ratio and air temperature were 0.16 and 575 °C, respectively. The second solution is an atmospheric gasifier, operating at 1 atm. The optimal values for hydrogen, carbon monoxide, methane, higher heating value, and tar were 10.07 %, 14.52 %, 2.21 %, 4.14 MJ/Nm^3, and 29.17 g/Nm^3, respectively. The most optimized points for the equivalence ratio and air temperature were 0.15 and 445 °C, respectively. This study provides valuable insights into fluidized bed hydrodynamics and the optimization of gasification processes parameters. The developed models offer practical guidelines for selecting optimal gasifier conditions to maximize syngas energy density and minimize tar content.

CHAPTER ONE

INTRODUCTION

1.1 Background

The depletion of fossil fuels and the heightened emissions regulations have spurred interest in renewable energy sources to stimulate economic growth. Biomass accounts for more than 70 % of renewable energy production and contributes up to 10-15 % of the energy supplied globally (IEA, 2019). Biomass applies to any carbonaceous material that can be converted into useful energy through appropriate technology. It is classified into two categories: forestry biomass such as woodchips, bark and sawdust, and agricultural residue and industrial byproducts such as rice husk, macadamia nutshells, straw and bagasse (Bhattacharya and Abdul Salam, 2002).

Biomass waste has a huge potential as a sustainable energy source due to its ability to be regrown and replenished within a relatively short period, making it a good alternative to fossil fuels (Mohammed et al., 2011). In many developing countries, where access to traditional energy sources is limited, meeting energy demands is a considerable challenge. However, biomass offers a practical solution by providing a locally available and cost-effective energy resource that can be utilized sustainably (Gómez-Barea and Leckner, 2010).

The global production of biomass is estimated at 146 billion metric tons annually. Approximately 14 million metric tons of biomass waste are generated annually in Kenya, which are primarily used for household cooking and as fuel for industrial boilers (Njogu et al., 2015). However, the traditional combustion of biomass waste poses significant risks to human health and environmental degradation. Poor combustion efficiency leads to the emission of particulate matter, volatile organic compounds, and carbon monoxide, contributing to indoor air pollution (F. I. Njuguna et al., 2023). Chronic exposure to biomass smoke from uncontrolled combustion has been associated with health issues such as chronic obstructive pulmonary disease and interstitial lung disease. Furthermore, biomass combustion releases air pollutants like polycyclic aromatic hydrocarbons (PAH), known to cause adverse health effects including cancer, kidney, and liver damage. (Sengupta et al., 2023).

Gasification technology has emerged as a highly effective waste to energy approach for biomass and a feasible option for managing solid waste. In gasification process, biomass waste is subjected to high temperatures ranging from 600 °C to 1000 °C, under controlled combustion conditions with air or oxygen, resulting in the production of a gas mixture known as syngas (Saleh and Samad, 2021). Syngas is a versatile fuel that can be utilized generate electricity (Saleh and Samad, 2021).

Generally, gasifiers are classified as either fixed or fluidized bed gasifiers. Fluidized bed gasifiers are preferred for their high efficiency and ability to produce syngas with low tar content. They offer enhanced heat transfer rates and mixing capabilities compared to fixed bed gasifiers (Samiran et al., 2016). In fluidized bed gasifiers, inert bed materials like sand or alumina facilitate heat transfer to fuel particles, and is particularly useful for low-density biomass fuels (Ostermeier et al., 2019). The fluidization process involves intricate gas-solid and solid-solid interactions, making the investigation of fluidized bed hydrodynamic parameters complex. These parameters, which include bed porosity, minimum fluidization velocity, and bubble size, are crucial in the design of fluidized bed systems because they affect mass and heat transfer and the rate of gasification reactions (Loha et al., 2012).

This research focused on gasification of macadamia nutshells using fluidized bed gasifiers. Macadamia nutshells, an agricultural biomass byproduct, represent a plentiful yet underexploited resource for sustainable energy production. The interest in harnessing biomass waste for energy is particularly high in developing nations, where the economies are based on agriculture (Al-Farraji, 2017).

1.2 Macadamia Nutshells

Macadamia nuts constitutes a small sub-sector of all nuts in the world, contributing about 1.28% of the total nut production, although the production continues to increase attributed to increasing world demand. Production of macadamia nuts has shown a steady growth of 218 % over ten years, between 2009 and 2019 (Linh et al., 2021).

Australia and South Africa are the biggest producers of macadamia nuts globally, each holding an estimated market share of 27 %. On the other hand, Kenya ranks as the third-largest producer, with a market share of 13 %. based on kernel production, as shown in Table 1.1 (Bandason et al., 2022).

Table 1.1: Global Macadamia Production

Country	Metric tons (Kernel based)	Share (%)
South Africa	14,288	27
Australia	14, 192	27
Kenya	7,002	13
USA	4,153	8
China	3,859	7
Guatemala	2,190	4
Malawi	1,620	3
Brazil	1,450	3
Others	4,172	8

Macadamia nuts are cultivated as cash crop in various regions of Kenya, with significant production taking place in Central Kenya. As of 2023, the country had an estimated cultivation area of macadamia spanning 8,746 hectares, a 22 % increase from 7,180 hectares reported in 2021 (AFA, 2021). This rapid expansion raises potential issues related to macadamia waste in production areas. The nuts are enclosed in rigid, woody shells, which become waste after processing.

Macadamia nutshells production was approximated at 42,562 tons from the latest nuts and oils statistics of 2021 (AFA, 2021). Currently, the sustainable utilization of macadamia nutshells is limited, leading to significant environmental impact due to the large volume of waste generated. These wastes are used in both domestic and industrial setups for various applications.

In Kenyan homes, macadamia nutshells are used to generate heat for cooking, often utilizing traditional stoves. Other domestic uses include allowing the waste to decompose naturally to produce manure for farm use. Additionally, macadamia nutshells have been converted into charcoal briquettes through carbonization, providing an alternative fuel source (Linh et al., 2021).

In the agro-processing industries, macadamia nutshells are harnessed through combustion and incineration to generate heat for various industrial applications, such as boiler operations. Recently, the shells have also been used to produce activated carbon, which is employed in water filtration and air purification systems (Kabir Ahmad et al., 2022a).

Although innovative uses of macadamia nutshells are emerging, their conventional use through combustion remains the predominant method. This presents serious environmental issues due to the production of emissions that are harmful to human health. If not utilized, the waste accumulates, contributing to environmental pollution due to its phytotoxic nature (Al-Farraji, 2017).

Kenya, like other developing countries, needs to exploit available energy resources for sustainable national development. Currently, Kenya primarily depends on imported oil and gas for its power needs, leading to increased emissions associated with fossil fuels. This situation calls for accelerated research into using the available biomass waste as an alternative energy source for sustainable energy production. Table 1.2 presents a comparison of physio-chemical properties of various biomass wastes produced by agro-processing companies.

Table 1.2: Macadamia Nutshells Physiochemical Propeties

Biomass waste	**Component**				**Region**
	Volatile matter (wt %)	**Fixed carbon (wt %)**	**Ash (wt %)**	**Energy density (Mj/kg)**	
Coconut shell	70.82	21.80	1.80	19.4	Coast
Saw dust	70.30	25.00	2.70	15.9	Countrywide
Macadamia nutshells	70.64	21.68	0.33	19.26	Central
Rice husk	65.33	10.04	24.63	13.8	Central
Sugarcane Bagasse	82.55	8.30	3.90	16.9	Western, Nyanza

Source: (Kabir Ahmad et al., 2022a)

Macadamia nutshells exhibit a favorable combination of high volatile matter and low ash content, as evidenced in Table 1.2. Presence of a huge amount of volatile matter is essential for generating pyrolysis gas and enables subsequent oxidation and reduction reactions (Kabir Ahmad et al., 2022b). On the other hand, low ash content is important because it reduces the likelihood of operational issues in fluidized bed reactors, such as agglomeration or de-fluidization due to clogging of the air distributor plate (Fryda et al., 2008).

1.3 Problem Statement

Macadamia nutshells are byproducts of agro-processing industries and have the potential to be utilized as alternative fuels. However, these wastes are often discarded or burned through direct and uncontrolled combustion, causing air pollution and making their use unsustainable.

Although biomass wastes are considered a renewable energy source, their conversion to clean energy using gasifiers remains challenging. One major issue is the limited information available for optimizing gasifier process parameters to produce syngas with high energy density and low tar content, which limits their industrial application. Designing gasifiers to operate optimally can enhance syngas quality, but this is usually based on experiments using lab-scale units, which are expensive and time-consuming. Moreover, gasifiers operate at extremely high temperatures, making optimization experiments technically challenging.

While fluidized bed gasifiers are preferred for their superior heat and mass transfer capabilities, the fluidization process presents a complex multiphase problem. This complexity makes experimental measurements of fluidized bed hydrodynamic parameters challenging, especially at high temperatures. As a result, there is a significant gap in the understanding of flusized bed systems for practical use with biomass such as macadamia nutshells.

The aim of this study was to investigate fluidized bed hydrodynamics and gasification process using numerical modeling techniques. By employing numerical simulations, the study seeks to overcome the challenges associated with conducting experimental measurements at elevated temperatures.

1.4 Study Objectives

The main objective of this study was to design, investigate and optimize the performance of a fluidized bed gasifier for syngas production using numerical method. To achieve this objective, the following specific objectives were pursued:

i. To design a laboratory-scale fluidized bed unit.
ii. To develop and validate a numerical model for the hydrodynamics of the fluidized bed.
iii. To develop and validate a numerical model for the gasification of biomass waste.
iv. To analyze the influence of process parameters on the gasifier performance using the validated numerical gasification model.
v. To optimize the operational parameters of the fluidized bed gasifier.

1.5 Justification

Biomass waste gasification is crucial due to its potential to address both the increasing global energy demand and the pressing environmental challenges. International Energy Agency (IEA) estimates that the global energy demand is expected to increase by more than 25 % by 2040 (IEA, 2019). Biomass waste gasification offers an attractive solution by providing a renewable energy source that meets societal energy needs while reducing fossil fuels reliance. Consequently, biomass gasification can play an important role in reducing carbon emissions and mitigating climate change (A. Kumar et al., 2009).

Gasification also addresses the challenge of biomass waste management. Biomass waste undergoes natural decomposition when left unattended, releasing hamful pollutants such as methane and carbon dioxide through anaerobic process (Kabeyi and Olanrewaju, 2022). Converting biomass waste into useful energy prevents the accumulation of waste in landfills and reduces the release of harmful emissions (Demirbas, 2004).

In this study, a fluidized bed gasifier is used due to its superior mass and heat transfer capabilities, leading to higher efficiency and lower tar content in syngas. Numerical models for fluidized bed hydrodynamics and gasification processes will be developed. The models will be beneficial because it addresses challenges associated with conducting experimental measurements at high temperatures. Additionally, optimizing the gasification process parameters will improve syngas energy density and further reduce tar content, facilitating the adoption of gasification technology on an industrial scale.

Adoption of gasification technology for biomass waste will also contribute to economic growth and job creation. Many regions in rural areas possess significant biomass resources that are underutilized. Investing in biomass waste gasification technologies can harness local resources to generate clean energy, simulate economic growth and create jobs.

1.6 Thesis Structure

This thesis is organized into five chapters. **Chapter one** provides the research background, emphasizing the need for searching alternative energy sources, with a particular focus on biomass. It also outlines the problem statement, justifies the research significance, and states the study objectives. In **chapter two**, a comprehensive literature review is presented, covering both fluidized bed hydrodynamics and the gasification process. The chapter also delves into the analysis of the findings of other researchers to identify gaps for further research. **Chapter three** focuses on the materials and methods. The methods used to characterize the biomass materials and silica sand are discussed first, followed by the design and fabrication of the experimental setup. The chapter concludes with a the numerical methods employed for the fluidized bed hydrodynamics and gasification process studies. In **chapter four**, the results and discussions for the fluidized bed hydrodynamic and gasification are presented. The results include the experimental measurements, model validation, numerical modeling and the multi-objective optimization results. In **chapter five**, conclusions drawn from the research findings are presented, and recommendations that provide opportunities for future work are suggested. Supplementary information is presented in the appendices.

CHAPTER TWO

LITERATURE REVIEW

This section will present a literature review of the biomass waste gasification technologies, fluidized bed hydrodynamics and biomass gasification process.

2.1 Waste to Energy Conversion Technologies

Biomass waste can be converted into energy through thermo-chemical and bio-chemical conversion processes. Bio-chemical conversion involves processes like anaerobic digestion and fermentation, which utilize biological decomposition to generate gaseous or liquid fuels. Anaerobic digestion involves the decomposition of organic matter in the absence of oxygen, resulting in the production of biogas, which is primarily composed of methane and carbon dioxide. Fermentation, on the other hand, is a process that converts biomass into bioethanol, a liquid fuel that can be used as an alternative to gasoline (Janajreh and Al Shrah, 2013).

Thermo-chemical conversion, which relies on the application of heat to transform biomass feedstock into different forms of energy, is advantageous over bio-chemical processes. Biochemical methods often encounter challenges when treating biomass waste rich in lignocellulose materials. They also tend to operate at a slower pace and in batch mode, resulting in a dilute product stream. In contrast, thermo-chemical conversion methods can be conducted with or without the presence of oxygen. The three most common thermo-chemical conversion techniques are combustion, pyrolysis and gasification (D. Glushkov et al., 2021).

Combustion involves the burning of biomass waste to produce heat, which can be used directly or converted into other forms of energy. Gasification, on the other hand, is a process that converts biomass into syngas, composed mainly of carbon monoxide and hydrogen. Syngas can be further utilized for power generation, as a fuel in industrial processes, or refined into liquid fuels (D. O. Glushkov et al., 2021).

Pyrolysis entails the thermal decomposition of biomass waste in an oxygen-deprived environment. The main outputs of pyrolysis include bio-oil, non-condensable gases, and char. Bio-oil is utilized in various applications such as diesel engines, decentralized power generation units, as well as in large-scale power plants. However, widespread industrial adoption of bio-oils is hindered by challenges related to fuel quality, high viscosity, limited stability and corrosiveness (D. O. Glushkov et al., 2021). Approximately 10 to 35 % of char is produced through pyrolysis, which can be utilized as solid fuel in boilers or in the production of activated carbon (Nkosi et al., 2021). The gas generated during pyrolysis can be processed into syngas to use in engines and turbines (D. Glushkov et al., 2021).

2.1.1 Gasification

Gasification technology produces syngas from biomass waste. The composition of syngas determines its potential applications, with various possibilities based on its characteristics. Syngas can undergo direct combustion in boilers or used in gas turbines and IC engines (F. Njuguna et al., 2023). It is mainly composed of CO and H_2, with traces of other gases like CH_4, N_2, CO_2 and tar as the main impurity. Syngas composition is however dependent on biomass type, gasifier's operating conditions, and the gasification agent, making it difficult to predict it precisely (F. Njuguna et al., 2023).The gasification process consists of four stages: drying, devolatilization (pyrolysis), combustion, and reduction (gasification), as illustrated in Figure 2.1 (U. Kumar and Paul, 2019).

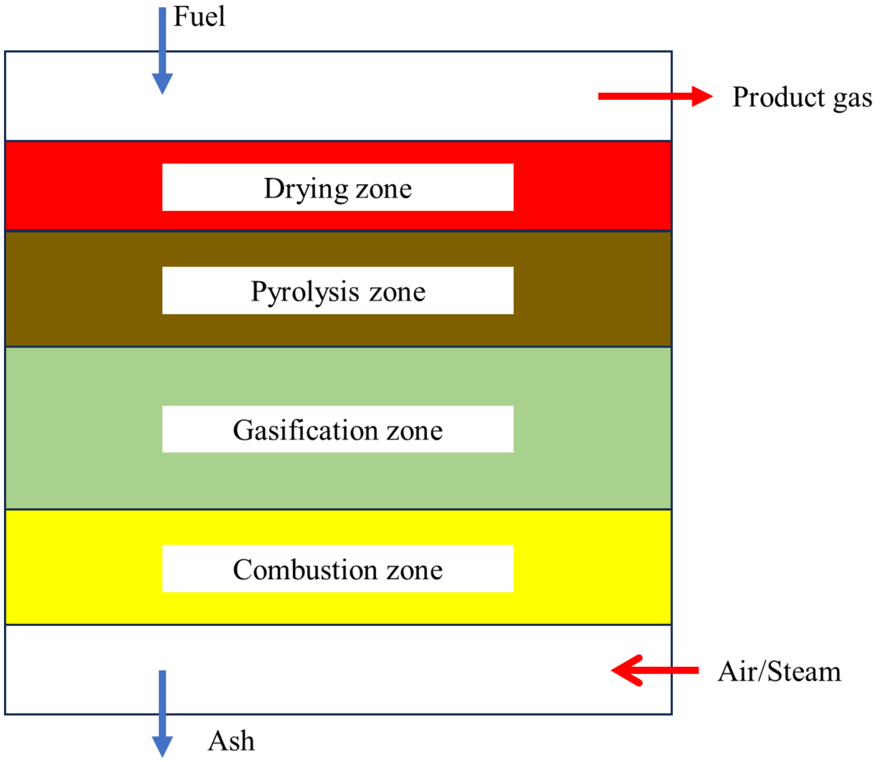

Figure 2.1: Gasification Stages

Source: (Lindgren, 2016)

Moisture contentis critical in biomass fuel gasification as it converts into steam during the drying stage. A moisture content of 15 % or lower is advised for most biomass feedstock. In the initial stage, drying converts moisture into steam, which plays an important role in subsequent gasification reactions (D. Glushkov et al., 2021; Safarian et al., 2022). The drying process often occurs simultaneously with devolatilization or pyrolysis (U. Kumar and Paul, 2019).

Devolatilization occurs between 350 °C and 800 °C in the absence of oxygen, decomposing biomass waste into gases such as methane, hydrogen, carbon monoxide, carbon dioxide, and hydrocarbons, along with biochar (Safarian et al., 2022). The composition of gases and biochar depends on biomass chemical composition and the process temperature. Pyrolysis temperature determines the extent of pyrolysis reactions and the resulting products (Nkosi et al., 2021). Heat is conducted from the surface to the center of biomass particles during the pyrolysis stage, inducing thermal decomposition and releasing volatiles, which ensures uniform exposure to the required temperatures for complete pyrolysis (D. Glushkov et al., 2021).

Oxidation, also known as combustion, is the exothermic stage of gasification and supplies thermal energy for endothermic reactions. It raises gasifier temperatures between 800 °C and 1100 °C (Zhao et al., 2015). To initiate the combustion process, a controlled amount of oxygen, below stoichiometric levels, is supplied to the gasifier, ensuring partial biomass oxidation. During this stage, char and hydrogen reacts to form carbon dioxide and water vapor, releasing heat energy. This heat is crucial for sustaining endothermic gasification reactions to sustain the endothermic reduction reactions (Ren et al., 2022).

During the reduction stage, the products of pyrolysis and oxidation react with the gasifying agent to produce syngas and tars. Reduction reactions are endothermic and heat from the oxidation stage is absorbed to facilitae this process. Caution is needed to prevent ash from contaminating the reduced char, which can lead to overheating (Puig-Gamero et al., 2021).

2.2 Gasification Mechanisms

The oxidation and the reduction steps, whicht occur after pyrolysis involves both heterogeneous (gas-solid) and homogeneous reactions (gas-gas). Production of syngas results from a series of endothermic and exothermic chemical reactions taking place between carbon in the char, carbon dioxide, steam, and hydrogen inside the reactor. These reactions are are described in the following section.

2.2.1 Water-gas Shift Reaction

Water-gas shift reaction, shown in Equation (2.1), is a homogeneous reaction between carbon monoxide and steam. This reaction is exothermic reversible reaction and is used to reduce carbon monoxide and increase hydrogen concentration in syngas (Al-Farraji, 2017).

$$CO + H_2O \rightleftharpoons CO_2 + H_2 \qquad 2.1$$

2.2.2 Boudouard Reaction

Boundouard reaction, shown in Equation (2.2), is an endothermic reaction and requires temperature for effectiveness. At temperatures above 700 ^{o}C, the free energy change becomes negative, breaking carbon dioxide bonds and favoring the formation of caron monoxide (Al-Farraji, 2017).

$$C + CO_2 \longrightarrow 2CO \qquad 2.2$$

2.2.3 Methanation Reaction

Methanation reaction, shown in Equation (2.3) is an exothermic reaction and occurs between carbon and hydrogen to produce methane. Methane increases the overall heating value of syngas due to its high energy density. Low temperature and high pressure are required to promote methanation reaction (Ayub et al., 2020).

$$C + H_2 \longrightarrow CH_4 \qquad 2.3$$

2.2.4 Char Combustion Reaction

Char reduction reactions, shown in Equations (2.4) and (2.5), are heterogeneous exothermic reactions which generates heat to support the endothermic reactions. The formation of carbon monoxide and carbon dioxide during char combustion depends on the size of biomass particle. For small particle sizes, the carbon monoxide formed during combustion diffuses out quickly, while it burns within the boundary layer of the particle for bigger particles, transporting carbon dioxide out as a result of slow diffusion (Sait et al., 2012; Zhao et al., 2015).

$$C + 0.5O_2 \longrightarrow CO \qquad 2.4$$

$$CO + O_2 \longrightarrow CO_2 \qquad 2.5$$

2.3 Sustainable Use of Macadamia Nutshells

Efforts have been made to add value and harness the potential of macadamia nutshells sustainably by employing various technologies. Macadamia nutshells find application as feedstock for the production of activated carbon, bio-diesel, and fertilizer (Azad et al., 2017; Machedi et al., 2019). Regarding energy production, macadamia nutshells have been utilized for pyrolysis, bio-chemical conversion, solid fuel densification, and hydrothermal processes (Samaksaman et al., 2023). Xavier et al. (2016) conducted a study on the utilization of macadamia nutshells for bio-diesel production, employing a kinetic model. However, a primary challenge associated with pyrolysis is the high moisture content, which requires significant heat for vaporization, consequently impacting overall efficiency (Cai and Liu, 2007).

Bio-chemical conversion of macadamia nut shells has been studied experimentally for the production of biogas (Vu et al., 2023). This process involves fermentation and anaerobic digestion which requires more time compared to thermal-chemical processes (Kabeyi and Olanrewaju, 2022; Nazari et al., 2017). On the other hand, hydrothermal conversion involves transforming biomass into hydrochar through dehydration and decarboxylation (Libra et al., 2011). Water serves as the primary reactant for hydrothermal conversion and requires a significant amount of energy during the conversion process (Samaksaman et al., 2023).

Gasification, a thermal-chemical conversion process that occurs under high-temperature conditions, holds significant promise as a technology for extracting syngas from biomass waste. Syngas is a versatile fuel and finds applications in internal combustion engines, turbines and the production of liquid fuels (Linh et al., 2021). Despite the diverse application of gasification with various feedstocks, there is a scarcity of studies addressing the gasification of macadamia nutshells. Given their excellent physio-chemical proretties, gasification can be extended to macadamia nutshells for syngas production.

2.4 Gasifiers

Gasifiers can be categorized into two main types: fixed bed and fluidized bed gasifiers. Each type offers distinct advantages and disadvantages depending on the intended application, the type of biomass feedstock, and the specific operating conditions. The fixed and fluidized bed gasifiers are discussed below.

2.4.1 Fixed Bed Gasifiers

Fixed bed gasifiers (FBG) are operated below the melting temperatures of the bed materials to prevent the formation of slag. They consist of a vertical cylindrical space to accommodate the fuel and gasifying media. Additional components include a fuel-feeding unit, an ash-removal unit, and a provision for the exit of gas. In a fixed bed gasifier, the biomass fuel is gradually consumed, causing the bed to move slowly downward within the reactor. Additionally, fixed bed gasifiers exhibit distinct layers where drying, pyrolysis, reduction, and oxidation occur. In fixed bed configurations, the bed particles remain stationary, and the gasifiers are operated below the minimum fluidization velocity required to achieve fluidization of the bed materials. Fixed bed gasifiers are commonly found in two main configurations: downdraft and updraft configurations (Din and Zainal, 2016; Samiran et al., 2016). Figure 2.2 shows the two fixed bed gasifiers configurations.

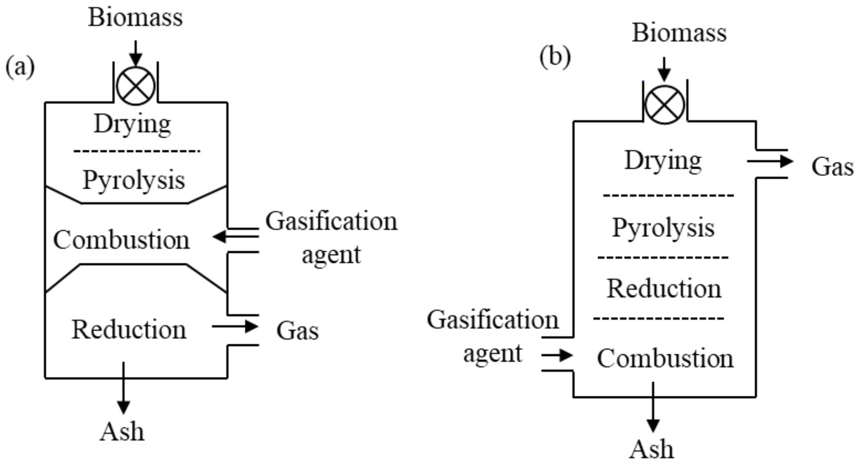

Figure 2.2: Fixed bed Gasifiers (a) Downdraft (b) Updraft

Source: (Samiran et al., 2016)

In an updraft gasifier configuration, the biomass feedstock is introduced from the top, while the air supplied from the bottom. Consequently, the oxidation reactions primarily occur at the bottom of the bed. As a result of combustion, the bottom section of the gasifier experiences the highest temperatures, while the syngas exits from the top at temperatures around 500 °C. However, due to the relatively low temperature at the exit, syngas produced in updraft gasifiers tends to contain a significant amount of tar (Bonilla et al., 2019).

On the other hand, in a downdraft gasifier, both the biomass waste and the gasifying agent enter from the top, while the syngas is discharged from the bottom of the gasifier. In the downdraft configuration, the temperature at the top of the gasifier is typically elevated necessitating the installation of a heat recovery system to capture and utilize the heat from the syngas before it is stored or utilized (Samiran et al., 2016).

2.4.2 Fluidized Bed Gasifiers (FBG)

Fluidized bed gasifiers (FBG) utilize inert bed materials, such as sand or alumina, to transfer heat to the fuel particles. The inert bed materials are fluidized using air or oxygen. Similar to fixed bed gasifiers, fluidized bed gasifiers also operate below the melting temperatures the bed materials. However, they offer distinct advantages due to their unique characteristics (Samiran et al., 2016).

Fluidized bed gasifiers exhibit higher heat transfer rates and improved mixing capabilities compared to fixed bed gasifiers. The movement and mixing of the bed materials in a fluidized bed enhance heat exchange between hot gases and solid particles, resulting in more uniform temperature distribution and higher reaction rates. Additionally, FBG facilitate higher mass flow rates, offer greater flexibility in biomass feeding, and typically generate moderate levels of tar and particulates compared to fixed bed gasifiers (Samiran et al., 2016; Sansaniwal et al., 2017). Unlike fixed bed gasifiers, fluidized bed gasifiers do not have distinct drying, pyrolysis, reduction, and oxidation stages because the gasification process occurs simultaneously throughout the bed (Motta et al., 2018).

For feedstock selection, fluidized bed gasifiers can utilize biomass sources with variable moisture contents and particle sizes below 6 mm (Molino et al., 2016). However, it is important to select biomass with low ash and alkali metal contents, as these materials can form agglomerates in the presence of silica from the bed or fuel ash. Consequently, biomass materials such as grasses, canes, almond hulls, and rice and wheat straws are not recommended for this reactor configuration (Din and Zainal, 2016; Motta et al., 2018).

Fluidized bed gasifiers can be further categorized into two types: bubbling and circulating fluidized beds. Bubbling fluidized bed (BFB), shown in Figure 2.3 (a), involves the upward movement of gas and particles, creating bubbles within the bed. They operate by introducing fluidizing air at velocities above the minimum fluidization velocity, typically below 5 m/s (Samiran et al., 2016). This creates an emulsion of particles and gas bubbles, maintaining the bed in a fluidized state. A freeboard section with an increased cross-sectional area helps reduce the superficial velocity of gases, causing bed materials to return and ensuring consistent solid content within the bed (F. Njuguna et al., 2023).

Bubbling fluidized bed gasifiers are known for producing tar and solid particles, which necessitate gas cleaning systems. Tar formation presents challenges in fluidized bed gasifiers but can be reduced through proper gasifier design and secondary techniques such as catalytic cracking(Cortazar et al., 2023).

Bubbling fluidized bed (BFB) gasifiers can be scaled up to large sizes, where even distribution of raw materials is essential. These gasifiers offer excellent flexibility in fuel loading and processing, handling a wide range of fuels with high ash content, including biomass, lignite, and coals, provided biomass particle sizes are below 6 mm (Molino et al., 2016; Samiran et al., 2016). It is important to either use fuels with high ash melting temperatures or operate below the ash melting temperature of the fuels to prevent bed particle agglomeration and de-fluidization in BFB gasifiers (Fryda et al., 2008).

Circulating fluidized beds (CFB), shown in Figure 2.3 (b), operate in a similar manner to BFB gasifiers, but with significantly higher fluid flow velocities. This increased velocity facilitates better mixing of the fluid with the bed material, ensuring efficient gas-solid contact. As a result, CFB gasifiers exhibit enhanced heat and mass transfer rates due to the high velocity of the gas and solid particles. However, the higher air flow rates and the recirculation of solids in the CFB system leads to increased power requirements and investment costs compared to conventional fluidized bed reactors.

These factors make CFB gasifiers more expensive to operate and construct (Samiran et al., 2016).

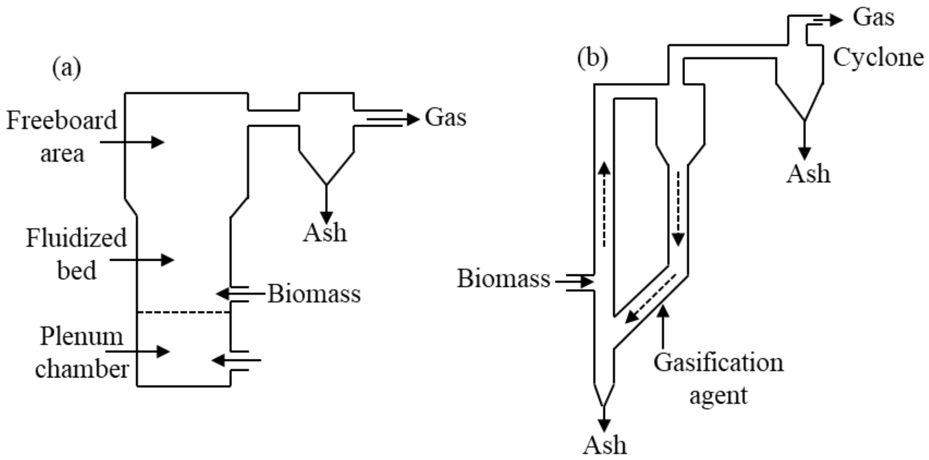

Figure 2.3: Fluidized Bed Gasifiers (a) Bubbling (b) Circulating

Source: (Samiran et al., 2016)

2.5 Fluidization

When a gas flows through a bed of granules at low velocities, it permeates the voids between the particles. Initially, the granular material remains in a stationary state. However, as the velocity of the gas increases, a critical point is reached where the drag force exerted on the particles equals their weight. This results in a transition to a fluid-like state, known as fluidization (Subramani et al., 2007).

During fluidization, the bed of granular material becomes mobile and behaves like a fluid. The gas flows through the voids between the particles, causing them to move and mix. The velocity at the incipient of fluidization is called the minimum fluidization velocity (U_{mf}) (Reyes-Urrutia et al., 2022). Depending on the velocity of the fluidizing agent, different fluidization regimes can be observed, including bubbling, slugging, turbulent, and fast fluidization.

Pressure in fluidization provides the necessary force to suspend solid particles. The pressure drop profile, influenced by gas velocity, indicates the transition between fixed bed and fluidized bed regimes. In the fixed bed regime, pressure drop increases linearly with gas velocity until fluidization occurs, after which it remains constant with air velocity. The constant pressure drop, calculated using Equation (2.6), depends on the amount of bed materials. The intersection of the linear increase and horizontal line represents the minimum fluidization point (Subramani et al., 2007). The pressure drop is determined by the drag forces exerted by the fluid on the particles, calculated using Equation (2.7) (Alghamdi et al., 2021).

$$\left(\frac{\Delta P}{L}\right)_{mf} = (1-\varepsilon)\left(\rho_s - \rho_g\right)g \tag{2.6}$$

$$F_d = (C_d \times \rho_g \times A \times U^2)\,/\,2 + \frac{(\varepsilon \times dp \times \rho g \times U^2)}{(150 \times (1-\varepsilon)^2)} \tag{2.7}$$

where Δp is the pressure drop, L is the initial bed height, F_d is the drag force, C_d is the drag coefficient, ρ_g is the air density, A is the cross-sectional area of the bed, U is the superficial air velocity, ε is the void fraction, and d_p is the particle diameter.

Before reaching the minimum fluidization point (Umf), the bed height remains static. Once the air velocity exceeds Umf, the bed starts to move, and increasing the flow rate further leads to a gradual and uniform expansion of the bed (Subramani et al., 2007). Effect of superficial velocity on the bed pressure drop and movement is shown in Figure 2.4.

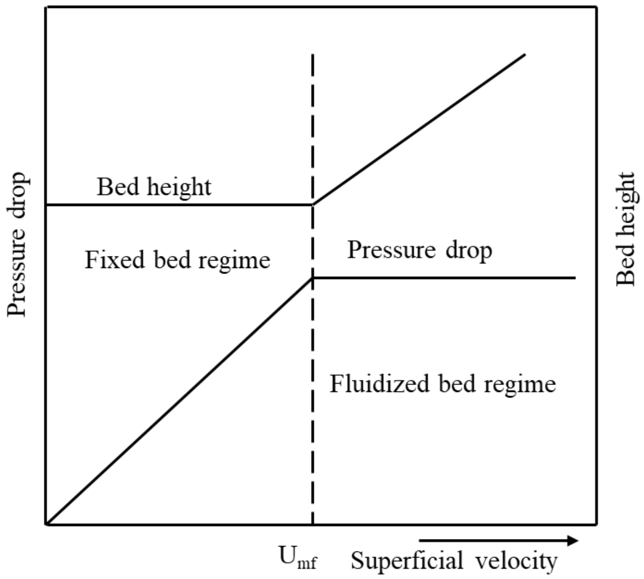

Figure 2.4: Determination of the Minimum Fluidization Point

Fluidization behavior of gas-solid systems is mainly affected by solid particle characteristics of the bed materials. Solid particles are classified into four categories according to Geldart classification of powders as shown in Table 2.1.

Table 2.1: Geldart Powder Classification

Geldart Group	Particle size range (μm)
A	30 – 150
B	150 – 750
C	0 – 30
D	>750

Source: (Wang, 2009; Welahettige et al., 2017)

Group A consists of cohesive or fine powders that tend to form lumps or agglomerates when fluidized and exhibit significant bed expansion at low air velocities without bubble formation. Group B includes non-cohesive, free-flowing powders that fluidize easily and exhibit good fluidization characteristics, with bubbles forming at the onset of fluidization. They include sand particles and are used in fluidized bed combustors and gasifier units with few difficulties. Group C particles exhibit poor fluidization characteristics and often tend to form slugs or channeling in fluidized beds. They tend to behave more as particle cluster than single particles (Shaul et al., 2014; J. Wang, 2009). Lastly, group D comprises coarse particles which are difficult to fluidize and generally require specialized fluidization techniques or equipment. They form huge and slugging bubbles during fluidization and are applied in spouting beds which have low gas requirements than the standard fluidized beds (Welahettige et al., 2017). Figure 2.5 shows particle size classification and the associated forces.

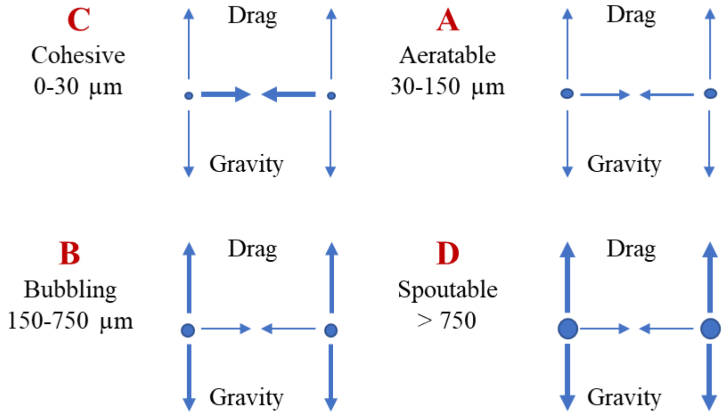

Figure 2.5: Geldart Classification of Powder

Source: (Welahettige et al., 2017).

2.6 Numerical Modeling of Multi-Phase Flows

Designing a fluidized bed gasifier requires understanding of both the hydrodynamics of the fluidized bed and the gasification process. Fluidization involves the interaction between gas and solid particles, resulting in a multiphase flow system (Dos Santos et al., 2020). This includes aspects such as the fluid flow patterns, particle movement, mixing, bubble behavior and heat transfer. On the other hand, the gasification process involves reactive chemical reactions such pyrolysis, oxidation, and reduction, which converts solid biomass into gaseous components (Ostermeier et al., 2019).

In recent years, the study of fluidized beds involved extensive and expensive experimental techniques. Researchers use both intrusive and non-intrusive methods to investigate the fluidized bed hydrodynamics. Non-intrusive experimental methods are generally preferred because they allow for the examination of the entire flow domain without disturbance (Sun and Yan, 2016). These methods include X-ray radiography, electrical capacitance tomography, particle image velocimetry, phase doppler anemometry, and magnetic resonance imaging, which are used to study bed porosity, bubble formation, and size (Li et al., 2018; Mathiesen et al., 2000; Shah et al., 2017; Sun and Yan, 2016). On the other hand, intrusive methods include pressure transducers, hot wires, optical probes, and endoscopes, and are used to study pressure drop, bed porosity, and temperature distribution (Ghaly et al., 2015; Lv et al., 2016).

Quantifying the intricate dynamics of fluidized bed hydrodynamics poses challenges due to the scarcity of experimental data and difficulties associated with high-temperature experiments. To overcome these limitations, numerical modeling has become a valuable tool, enabling non-intrusive multiphase simulations. This minimizes the need for extensive experimentation, reducing both time and cost (S. Wang et al., 2023). Validated numerical models offer approximations for understanding and predicting fluidized bed phenomena.

Simulation of fluidized bed gasifier uses two approaches for the gas-solid flow modeling. i.e., Eulerian-Eulerian and Eulerian-Lagrangian approaches. The Eulerian-Eulerian is a two-fluid model (TFM) that treats both gas and solid phases as inter-penetrating continua. Conservation equations of mass, momentum and energy are solved for each phase and the relation for solid phase is usually closed with kinetic theory of granular flow (KTGF). This approach has three sub-models namely volume of fraction (VOF), mixture and Eulerian models. The Eulerian model is generally preferred for fluidized bed simulations because the Volume of Fluid (VOF) model is primarily used for fluid-fluid applications, while the mixture models have limited accuracy (Greenshields, 2015).

Eulerian-Lagrangian approach is based on discrete element method (DEM) and supports the molecular dynamics. In this approach, the gas phase is treated as the continuous phase while the solid phase is treated as the dispersed phase where the particles are tracked individually. The governing equations of the momentum, energy and mass are exchanged between fluid and the dispersed phases. Eulerian-Lagrangian approach is suitable for problems having low dispersed phase volume fraction, in which case the particle-particle interactions can be ignored. This approach is, therefore, not suitable for the modeling of dense bubbling fluidized beds (U. Kumar and Agarwal, 2017).

2.7 Numerical Modeling of Gas-Solid Fluidized Beds

Fluidized beds are utilized in industries for processes such as gasification, drying, catalytic reactions and chemical looping. They are advantageous due to their enhanced mixing and uniform heat transfer capabilities. For syngas production from biomass waste, bed materials like silica sand are employed due to their ability to ensure uniform temperature distribution and improved heat transfer rates (Al-Farraji and Taofeeq, 2020).

Understanding the hydrodynamics of fluidized beds is crucial due to its direct impact on the design, optimization, and operation of fluidized beds systems, which rely on the fluidized bed hydrodynamic parameters (F. Njuguna et al., 2023). Designing a gas distributor plate for gasifiers requires that its pressure drop (ΔPDP) needs are met at the point of minimum fluidization (mf) to ensure uniform fluidization. Generally, it is accepted that the ratio of ΔPDP to bed pressure drop (ΔPB) should fall between 0.1-0.4 (Ghaly et al., 2015). When U_{mf} is overestimated, the fluidized bed (FB) unit operates with a higher pressure drop than necessary. This is inefficient because the pressure drop is supplied by a blower or an air compressor, which pumps the fluidizing gas into the FB system. Consequently, excess pressure drop leads to wastage of resources. On the other hand, if U_{mf} is underestimated, it can cause issues such as maldistribution of the fluidizing gas, the formation of hot spots, and the presence of dead zones (Al-Farraji and Taofeeq, 2020).

Minimum fluidization velocity (U_{mf}) influences elutriation which impacts on the gasifier performance and can potentially lead to inefficiencies of the gasifier performance if not properly controlled (Y. M. Chang et al., 2005). Additionally, the bed porosity plays a crucial role in heat transfer rates. If the porosity is too low, heat transfer rates can be insufficient, resulting in slower reaction rates and influencing the syngas concentration and yield. Conversely, a higher bed porosity can enhance heat transfer rates, promoting faster reaction rates and increasing syngas yield (Mandal et al., 2013).

Fluidized bed units are typically operated at high temperatures, yet the prediction and estimation of their hydrodynamic parameters often rely on models developed under ambient temperature conditions (Al-Farraji and Taofeeq, 2020). Operating a fluidized bed unit at extremely high temperatures introduces various thermal effects, such as changes in fluid properties, heat transfer characteristics, and particle behavior, which alters the hydrodynamics of the system. However, existing models and correlations for predicting hydrodynamic parameters are primarily developed and validated based on experimental data obtained at ambient temperature conditions (Mahinpey et al., 2007; Rasteh et al., 2018). As a result, using these models to predict hydrodynamic parameters in high-temperature fluidized bed units can introduce uncertainties and inaccuracies.

Limited research has been conducted on the hydrodynamics of the fluidized bed at high temperatures, due to the difficulties of conducting experiments with high-temperature laboratory-scale units. Consequently, the characteristics of fluidized beds under these conditions remains not fully understood (Fang et al., 2020). Existing experimental studies primarily concentrated on the minimum fluidization velocity (U_{mf}) and have reported an increase in U_{mf} with temperature. Al-Farraji et al. studied the impact of elevated temperature on the fluidized bed hydrodynamics and reported that the minimum fluidization velocity decreased as the temperature of the bed materials increased, while it increased with the size od the sand particles (Al-Farraji and Taofeeq, 2020). To gain a comprehensive understanding, further studies are essential to explore other crucial aspects of fluidized bed hydrodynamics, like bed expansion, bubble formation, and porosity. Additional research in these areas would contribute to a better understanding of fluidized beds at elevated temperatures.

Other studies conducted to estimate the minimum fluidization velocity in fluidized bed systems have further suggested empirical correlations for U_{mf} (Al-Farraji and Taofeeq, 2020; Shrestha et al., 2019). However, it has been reported that these correlations often yield different results compared to experimental findings under elevated temperature conditions. Gosavi et al. (2018) studied the minimum fluidization velocity at elevated temperatures and compared their results with the correlations proposed in the literature. They found that the results obtained from the correlations differed from those obtained in their study. Shao et al. (2019) noted that the correlations were derived from experiments conducted at certain conditions, and may not be applicable at different conditions, leading to unreliable outcomes. Therefore, further research is needed to improve the accuracy to predict the minimum fluidization velocity in high-temperature fluidized bed applications.

The hydrodynamic behavior of fluidized beds is influenced by the characteristics of bubbles, including their size and growth, which, in turn, have a significant impact on heat and mass transfer within the system. The behavior and dynamics of bubbles play a crucial role in determining the distribution of gas and solids, affecting the overall flow patterns, mixing, and residence time of particles. Furthermore, the size and growth of bubbles influence the interfacial area available for heat and mass transfer, thereby influencing the efficiency and effectiveness of these transfer processes in fluidized bed systems (Shrestha et al., 2019).

There is limited research available on the quantification of bubble size in fluidized beds, particularly at elevated temperatures. Although there are attempts to study bubble behavior under these conditions, the findings from different studies have been inconsistent. For example, Issaou et al. (2019) observed from experimental measurements that bubble size reduced with rise in temperature. However, other researchers who focused on visualizing bubbles in experiments reported an opposite trend, with bubble size increasing as the temperature rose (Nemati et al., 2016). These contrasting results highlight the complexity of understanding the fluidized bed hydrodynamics at high temperatures, particularly concerning bubble size and growth, and emphasize the necessity for further research.

Computational fluid dynamics has been utilized to investigate the fluidized beds, with the majority of these studies conducted at ambient temperature conditions. For instance, Uddin et al. (2017) employed Ansys Fluent to investigate fluidized beds hydrodynamics at ambient temperature and reported accurate prediction of pressure drop. Although CFD work is reported in literature, it is however noted that the numerical models developed for ambient temperature conditions lack applicability in predicting fluidized bed hydrodynamics at high temperatures, emphasizing the need for further studies in this area.

The few fluidized bed numerical studies reported in literature which involved high temperature were conducted using 2D models, and mostly investigated heat transfer and thermal conductivity (J. Chang et al., 2012; Xie et al., 2008). In their study, Chang et al. (2012) employed CFD to model particle-particle heat transfer in a fluidized bed, using 2D modeling. The findings of the study revealed that the particle-particle heat exchange coefficient between different particle classes increases with larger particle sizes and higher superficial gas velocities. The effect of modeling using 2D was studied by Xie et al. (2008) who reported that 2D models are not sufficient to reproduce 3D results. Cammarata et al. (2003) further validated the hydrodynamic results of bubbling fluidized bed using 2D models and reported overprediction of bed movement. These findings emphasize the necessity for additional research using 3D models to enhance the development of numerical models that can predict fluidized bed hydrodynamic behavior more accurately.

Effects of parameters such as timestep, specularity and restitution coefficient on fluidized bed hydrodynamics have been studied. The effect of timestep and frictional stress on bed porosity was investigated by Hulme et al. (2005) and who reported that small timesteps improved solution but increased the computational cost significantly. They also reported that the frictional stress should be considered in order to obtain realistic results and to have a better solution divergence. It is also reported that a small time step should be considered to ensure a courant number of less than 0.1, and avoid numerical instabilities and divergence (Alobaid et al., 2021).

Particle-wall interaction is quantified in terms of specularity coefficient (Φ) which has a significant effect on fluidized bed hydrodynamics especially when modeling small scale units. Some researchers used non-slip boundary condition (J. Wang, 2010) while others used slip wall boundary condition (Armstrong et al., 2010). The effect of specularity and restitution coefficient on fluidized bed behavior was investigated by Chanchal et al. (2013). They reported that the specularity coefficient had no significant impact on the bed movement but the parameters such as granular temperature and the void fraction was affected especially near the walls. They recommended using small specularity coefficient to capture fluidization phenomenon accurately. However, they reported that the restitution coefficient was not important for the flow characteristics. Similarly, Ehsani et al. (2015), studied the effect of both specularity and restitution coefficients and reported that a specularity coefficient values less than 0.5 should be used because small values captured the fluidized bed hydrodynamics more accurately.

In a multiphase flow system, the interstitial fluid exerts drag forces on the solid particles because of the velocity differences between the gas and the solid phases. The drag function is, therefore, an important consideration in a gas-solid fluidized bed modeling. In the fluidized bed numerical modeling, different drag model correlations are used and are widely investigated in the literature due to their high relevance (Zimmermann and Taghipour, 2005). One of the mostly used drag models are the EMMS, Gidaspow and Syamlal O’brien drag models. Zimmermann et al. indicated that the original forms of Syamlal Obrien models are not sufficient for modeling fluidization behavior of small particles (Zimmermann and Taghipour, 2005). Furthermore, the use of Syamlal Obrien requires experimental minimum fluidization velocity as an input parameters during numerical simulations (Zimmermann and Taghipour, 2005). A comparative study of EMMS, Gidaspow and Syamlal O’brien drag models was conducted by Loha et al. (2012) who investigated their effect on the hydrodynamics of bubbling fluidized beds. The Gidaspow and Syamlal O’brein drag models were able to predict the hydrodynamics at the core annulus of the bed while the EMMS model predicted the time-averaged granular temperature with good accuracy. Overall, the hydrodynamic results from Gidaspow drag model were reported to compare well with the experimental results.

This review reveals that fluidized bed behavior at higher temperatures differs significantly from that at ambient conditions, highlighting the need for further investigation into the hydrodynamics of high-temperature fluidized beds. To improve the accuracy of predicting hydrodynamic parameters in such units, it is crucial to develop and validate models that account for temperature-dependent effects and thermal influences on flow. This approach will enable more reliable predictions, ensuring better design, optimization, and operation of fluidized bed units at elevated temperatures.

2.8 Numerical Modeling of Biomass Gasification

The operation of gasifiers involves working with extremely high temperatures, which introduces challenges when operating laboratory-scale units and collecting accurate data at elevated temperatures (Armstrong et al., 2010). Furthermore, biomass gasification entails complex chemical reactions and physical processes, including drying, pyrolysis, char decomposition, oxidation, and reduction, which add complexity to the gasification process. These processes interact with each other and can have a significant impact on the overall gasification efficiency and the composition of the resulting gas. Gasification experiments, therefore, require extensive resources, making them expensive and time intensive (Eikeland et al., 2015).

Employing a validated numerical model can reduce the challenges associated with experimental investigations in gasification, offering valuable insights into the complex gasification process and providing a cost-effective and efficient tool for understanding, designing, and optimizing gasification processes (Puig-Gamero et al., 2018).

To investigate the gasification process, researchers have developed simulation models that employ various approaches. Some simulations utilize computational fluid dynamics (CFD) techniques (U. Kumar and Paul, 2019; Ostermeier et al., 2019; Yu et al., 2018) while others rely on process simulation software such Aspen Plus (Islam, 2020; Marcantonio et al., 2020; Vaezi et al., 2011). CFD models consider the internal flow characteristics within the gasifier, incorporating complex fluid dynamics phenomena. However, CFD simulations are computationally intensive, necessitating comprehensive computational model design, its discretization and time-step selection. Additionally, CFD simulations often exhibit instability and demand significant computational resources (Puig-Gamero et al., 2021; Y. Wu et al., 2014).

Aspen Plus is widely used for process simulation and optimization in various industries, including gasification. It offers a user-friendly interface and a vast library of pre-built models and thermodynamic databases that can be tailored to simulate gasification reactions, fluid dynamics, and heat and mass transfer phenomena. Aspen Plus allows researchers to simulate complex gasification processes by considering the interactions between multiple components, reactions, and operating conditions (Ahmed et al., 2015). Additionally, Aspen Plus simplifies the simulation workflow, enhances efficiency, and provides valuable insights on the gasification process, aiding in the design and optimization of gasification systems (Vaquerizo and Cocero, 2018).

Aspen Plus offers both the thermodynamic equilibrium (TEM) and kinetic modeling (KM) approaches. TEM, a 0-D (dimensionless) model, does not consider the specific geometry of the gasifier and may not provide an accurate representation of the gasification process (Y. Wu et al., 2014). This approach can be implemented stoichiometrically by defining a set of reactions and then calculating the equilibrium composition, or non-stoichiometrically by defining the set of chemical elements in the feeding and compounds in the output and then calculating the composition that minimizes the Gibbs free energy of the system. However thermodynamic equilibrium does not seem suitable for predicting gasification gas composition in bubbling fluidized bed reactors because of the assumptions such as dimensionless gasifier, which leads to overestimation of hydrogen and carbon monoxide gases (Shi et al., 2015). On the other hand, kinetic modeling considers the specific configuration of reactors, including the geometry and operational conditions, as well as the kinetics of reduction and oxidation reactions. By incorporating these important factors, kinetic modeling provides a more accurate representation of the gasification process compared to TEM approach (Safarian et al., 2022). The inclusion of reaction kinetics allows for a more realistic prediction of gasification behavior and enables the simulation results to agree with experimental findings. This enhanced accuracy and good agreement with experimental data make kinetic modeling a valuable tool for understanding and optimizing gasification processes (Puig-Gamero et al., 2021).

Various researchers have explored different gasification parameters, employing various biomass wastes to study the gasification process. Puig-Gamero et al. (2021) used Aspen Plus to model the gasification of pine pellets and reported that increasing the gasification temperature positively influenced syngas quality by elevating the concentrations of hydrogen, carbon monoxide, and methane in the syngas. However, the study utilized gasifying air at room temperature, producing low syngas quality with up to tar concentration of 42 g/Nm^3.

Marcantonio et al. (2020) utilized thermodynamic equilibrium modeling approach in using Aspen Plus to simulate the removal of tar and other inorganic compounds. They reported a reduction of 1 g/Nm^3 and 1 ppm for tar and inorganic contaminants respectively. Thermodynamic equilibrium modeling does not consider gasifier geometry, and thus may fail to capture the intricacies of the gasifier (Safarian et al., 2022). In their study Ngamchompoo and Triratanasirichai (2017) utilized fixed-bed downdraft gasifier to investigate the effect of air temperature on gas composition and reported improved concentration of combustible gas species. The additional energy provided by air preheating facilitates endothermic reactions, achieving improved gas yields and enhanced syngas quality. Although air preheating enhances syngas quality, syngas produced from fixed bed gasifiers is of low energy density and contains high amount of tar (Samiran et al., 2016).

According to various studies, tar in syngas can be reduced by increasing the gasifier temperature. Puig-Gamero et al. (Puig-Gamero et al., 2021) studied biomass gasification using Aspen Plus modeling. They varied the equivalence ratio, which ranged from 0.17 to 0.35, and the gasification temperatures, which varied between 709 °C and 859 °C. They observed that increasing both the equivalence ratio (ER) and the temperature decreased tar concentration. To achieve optimal gasifier design and operation, parametric studies can be advanced to identify the gasification parameters that maximize syngas quality. These studies should focus on understanding the interplay between various gasification parameters to determine the best combination for achieving the desired syngas quality.

Researchers have utilized gasifying agents such as pure oxygen to enhance gasification performance. Bonilla et al. (Bonilla et al., 2019) conducted a study to with pure oxygen as the gasifying agent instead of air. Their reported a significant decrease in tar concentration, from 15.78 g/Nm^3 to 10.24 g/Nm^3. However, using pure oxygen in gasification is not cost effective because of the high cost of production of oxygen.

Additionally, supplying excessive oxygen may result in the production of flue gases instead of syngas (Mustafa et al., 2017).

Partial oxidation is another route that has been investigated to enhance gasification conditions. Zhao et al. (2015) used a multi-stage gasifier comprising an oxidative pyrolysis stage followed by partial oxidation, using pinewood as the biomass materials. They were able to reduce tar amount in syngas by 21 %. Partial oxidation shows promise for improving syngas quality, but its implementation is complex due to the interconnected stages, such as separate combustor and gasifier units (Pio et al., 2016; Zhao et al., 2015).

While Aspen Plus has been utilized in modeling biomass gasification, the majority of research is on parametric studies of the gasification parameters. As a result, it becomes necessary to determine the ideal range of these parameters for designing a gasification system with optimum response. In this study, response surface methodology (RSM) was employed for numerical optimization. RSM is a widely-utilized method in the field of design of experiments and is advantageous over classical optimization techniques. RSM allows for the exploration of the entire response surface, providing a comprehensive understanding of the relationship between the input variables and the response. Additionally, RSM requires a relatively smaller number of runs compared to classical optimization techniques but with fairly accurate results. This reduces time, cost, and resources required for experimentation. Furthermore, RSM provides statistical tools to assess the quality of the model fit, resulting in highly accurate regression models (Mojaver et al., 2019).

Response Surface Methodology (RSM) has been widely employed in the field of engineering for optimization purposes. Recent studies demonstrate the effectiveness of RSM in optimizing processes parameters to achieve improved system performance. For instance, RSM was successfully applied to optimize the production of biodiesel from waste cooking oil (Yahya et al., 2020). Armin et al. (2022), applied RSM to optimize the process parameters of a plasma co-gasification of municipal solid waste and coal. By considering factors such as steam-to-fuel ratio, temperature, and waste-to-coal blending ratio, the optimal parameters that maximized hydrogen and syngas production were determined. Chalermsinsuwan et al. (2023) employed RSM to optimize the gasification parameters using medical masks as the biomass waste. They varied pressure, steam-fuel ratio, and the gasification temperature and identified the optimal conditions that improved syngas quality by improving hydrogen production and cold gas efficiency.

While most optimization studies on gasification have focuesd on maximizing optimization goals, it is also important to consider presence of tar in syngas as an undesirable output. To address this, RMS technique can be further developed to include optimization goals with minimizing objective function that allows to incorporate additional output responses such as tar concentration.

2.9 Summary of the Research Gaps

The identified research gaps from the literature review can be summarized as follows:

i. Experimental measurements of fluidized bed hydrodynamic parameters are challenging due to the elevated temperatures involved in operating fluidized bed units.
ii. Existing studies using fluidized bed hydrodynamics numerical modeling have mainly focused on ambient temperature conditions, with limited investigations conducted at elevated temperatures and primarily focused on heat transfer.
iii. The majority of numerical simulations have utilized 2D models, which fail to capture the non-axisymmetric nature of cylindrical fluidized bed units and the non-uniform flow of fluidizing gas associated with perforated gas distributors.
iv. Gasification experiments are challenging and time-consuming due to the high-temperature conditions involved.
v. Most gasification studies are conducted with raw atmospheric air at ambient temperature, resulting in low-quality syngas with high tar content. Additionally, supplying air at ambient temperature causes a sudden reduction in temperature and loss in gasification efficiency.

vi. There are limited studies on gasification process optimization, with the majority of studies focusing on parametric analysis. The few available optimization studies are on maximizing gasification outputs.

vii. There is a scarcity of numerical simulation studies on biomass gasification that incorporate tar formation.

This research will address all the gaps mentioned above.

CHAPTER THREE

METHODOLOGY

This chapter presents materials and methods used in the study. The materials include inert silica sand as the bed materials and macadamia nutshells as the feedstock. The inert silica sand was studied to investigate its hydrodynamic behavior, which play a vital role in the design and operation of bubbling fluidized bed systems. Moreover, characterization of the biomass waste was performed for ultimate and proximate analysis. Biomass waste characteristics are important in the design of fluidized bed systems and determine characteristics of the final gas product. The study methods included both experiments and numerical simulations, with the experiments serving to validate the numerical models.

3.1 Biomass Waste Characterization

The as received (ar) macadamia nutshells and the characterization methods employed to analyze their properties are discussed. These properties play a crucial role in evaluating the gasification performance in a bubbling fluidized bed reactor and directly influence the gasifier operating conditions, including process temperatures and the amount of biomass supplied to the gasifier.

3.1.1 Proximate Analysis

The properties of a fuel, including moisture content, ash content, fixed carbon, and volatile matter, provide valuable insights into its characteristics. Reference methods for characterizing macadamia nutshells and their proximate properties are presented in Table 3.1. These properties play a vital role in estimating the behavior of a feedstock during thermo-chemical conversion processes.

Table 3.1: Standards for Biomass Waste Characterization

Characterization	Parameter	Reference method
Moisture	Water in sample ar	CEN-TS 14774-2:2009
Proximate analysis	Volatile matter	CEN-TS 15148:2009
	Ash content	CEN-TS 14775:2009
	Fixed Carbon	By difference
Calorific value	Gross calorific value	CEN-TS 14918:2009

Source: (ISO, 2015)

a) Moisture Content

The moisture content of biomass fuel affects the water content and the carbon monoxide to hydrogen ratio composition of the product gas. Additionally, when more water is taken into the reactor, more heat energy will be required in the gasifier to evaporate the moisture. More water will therefore create unnecessary evaporation which will lower the product gas heating value. High moisture content in biomass materials can also cause ignition and combustion problems during gasification. Usually, 15 % or lower water content is advised for most biomass feedstock.

The moisture content in the biomass was determined according to CEN-TS 14774-2:2009 standard. CEN-TS 14774-2:2009 is a technical specification published by the European Committee for Standardization (ISO, 2015). It provides guidelines and standardized methods for determining the moisture content in biomass samples. In order to test a single sample, an empty crucible with a lid was dried inside an oven at 105 °C, and then cooled to room temperature. The mass of the crucible with lid was measured using OHAUS PA1602 digital scale, with a sensitivity of 0.01 g and an accuracy of 1 %, and then recorded as m_1. One gram of sample was then spread evenly over the crucible and then placed in the oven with the lids next to it. The mass of the crucible, biomass sample and the lid were recorded as m_2 and then dried in an oven at 105 °C for 2 hours. After heating, the lid was placed on the crucible and cooled to room temperature. The purpose of the lid was to prevent biomass from absorbing moisture, since biomass is hygroscopic. The resulting mass was recorded after heating as m_3. The process was repeated three times to ensure the repeatability of the test samples. The moisture content (M_s) was calculated from the expression shown in Equation (3.1) (Ganesh et al., 1990).

$$M_s = \left(\frac{m_2 - m_3}{m_2 - m_1}\right) \times 100 \qquad 3.1$$

where m_1 is the mass of the empty crucible and lid in grams; m_2 is the mass of the crucible, lid and biomass in grams before heating; m_3 is the mass of the crucible, lid and residue in grams after heating.

b) Ash Content

Ash content is an important consideration when designing the gas distributor of the fluidized bed gasifier. It is defined as the mass of inorganic material left after ignition of fuel under specified conditions. High ash content could lead to clogging of the gas distributor leading to de-fluidization of the entire gasifier bed. It, therefore, means that low ash content of the macadamia nut shells is advantageous when designing the distributor plate of a fluidized bed gasifier.

Ash content was determined using CEN-TS 14775:2009 standard, which is a technical specification developed by the European Committee for Standardization that provides guidelines and procedures for the determination of ash content in solid biomass fuels (ISO, 2015). A crucible was put in the furnace at a temperature of 550 °C for one hour to remove any volatile material. The crucible was then removed and allowed to cool for 10 minutes, to room temperature and its mass was recorded as m_1. One gram of the biomass sample was spread over the crucible and the resulting mass was recorded as m_2. The crucible with the biomass sample was placed in the furnace and the temperature was raised to 250 °C for one hour to remove the volatiles before ignition. The furnace temperature was then raised to 550 °C for another half an hour to ensure complete combustion. The crucible was then removed from the furnace and allowed to cool for about 10 minutes to room temperature and the mass was recorded as m_3. Percentage ash content (As) was calculated using Equation (3.2) (ISO, 2015).

$$A_s = \frac{m_3 - m_1}{m_2 - m_1} \times 100 \qquad 3.2$$

where m_1 is the mass of the empty crucible in grams; m_2 is the mass of the crucible and the test sample in grams; m_3 is the mass of the dish and ash in grams.

c) Volatile Matter and Fixed Carbon

Volatile matter refers to the portion of the biomass that can be easily vaporized or converted into gas when subjected to high temperatures. Fixed carbon is the remaining mass after release of volatiles (Komarova et al., 2015). The ratio of volatiles to fixed carbon indicates the biomass reactivity since volatile compounds tend to react more rapidly than fixed carbon. The knowledge on the volatile amount in the biomass feedstock is necessary in the design of the gasifier system because it contributes to the formation of tars in the product gas.

Volatile mater was determined according to CEN-TS 15148:2009 standards (ISO, 2015). First, the moisture content of the biomass was determined by drying a separate sample at 105 °C as detailed above. For the volatile matter, one gram of biomass sample was placed in a crucible, and a lid was placed on it. The crucible was then transferred into a muffle furnace, which was purged with nitrogen to create an inert atmosphere, and heated at 925 °C for 7 minutes After this period, the crucible was removed, allowed to cool, and weighed. The percentage of volatile matter was calculated from the loss in mass of the sample due to heating, excluding the initial moisture content. The volatile matter (VM) was calculated using Equation (3.3) (Ganesh et al., 1990).

$$VM_s = \frac{m_2 - m_3}{m_2 - m_1} \times 100 \qquad 3.3$$

Where m_1 is the mass of the empty crucible and lid; m_2 is the mass of the crucible, lid, and biomass before heating; m_3 is the mass of the crucible, lid and sample after heating.

Fixed carbon (FCs) in the biomass waste was determined from the percentage of sample mass that remained after subtracting moisture, volatile matter, and ash content from a biomass sample as shown in Equation (3.4) (Ganesh et al., 1990).

$$FC_s = 100 - (M_s + A_s + VM_s) \qquad 3.4$$

d) Calorific Value

Calorific value refers to the quantity of heat released per unit mass or volume of biomass fuel after combustion (Etim et al., 2022). It can be expressed as either gross calorific value (GCV) or lower calorific value (LCV). The GCV, measured in laboratory settings, includes the energy released from water condensation. It provides a comprehensive assessment of the fuel's heat content, accounting for the latent heat of vaporization of any water present. In contrast, the LCV represents the heat released without considering the energy from water condensation. The current study utilized a digital bomb calorimeter, model number C200/3/1 with an accuracy of 2.5 %, shown in Figure 3.1, to measure the gross calorific value.

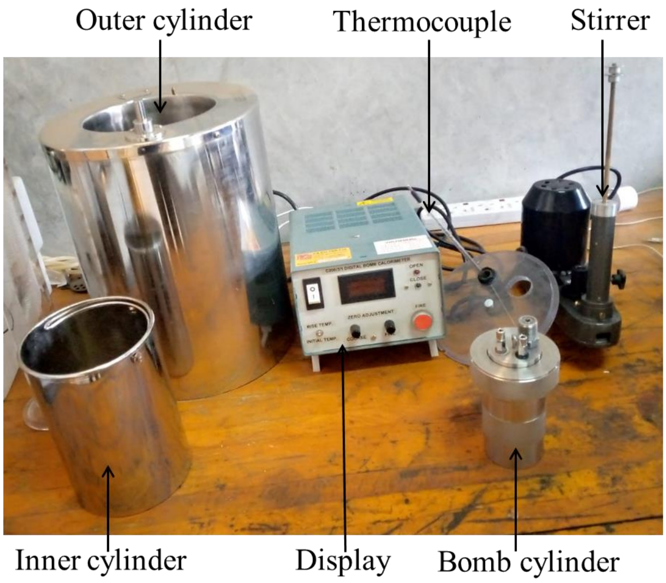

Figure 3.1: Digital Bomb Calorimeter C200/3/1

A known mass of biomass sample (m) was prepared in powder form and placed inside a sealed container (bomb) and pressurized with oxygen. Two liters of distilled water was measured in a separate calorimeter vessel and its weight recorded. The initial temperature of the water was recorded, serving as a reference point. The bomb cylinder was then submerged in the water and the sample was electrically ignited. The combustion process released heat energy, raising the temperature of the bomb and the water in the calorimeter vessel. When the equilibrium was achieved, temperatures were recorded until the temperature started to drop. The gross calorific value was then calculated using Equation (3.5)(Etim et al., 2022). Three tests were repeated and averaged to ensure repeatability.

$$GCV = \frac{(\varepsilon \times \Delta T) - Q_{fuse} - Q_{ign}}{m} \qquad 3.5$$

Where Ɛ is the effective heat equivalent of the calorimeter (11214.35J/K), ΔT is the temperature rise of the calorimeter vessel, Q_{fuse} is the heat contribution from the cotton thread (17496.6 J/g), Q_{ign} is the heat contribution from the ignition wire (1402.2 J/g)

3.1.2 Elemental Composition

Elemental composition of a biomass feedstock is determined by ultimate analysis which gives biomass elemental composition including carbon, hydrogen, nitrogen, Sulphur and oxygen. These elements are important in the computation of equivalence ratio for gasification. In this study, the ultimate analysis of biomass was determined using thermo-scientific CHNS/O Flash Smart Elemental Analyzer model 11206155 with an accuracy of 1 % and inbuilt application program. The samples were ground into fine powder before they were tested. A small portion of 0.1 g of sample was placed in the tin capsule of the elemental analyzer and then loaded. The furnace was heated at temperature of about 950 ^{o}C with a constant flow rate of oxygen-enriched helium (Cavalaglio et al., 2020). The equipment uses EagerSmart application to analyze and compute the elemental composition of Carbon, Hydrogen, Nitrogen, Sulphur and Oxygen. Table 3.2 shows the physical and chemical properties of the ‘as received’ macadamia nutshells used in this study, which are comparable to macadamia properties from other studies (Xavier, Lira, Jr, et al., 2016).

Table 3.2: Macadamia Nutshells Properties (Moisture Content (ar) = 7.35%)

Proximate (wt %)	Value	Ultimate (wt % db)	Value
Ash	0.33	Carbon	54.36
Volatile	70.64	Hydrogen	6.74
Fixed carbon	21.68	Oxygen	38.24
GCV (MJ/kg)	19.26	Nitrogen	0.33
		Sulphur	0.33

ar; as received; db: dry basis; GCV gross calorific value

3.1.3 Biomass Preparation for Gasification

Macadamia nutshells were sourced from Jungle Nuts Ltd, a macadamia nut processing company located in Thika, Kiambu County. The raw macadamia nutshells obtained were initially of large size (20-25 mm), unsuitable for direct use in a fluidized bed gasifier. To prepare them for gasification, the raw shells were dried using natural sunlight and were subsequently crushed using a ball mill crusher available at the JKUAT engineering workshop. Sizing was achieved through mechanical sieve analysis, using sieve sizes of 2000 and 4000 μm, to obtain size range of 2-4 mm. This size range is suitable for feeding into fluidized bed gasifiers as recommended by previous studies (Al-Farraji, 2017; Molino et al., 2016).

3.2 Silica Sand Characterization

3.2.1 Sizing and Grading

To investigate the fluidization behavior of inert sand particles, this study utilized three particle sizes classified under group B of Geldart powder classification (Chirone et al., 2020). Group B particles are known for their favorable fluidization characteristics and are commonly utilized for fluidization processes with minimal difficulties (Fu et al., 2019). The particle size selection process included the entire range of the group B classification, ranging from low to high particle sizes, ensuring entire coverage of the group B class. The particle size ranges considered are listed in Table 3.3.

Table 3.3: Sand Particle Size Ranges

Type	**Size range [μm]**	**Category**	**Sauter mean particle diameter, dp [μm]**
Silica sand	180-250	Low	233
Silica sand	300-425	Medium	335
Silica sand	425-550	High	500

The sizing of sand was performed using the mechanical sieve analysis method (Ma et al., 2023). This method involved passing a sample of sand through a set of sieves with different mesh sizes. The sieves were stacked in order of increasing mesh size, with the finest sieve at the bottom and the coarsest sieve at the top. The sand sample was placed on the top sieve, and the stack was then mechanically shaken to facilitate the separation of particles based on their size. The sand particles that were retained by the last sieve was taken for particle size analysis. In this study, inert silica sand was used as the bed materials and Figure 3.2 shows different sand particle size ranges which resulted from the mechanical sieve analysis method.

For size distribution analysis, the particle sizer Analysette 22 NEXT was employed. This instrument utilizes a laser particle size analysis technique to accurately compute data within a measuring range of 0.01–3800 µm, ensuring precise measurement even for the smallest particles. Analysette 22 NEXT enabled the determination of the Sauter mean diameter, which was calculated using Equation (3.6) (Subramani et al., 2007).

$$d_p = 1/ \sum_{i=1}^{n} \left(\frac{x_i}{d_i}\right) \qquad 3.6$$

Where x_i is the volume fraction of the particles having an average diameter of d_i.

Figure 3.2: Inert Silica Sand (a) 180-250 μm (b) 300-425 μm (c) 425-550 μm

Figure 3.3 depicts the results for the size distribution analysis of the sand particles under consideration. The graph demonstrates that all the sizes analyzed exhibited a narrow particle size distribution. This observation is significant as it suggests a reduced probability of bed segregation and de-fluidization occurring. When the particle size distribution is narrow, it implies that the range of particle sizes is relatively close, with fewer variations between smaller and larger particles. This characteristic enhances uniform fluidization and promotes bed stability. A narrow size distribution ensures that smaller particles are not trapped between larger particles, leading to a uniform and stable fluidization process (F. Njuguna et al., 2023).

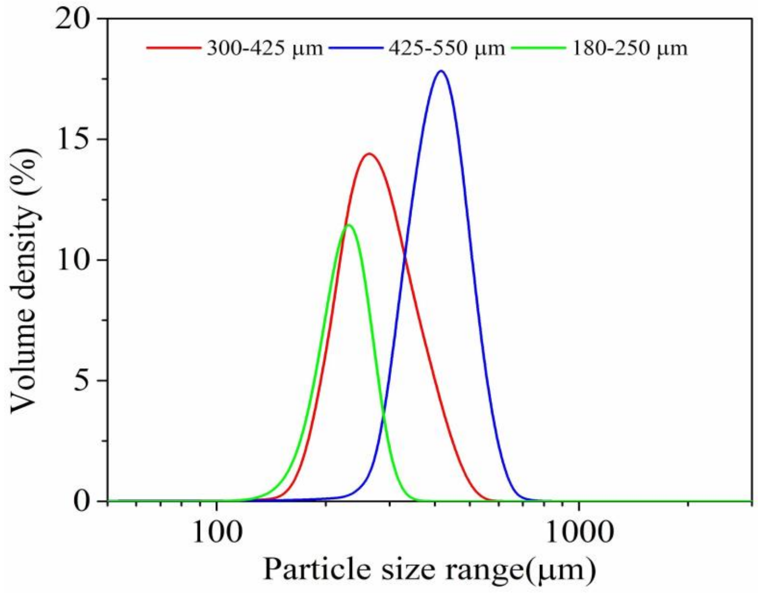

Figure 3.3: Particle Size Distribution for Different Sizes of Inert Silica Sand

3.2.2 Sand Bulk Density

A density pycnometer of 100 ml capacity, was utilized to determine the bulk density of sand (λ_S). The mass of the empty and dry pycnometer (m_0) was determined using an OHAUS digital scale, with a sensitivity of 0.01 g. The pycnometer was then filled to approximately one-third of its capacity with sand particles, and the weight of the pycnometer with the sand (m_1) was recorded. Distilled water was then added to the pycnometer, ensuring that it completely filled the pycnometer, including its capillary hole. The pycnometer, containing both sand and water, was placed in a thermostatic bath to adjust the temperature to 20 °C, ensuring thermal equilibrium. Once the temperature was stabilized, a filter paper was used to dry the water that leaked through the capillary hole. The weight of the pycnometer with the water and capillary (m_2) was recorded. Using the recorded measurements, the density was calculated using Equation (3.7).

$$\lambda_S = \frac{(m_1 - m_0)}{V_{sand}} \qquad 3.7$$

Where;

$$V_{Sand} = \frac{m_2 - m_0 - (m_1 - m_0)}{\rho_{water}} \qquad 3.8$$

3.3 Design and Fabrication of the Experimental Setup

This section focuses on the design and fabrication of a bench-size fluidized bed unit, for experimental studies. Figure 3.4 illustrates a schematic diagram of the fluidized bed unit, which comprises several components such as the bubbling fluidized bed reactor (including the plenum chamber and distributor plate), an air preheating system with temperature controllers, an air delivery system, a fluidized bed heating system with temperature controllers, and a cyclone separator. These units were designed and constructed within JKUAT mechanical engineering workshops.

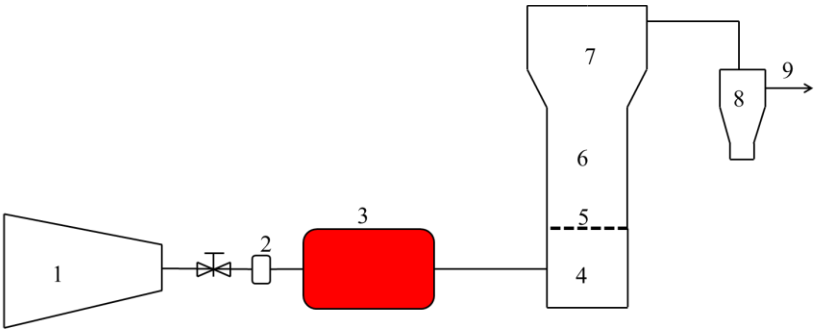

1 air compressor; 2 air flow meter; 3 air preheater; 4 plenum chamber; 5 air distributor; 6 fluidized bed section; 7 freeboard area; 8 cyclone separator; 9 to the gas storage bag

Figure 3.4: Schematic Diagram of a Fluidized Bed Gasifier Unit

3.3.1 Gasifier Design

The gasifier is the most important component in the gasification process, where fluidization and chemical reactions occur between the biomass waste and the gasifying agent. The gasifier comprises the plenum chamber, the distributor plate, fluidized bed section, and the freeboard area. These components are responsible for facilitating the gasification process, allowing for efficient interaction between the biomass waste and the gasifying agent, thereby enabling the desired reactions to take place. The following discussion entails the design process of the fluidized bed system employed for the experimental studies.

a) Reactor Column Cross-Sectional Area

Fluidized bed gasifiers are utilized for the conversion of biomass wastes into syngas. The gasifier operates by introducing two primary inputs: biomass waste and the gasification agent. When air is utilized as the gasification agent, heat generation occurs within the reactor by carefully controlling the equivalence ratio, which represents the ratio of air to biomass waste. Consequently, a single bubbling gasifier design is employed. In this study, air was employed as the gasifying/fluidizing agent and was preheated to enhance the gasification performance.

The design process for determining the internal cross-sectional area of the reactor column in a gasifier involved several steps, with the initial step being the selection of the fuel throughput. Secondly, an appropriate value for the equivalence ratio ER) was assumed. It is recommended that the value of ER should falls between 0.15 and 0.35 for gasification (Puig-Gamero et al., 2021). An equivalence ratio below 0.15 tends to favor pyrolysis, producing high amount of tar in syngas. On the other hand, an equivalence ratio exceeding 0.35 leans toward combustion, where the fuel is predominantly burned to produce more fumes in syngas (Puig-Gamero et al., 2021). The next step was to estimate the required rate of air supply for the gasification process based on the selected fuel. Finally, the inert particle size was chosen and the inside cross-sectional area was estimated to ensure that the superficial gas velocity remained within an acceptable limit for the selected particle size.

In the design of a bubbling fluidized gasifier, macadamia biomass waste was selected as the primary biomass feedstock, while sand was chosen as the inert bed material. The relevant properties of biomass waste and the silica sand material, given in Table 3.2 and Table 3.3 were taken into account during the design process.

b) Biomass Waste Stoichiometric Air Requirements

The air-fuel ratio is a critical parameter that significantly influences the performance of the gasification system. It is quantified as the equivalence ratio (ER), representing the ratio between the actual amount of air supplied per unit mass of fuel introduced into the gasifier and the stoichiometric air requirement as shown in Equation (3.9).

$$ER = AF_a / AF_s \quad 3.9$$

Where AF_a is the actual air-biomass ratio and AF_s is stoichiometric air -biomass ratio.

Gasification relies on the partial oxidation process of biomass waste, requiring the oxygen supply to be lower than the stoichiometric amount corresponding to the biomass quantity. The determination of the stoichiometric air flow rate was based on the complete combustion of carbon (C), hydrogen (H), and sulfur (S) as determined from the ultimate analysis. Nitrogen (N) was not considered in the combustion calculation since the gasification temperature falls below the threshold required for nitrogen conversion to nitrogen oxides (NOx) (Al-Farraji, 2017). The combustion chemical reactions involving the combustible species present in the fuel are depicted in the three reactions provided in (3.10), (3.11) and (3.12). The stoichiometric amount of oxygen required for these reactions was determined.

$$C + O_2 \rightarrow CO_2 \quad 3.10$$

$$H_2 + 0.5O_2 \rightarrow H_2O \quad 3.11$$

$$S + O_2 \rightarrow SO_2 \quad 3.12$$

Table 3.4 shows the atomic weight of the selected gases in the calculation of the stoichiometric amount of oxygen.

Table 3.4: Atomic Weights of Gases

Gas	Atomic weight (kg/Kmol)
Hydrogen	1.01
Carbon	12.01
Nitrogen	14.01
Oxygen	15.999
Sulphur	32.06

To determine the total stoichiometric oxygen required, the oxygen quantities for reactions (3.8) to (3.10) were summed while subtracting the inherent oxygen content present in the biomass fuel. Table 3.5 demonstrates air-fuel stoichiometric calculation for the selected biomass waste. Subsequently, the actual air-fuel ratio was determined based on the given equivalence ratio using the Equation (3.13).

$$(AFR)_a = ER \times (AFR)_s \tag{3.13}$$

where $(AFR)_a$ is actual air fuel ratio, $(AFR)_s$ is stoichiometric air fuel ratio.

The volumetric flow rate was determined from the expression in Equation (3.14).

$$\dot{m}_{air} = \dot{v}_{air} \times \rho_{air} \tag{3.14}$$

Where $\dot{m}_{air}$ is the mass flow rate of air, $\dot{v}_{air}$ is the volumetric flow rate of air and ρ_{air} is the air density.

Previous studies have indicated that the feed rate for laboratory-scale fluidized bed gasifiers usually falls within the range of 1 to 10 kg/h (Bonilla and Gordillo, 2017; Naryanto et al., 2020). In this study, the estimated feed rate for the gasifier was approximated at 15 kg/h, which is about one and a half times the throughput of a typical laboratory-scale biomass fluidized bed gasifier. It was determined from Table 3.5 that gasification process with an equivalence ratio of 0.4 would require approximately 2.78 g of air for the gasification of every gram of fuel. The huge values for ER and biomass feed rate were selected in the preliminary design to allow for any operational adjustment in the future. Based on this information, the gasification of 15 kg/h of biomass fuel would require an approximate air flow rate of 42 kg/h.

Table 3.5: Stoichiometric Air-Fuel Ratio

Combustion	**Fuel Composition**			**Stoichiometric Oxygen requirement (g)**
		% wt	**1 g basis**	
	C	54.36	0.5436	1.448182
	H	6.74	0.0674	0.534919
	O	38.24	0.3824	-0.3824
	N	-	-	-
	S	0.33	0.0033	0.003294
Total oxygen requirement				1.6
Total air requirement for complete combustion				6.96
Total air requirement for ER=0.4				2.78

In order to achieve optimal performance of the gasifier, it is essential to ensure that the superficial velocity of the gas passing through the particle bed, within the selected cross-sectional area, falls between the velocities required for minimum fluidization and terminal velocity (Grace et al., 2020). Bubbling fluidized gasifiers are designed and operated at flow rates that are typically 1.5-3 times the minimum fluidization velocity (Al-Farraji, 2017). However, for the purposes of this study, a design point of 4 times the minimum fluidization velocity was chosen to provide an additional safety margin. The physical properties of silica sand and air considered in the design are provided in Table 3.6.

Table 3.6: Properties of Air and Silica Sand

Parameters	Unit	Value
Particle size, dp	m	0.0005
Particle density ρ_p	kg/m^3	2750
Gas dynamic viscosity	Kg/m.s	1.83×10^{-5}
Air density ρ_g	kg/m^3	1.2
Minimum fluidization velocity, U_{mf}	m/s	0.23
porosity (ε), solid volume fraction (ε_p)		0.44, 0.56
Terminal velocity (Ut)	m/s	4

Source: (Eslami Afrooz et al., 2016)

c) The Reactor Height

Carbon conversion efficiency is influenced by the retention period of the biomass within the gasifier and the gas residence time. These parameters are influenced by the height of the gasification column (Al-Farraji, 2017). The overall height (H_t) of the reaction chamber was determined using Equation (3.15) (Fair and Walas, 2012).

$$H_t = TDH + H \qquad 3.15$$

The total disengagement height (TDH) was calculated based on the correlation shown in Equation (3.16), while the maximum expanded heigh (H) was computed using Equation (3.17).

$$\frac{TDH}{D} = (2.07D^{-0.3} - 0.7)exp(0.7U \times D^{-0.23}) \qquad 3.14$$

$$H = L.rH \qquad 3.17$$

where H is the total maximum expanded height, r is the bed expansion ratio taken as 1.5 for bubbling fluidized beds and L is the minimum bubbling height, expressed as shown in Equation (3.18) (Fair and Walas, 2012).

$$L = \frac{4m}{\rho_p\,(1-\varepsilon)\pi D^2} \qquad 3.18$$

Where m is the mass of bed materials.

To avoid material entrainment, an expansion was made to the upper portion of the freeboard in the gasifier. In this design, the height of the freeboard was selected as 4.5 times the internal diameter, while the remaining height was designated as the height of the fluidized bed section (Grace et al., 2020). A freeboard diameter 0.2 times the height of the fluidized bed section, was selected based on the design of Sánchez-Prieto et al. (Sánchez-Prieto et al., 2014).

Biomass gasifiers are typically operated within the pressure range of 1 to 10 atm (Szul et al., 2021). For the current study, a maximum internal pressure of 15 atm was chosen for the design under consideration. The determination of the reactor wall thickness was based on the hoop stress (σh) as shown in Equation 3.19 (Vullo, 2014). A maximum allowable stress of 12.9 ksi was taken into consideration for stainless steel grade 316L under elevated temperatures, leading to a reactor wall thickness of approximately 0.9 mm.

$$\sigma_h = pD/2t \qquad 3.19$$

Where p, D, and t are the internal pressure, diameter of the reactor and the reactor wall thickness respectively. Table 3.7 shows the summary of the calculated design values while Figure 3.5 and Figure 3.6 show the working drawings of the fluidized bed column.

Table 3.7: Calculated Design Values

Item	Value
Volumetric flow rate	0.0098 m^3/s
Superficial gas velocity	0.92 m/s
Bed inner diameter	110 mm
Gasifier height	1280 mm
Disengagement; Expandable height	1060; 220 mm
Fluidized bed; Freeboard height	780; 500 mm
Freeboard diameter,	150 mm
Wall thickness	1 mm

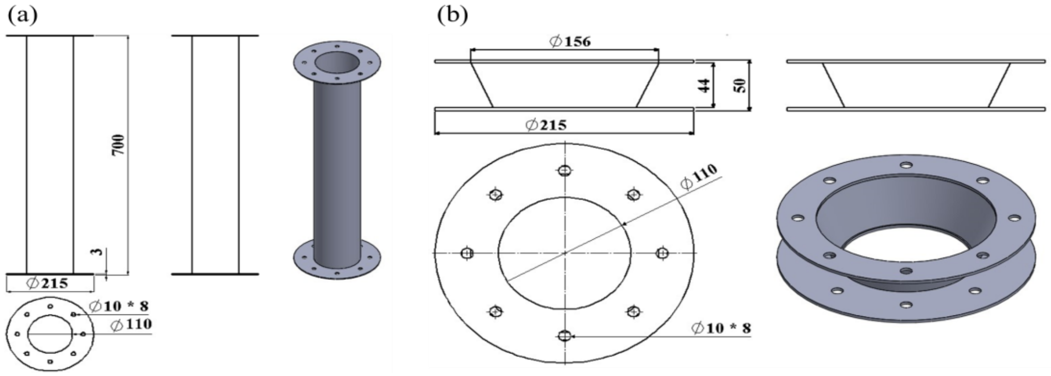

Figure 3.5: (a) Fluidized Bed Section (b) Fluidized Bed-Freeboard Sections Connector

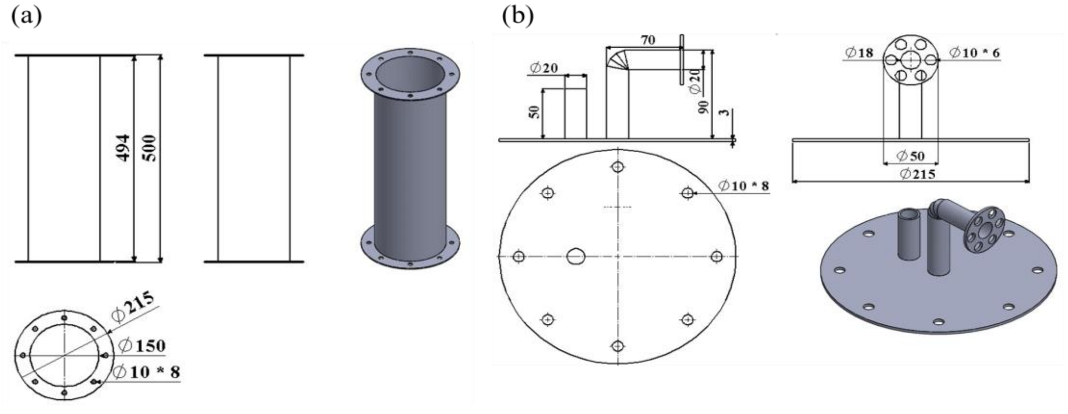

Figure 3.6: (a) Freeboard Section (b) Freeboard Section Cover

3.3.2 The Plenum Chamber

The role of the plenum chamber was to ensure even distribution of air underneath the air distributor. However, to minimize pressure drop at the distributor plate, it was important to address the potentially high kinetic energy of the incoming air in the central core. This high-energy air jet tends to exhibit preferential flow, concentrating at the point of impact on the distributor. As a result, additional resistance is encountered as the air spread across the distributor, including its corners. To address this, the distributor plate was positioned at a distance H_b above the air supply pipe, based on Equations (3.20) to (3.22) (Al-Farraji, 2017).

$$H_b = 0.2D_t + 0.5D_p \; for \; D_p > D_t/100 \qquad 3.20$$

$$H_b = 18D_n \; for \; D_p < D_t/100 \qquad 3.21$$

$$H_w = 6H_b \qquad 3.22$$

D_t denotes the fluidized bed internal diameter, D_p the air supply pipe diameter and H_w the height of the plenum chamber. A 20 mm pipe was selected to deliver air to the gasifier, resulting in a plenum chamber height of 200 mm. Stainless steel grade 316L was chosen for the plenum chamber due to its excellent corrosion resistance and high temperature tolerance. Figure 3.7 depicts the working drawing of the plenum chamber.

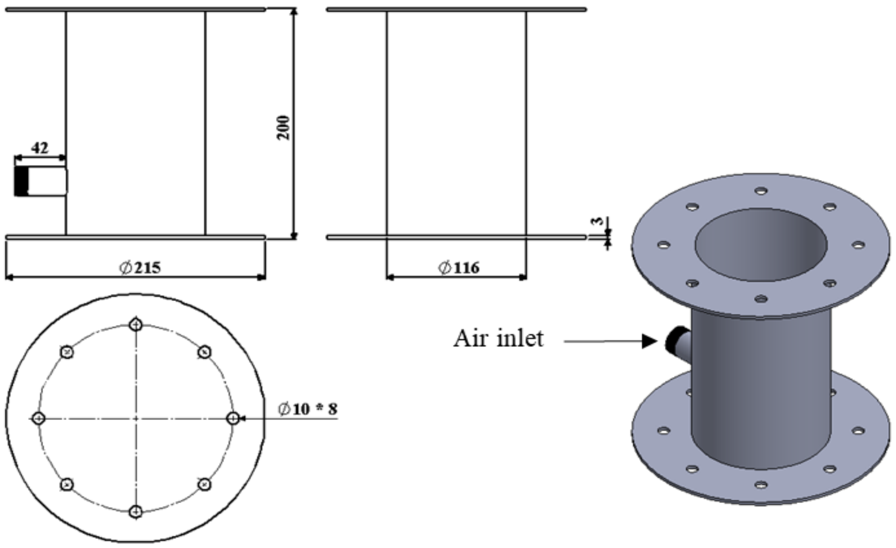

Figure 3.7: Plenum Chamber

3.3.3 Air Distributor Plate

The distributor plate distributes the fluidizing gas uniformly across the bed's cross-sectional area while providing support for the biomass and inert bed materials. The design of a fluidized bed typically revolves around the pressure drop, and it is crucial to ensure that the pressure drop across the gas distributor plate meets the requirements at the minimum fluidization velocity. This is necessary to achieve uniform gas distribution and proper fluidization of the bed. A generally accepted guideline for satisfactory fluidized bed performance is that the ratio of the distributor pressure drop to the bed pressure drop should fall within the range of 0.1-0.4 (Mori and Moriyama, 1978). When designing the distributor plate, a key consideration is to ensure that all orifices remain open under all operating conditions to maintain effective gas distribution. The pressure drop across a bubbling bed of height (H) was calculated from Equation (3.23) (Mori and Moriyama, 1978). A bed aspect ratio of two was selected, indicating a bed which was neither shallow nor deep. Additionally, it allowed for proper gas-solid contact and residence time, promoting effective heat and mass transfer while avoiding excessive back mixing or channeling effects (Sathiyamoorthy and Horio, 2003).

$$\Delta P_b = \rho_p . (1 - \epsilon). H. g \qquad 3.23$$

The relationship between the number of orifices of diameter d_o, per unit area of the distributor (N), the orifice velocity (U_{or}), and the superficial gas velocity (U) can be determined by considering the fractional open area (A_o) of the air distributor plate using the mass balance Equation (3.24).

$$N \times \frac{\pi}{4} \times d_o^2 U_{or} \rho_{gor} = U \rho_g \qquad 3.24$$

$$A_o = N \times \frac{\pi}{4} \times d_o^2 = \frac{U \rho_g}{U_{or} \times \rho_{gor}} = \frac{U}{U_{or}} \qquad 3.25$$

where N depends on the arrangement of orifices on the plate and the pitch P as follows.

For triangular pitch;

$$N = \frac{2}{\sqrt{3} \times P^2} \tag{3.26}$$

For square pitch;

$$N = \frac{1}{P^2} \tag{3.27}$$

The gas velocity through an orifice U_o is related to the pressure drop through the grid as shown in Equation (3.28). An orifice coefficient C_d of 0.8 is suited for many gas-solid fluidized bed applications and was used in the current design (Basu, 2006).

$$U_o = C_d \times \left[\frac{2\Delta P_d}{\rho_{gor}}\right]^{0.5} \tag{3.28}$$

An excessively high orifice velocity may lead to the attrition of bed particles. Orifice velocities less than 60 m/s are generally considered safe, while any value above 90 m/s is considered risky (Grace et al., 2020). From Equations (3.25) and (3.28), a fractional open area of the perforated plate and an orifice velocity of 2 % and 49.5 m/s, respectively, were obtained. Subsequently, a perforated distributor plate having 89 holes of 1.5 mm diameter each, and a triangular configuration of 10 mm pitch was arrived at. Triangular holes configuration was preferred because of their better performance compared to square arranged holes since they have a better flow distribution (Al-Akaishi et al., 2017). Figure 3.8 shows the dimensions of the air distributor plate, which was designed and constructed from stainless steel grade 316L.

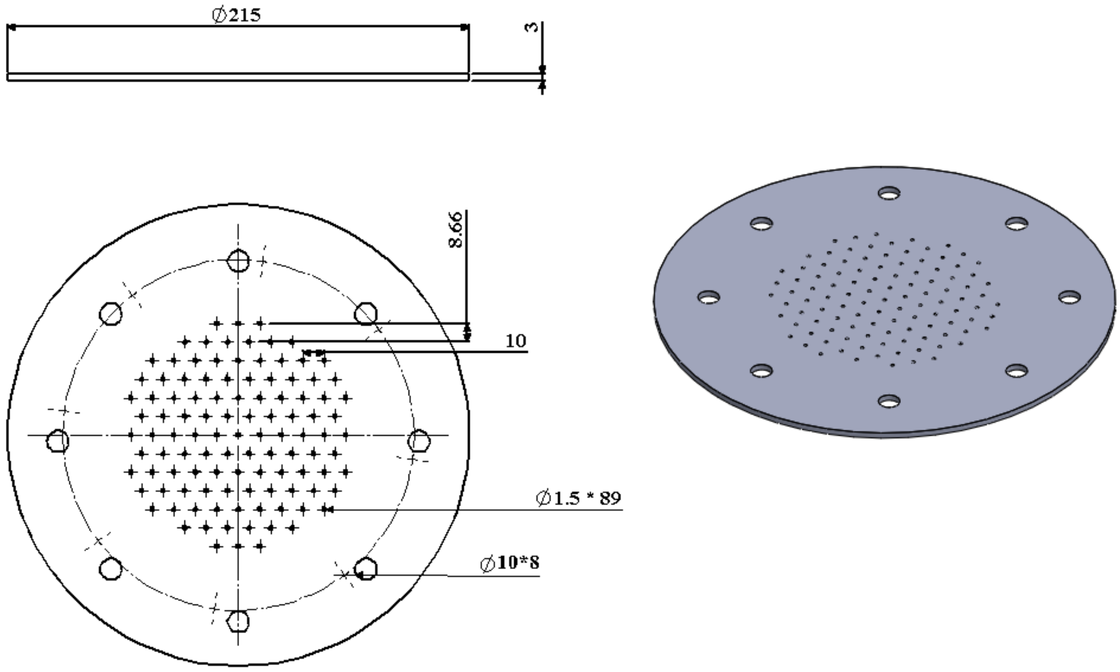

Figure 3.8: Air Distributor Plate

3.3.4 Cyclone Separator

The cyclone separator is a widely used equipment in various industries for the separation of solid particles from gas. Variours cyclone separator designs have been proposed in literature as shown in Table 3.8.

Figure **3.9** shows the dimensions of a typical cyclone design . For the current study, the collection efficiency of the particles was considered as the key design consideration because of the fine ash particles. The resulting design of the cylone separator, which was constructed using stainless steel grade 316L, is shown in Figure 3.10.

Table 3.8: Industrial Cyclone Separator Standard Designs

Duty	High efficiency	High throughput	General purpose
d	1.0	1.0	1.0
a/d	0.5	0.75	0.5
c/d	0.5	0.75	0.5
e/d	0.5	0.875	0.625
h/d	1.5	1.5	1.0
H/D	4.0	4.0	4.0
b/d	0.375	0.375	0.25

Source: (Simulation, 2010).

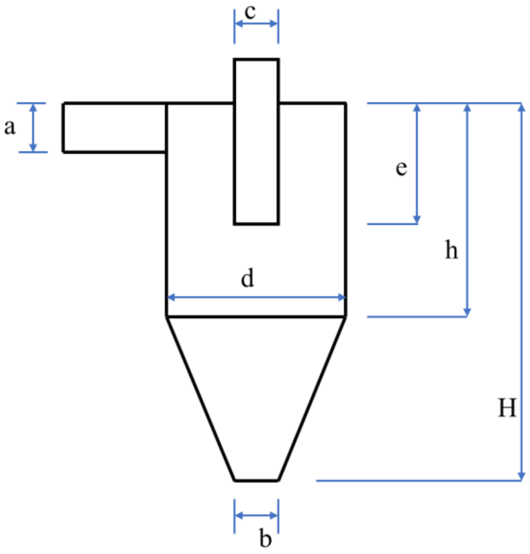

Figure 3.9: Typical Cyclone Separator Designs

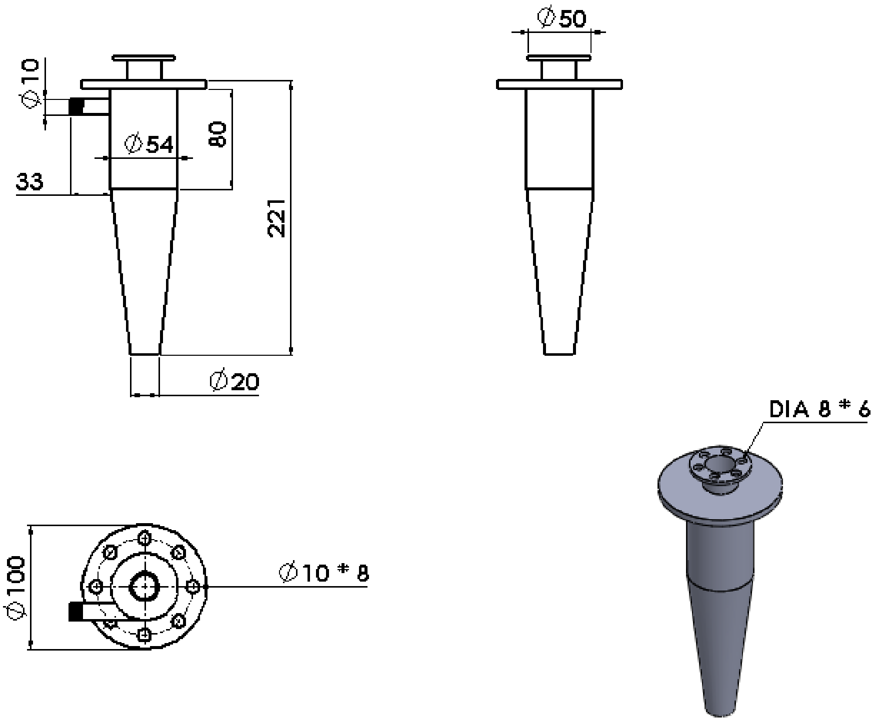

Figure 3.10: Cyclone Separator

3.3.5 Heat Energy Requirements

This section presents the design considerations for meeting the energy requirements of heating the bed materials and the gasifying air. It also covers thermal insulation, temperature regulation, and control.

a) Bed Heating System

Silica sand was heated directly from the room temperature to 500 ^{o}C, which was selected as the pyrolysis temperature, using dedicated electrical heating system. Table 3.9 shows the parametrs that were used for the design of the heating system. The amount of sand occupied a bed aspect ratio of 2 (H=2D). An aspect ratio of 2 was selected to ensure a neither too deep nor too shallow bed (Qizilbash and Malik, 2015). Additionally, a higher margin of 1.5 was included in the temperature to allow for an adequate supply of heat to the sand, ensuring that the desired temperature could be achieved and maintained effectively.

Table 3.9: Bed Heating System Design Parameters

Parameter	Value	Remarks
Silica sand mass (Kg)	6.88	Mass occupied by H=2D
Cp (J/Kg°C)	804	(Falciglia et al., 2015)
Initial temperature (°C)	25	Room temperature
Final temperature (°C)	750	1.5 times pyrolysis temperature
Electric heater rating (kW)	6	High rating to save space
Thickness of the column (mm)	3	For strength of the gasifier column
h (W/m^2): inside, outside	25, 5	(Falciglia et al., 2015)
k (W/mk) -Stainless steel	22.6	(Falciglia et al., 2015)

The overall heat required was calculated by considering the heat energy required to heat the sand and the heat loss resulting from radial heat loss due to radiation, convection and conduction heat transfer. The energy required (Q) to heat the bed sand material was calculated using Equation (3.29).

$$Q_{sand} = mCp\Delta T \qquad 3.29$$

where m is the mass of silica sand Cp is the specific heat capacity of silica sand and is the temperature change.

Radial heat transfer (1D heat transfer) was assumed considering that the gasifier column length (L) was much longer (1.4 m) relative to the diameter of the column (0.11 m). Radiative heat loss was based on Stefan-Boltzmann Equation (3.30) (Kreith and Manglik, 2016).

$$Q_{Rad} = 2\pi L\sigma\varepsilon T^4 \qquad 3.30$$

Where σ, ε, T are the Stefan-Boltzmann coefficient, emissivity of and temperature respectively.

Heat lost due to conduction and convection was based on Fourier's Law, expressed in Equation (3.31)

$$Q_{loss} = \Delta T/R_t \qquad 3.31$$

where Rt is the total thermal resistance due to convection and conduction expressed in the following equations.

$$Rt_{total} = Rt_{conv} + Rt_{Cond} \tag{3.32}$$

$$Rt_{conv} = \frac{1}{2\pi r_2 Lh} \tag{3.33}$$

$$Rt_{Cond} = \frac{ln(\frac{r_2}{r_1})}{2\pi Lk} \tag{3.34}$$

where L, k and h are the length of the fluidized bed column, thermal conductivity of stainless steel and convective heat transfer of air.

The time required to heat the silica sand was calculated using the Equation (3.35).

$$Time\ (t) = Q/Power \tag{3.35}$$

Table 3.10 shows the calculated design values.

Table 3.10: Calculated Design Values for the Bed Heating System

Parameter	**Value**
Q_{sand} (J)	4,010,352
Q_{loss} (W)	1,526
Q_{total} (W)	2,640
Heater rating (W)	6,000
Time (Mins)	27

b) Air Preheating System

The air used for fluidization or gasification was heated using 2kW electrical heating elements before being introduced into the fluidized bed. The parameters considered in the design are presented in Table 3.11.

Table 3.11: Air Preheating System Design Parameters

Parameter	Value	Remarks
Initial air temperature (°C)	25	Room temperature
Final air temperature (°C)	750	Same as sand
Mass flow rate of air (Kg/h)	12	Fluidization and gasification experiments

The rate of heat transfer and the surface area for the heat transfer were computed using Equations (3.36) and (3.37), respectively (Marchelli et al., 2020).

$$\dot{Q} = \dot{m}Cp\Delta T \tag{3.36}$$

$$A = \frac{\dot{Q}}{U \times LM\Delta T} \tag{3.37}$$

where: Q is the heat transfer rate, $\dot{m}$ is the air mass flow rate, Cp is the specific heat capacity of air, ΔT is the temperature difference, U is the overall heat transfer coefficient, A is the surface area, and $LM\Delta T$ is the logarithmic mean temperature difference. The overall heat transfer coefficient for a plane wall and the logarithmic mean temperature difference are calculated using the Equations (3.38) and (3.39), respectively (Marchelli et al., 2020).

$$U = \frac{1}{\frac{1}{h_i} + \frac{1}{h_o} + \frac{l}{k}} \tag{3.38}$$

$$LM\Delta T = (T_2 - T_1)/ln(T_2/T_1) \tag{3.39}$$

where h_i, h_o, and k are the convective heat transfer coefficient of inside and outside air respectively and k is the thermal conductivity of material of chamber.

Residence time (t) represents the time air spends inside the preheating chamber and was calculated using Equation (3.40).

$$t = \frac{V}{\dot{V}} \tag{3.40}$$

where is the volumetric flow rate and

$$V = Ah \tag{3.41}$$

where h is the height of the air box.

The design values that were calculated are listed in Table 3.12, while Figure 3.11 shows the working drawing of the air preheating chamber.

Table 3.12: Calculated Design Values for the Air Preheater

Parameter	Value
(W)	1,600
U (W/m^2.°C)	25
Heater power rating (kW)	1 kW X 2
Dimensions	550 X 600 X 150 mm height
Time (s)	113

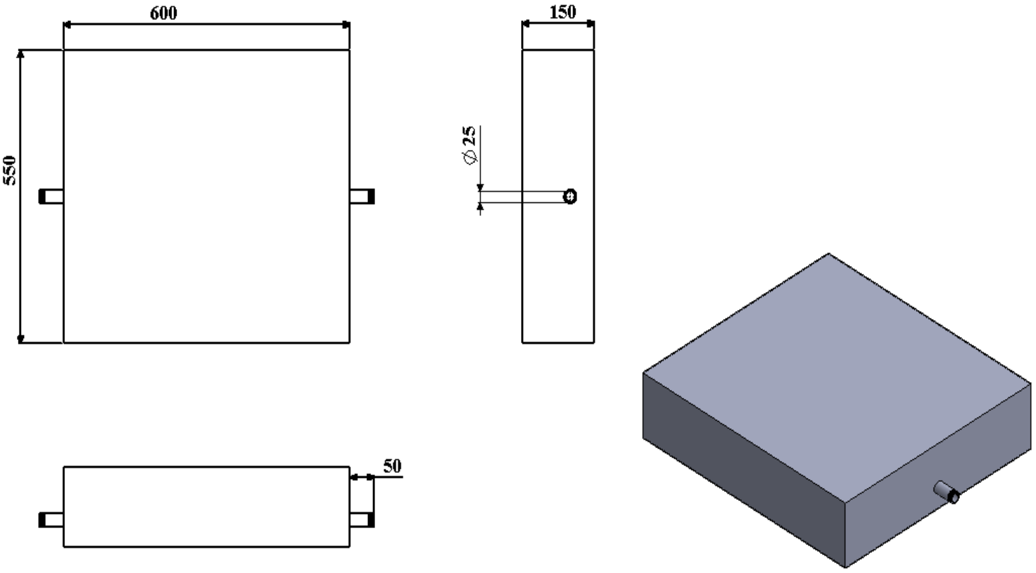

Figure 3.11: Air Preheating Chamber

3.3.6 Thermal Insulation

The gasifier was made of a stailess steel cylinder of internal diameter 110 mm and external diameter of 116 mm. It has a total height of 1400 mm, which includes the plenum chamber. Typically, gasification temperature falls within the range of approximately 600 °C to 1000 °C (Saleh and Samad, 2021). Equation (3.42), which is based on Fourier law, represents the heat transfer rate for radial conduction across a cylindrical wall and convection heat loss due to the air outside the cylinder (Marchelli et al., 2020).

$$\dot{Q}_{with\ insulation} = \frac{T_2 - T_1}{\frac{r_2}{r_1})\frac{1}{2\pi L k_1} + (ln\frac{r_3}{r_2})\frac{1}{2\pi L k_2} + \frac{1}{h(2\pi r_3 L)}} \qquad 3.42$$

where T_1,T_2, r_1, r_2, r_3, k and L are the temperature of outer wall, inner wall temperature, inner radius, outer radius of the cylinder without insulation, outer radius of the cylinder with insulation, thermal conductivity of the conducting material and the length of the gasifier column, respectively. The fiber glasswool insulation, with a thermal conductivity (k_2) of 0.35 W/m·K, was purchased from Insulation Materials Kenya Ltd. A thermal conductivity (k_1) of 25.4 W/m·K was used for stainless steel. Figure 3.12 illustrates the heat loss with the insulation material.

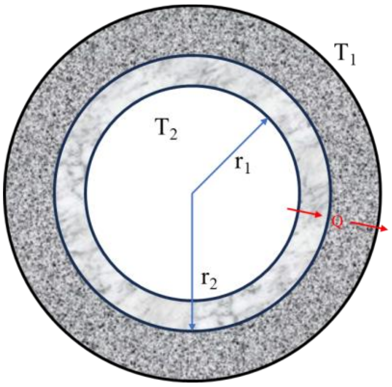

Figure 3.12: Heat Loss in Cylinders with Insulation

Figure 3.13 shows the relationship between heat loss and insulation radius. The plot showed an initial increase in heat loss with the insulation radius until reaching a critical point at 7 cm, after which it begins to decrease. An insulation thickness of 15 cm was selected considering reactor diameter.

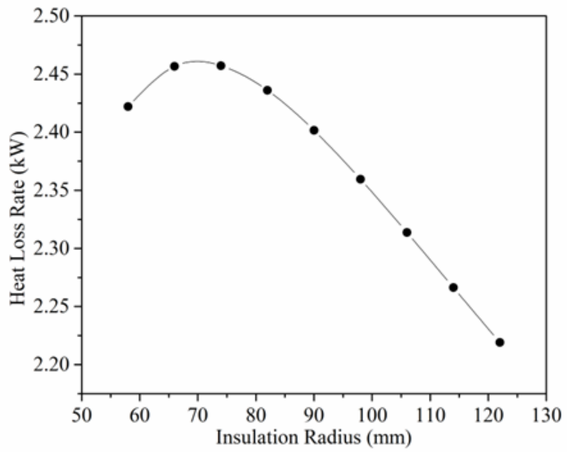

Figure 3.13: Heat Loss as a Function of Insulation Radius

3.3.7 Temperature Control System

A control system to regulate the heating process and maintain the desired temperature for the air and sand heating was selected. This was achieved by using a K-type thermoucouples connected to a PID controller. The controller monitored the temperature and adjusted the power output of the heating elements accordingly to maintain the desired temperature range.

Figure 3.14 shows the wiring diagram of the temperature controll system, comprising a Proportional-Integral-Derivative (PID) controller supported by a solid state relay (SSR). SSR provide electrical isolation between the control circuitry of the PID controller and the load circuit, offering protection to the controller from any electrical surge generated by the load. It helps in reducing interference and ensures the safety of the control system.

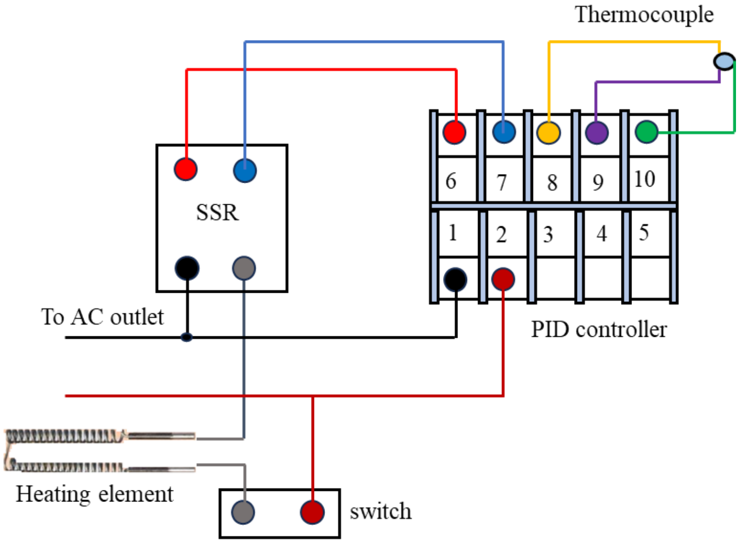

Figure 3.14: Temperature Control Wiring Diagram

3.3.8 Instrumentation

Assorted equipment and devices were used in the experimental measurements. Table 3.13 lists the specifications of the equipment used in both the fluidized bed hydrodynamics and gasification experiments. Pictorial representation of some of the experimental components is attached in the appendix section.

Table 3.13: Experimental Components

Item	Specification	Capacity
Fluidized bed section	110 mm ID X 700 mm height	-
Freeboard section	150 mm ID X 500 mm height	-
Plenum chamber	110 mm ID X 200 mm height	-
Air preheating chamber	550 mm X 700 mm X 150 mm	-
Pulsation dampener	100 mm ID X 200 mm length	-
Air compressor	IWATA	8 bar
Pressure transducers	AUTEX, Honeywell	15 psi
Rotameter	LZQ	Varied
Thermocouples	EGT K-type	1200 ^{o}C
PID temperature controller	REX-C100	0-1300 ^{o}C
Pressure data logger	DATAQ DI-2108	8 channels
Temperature data logger	NI-9211	8 channels

3.4 Experimental Measurements

Experiments were conducted to validate the simulation models by comparing the results obtained from the numerical simulations with the corresponding experimental data.

3.4.1 Materials

In the present study, the investigation of bed hydrodynamics involved the use of silica sand as the inert bed material, having a density of 2750 kg/m^3. Air was selected as the fluidizing agent for the system. To investigate the fluidized bed hydrodynamic behavior, three different particle sizes with Sauter mean diameters of 500, 335, and 233 µm were employed. The investigation on the fluidized bed hydrodynamic behavior was performed with the bed materials at a temperature ranging from 25 to 400 °C and with air at various velocities.

Gasification experimental measurements utilized the fine bed particles of 233 µm as the bed materials as this would require less fluidizing air. Macadamia nutshells were used as the biomass fuel. Fluidized bed gasification experiment was performed with the bed materials at initial temperature of 500 ^{o}C, air temperature ranging between 25 and 825 °C and the equivalence ratio ranging between 0.15 and 0.35. More details on the materials used can be found in section 3.1 and section 3.2.

3.5 Experimental Setup

The experimental setup is shown in

Figure 3.15. It consists of a high temperature transparent quartz glass tube forming the fluidized bed section and a freeboard area made up of stainless steel. The fluidized bed section is 110 mm ID and 700 mm height, while the freeboard section has 150 mm ID and 500 mm height. The quartz glass can withstand a temperature of 1200 ^{o}C and facilitates visual observation of the fluidization phenomenon. The fluidized bed column is lagged with a 10 cm thick layer of glass wool for thermal insulation but a small space is provided to observe fluidization and measure bed height.

An air distributor plate, of the description given in section 3.3.3, was placed at the bottom part of the fluidized bed column. The distributor plate ensured uniform distribution of the fluidizing air to the fluidized bed section. Below the gas distributor was a plenum chamber of 110 mm ID and 200 mm height, which served as the air holding section before its distribution, in order to avoid jetting phenomenon. A mesh with 45 µm diameter holes was placed on top of the distributor plate to avoid clogging of the distributor holes and silting of the bed material to the plenum chamber.

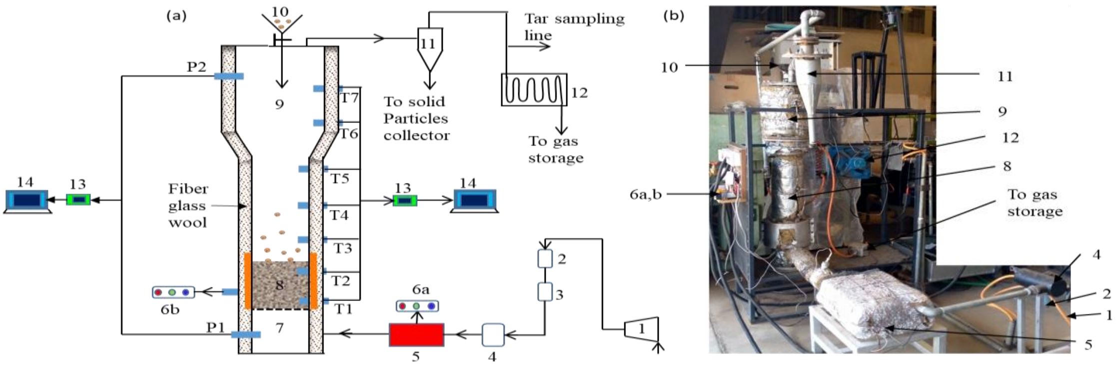

1 Compressed air, 2 Oil/Water separator, 3 Flow meter, 4 Pulsation dampener, 5 Air preheater, 6a PID Temp controller for air preheating, 6b PID Temp controller for bed heating, 7 Plenum chamber, 8 Fluidized bed, 9 Freeboard section, 10 Biomass reservoir, 11 Cyclone separator, 12 Gas cooler 13 Data logger, 14 Computer, T1-T7 Thermocouples, P1,2 Pressure transducers

Figure 3.15: Experimental Setup (a) Fluidized Bed Schematic Diagram (b) Experimental Rig

To facilitate bed and air heating, a bed heating system was provided around the lower part of the fluidized bed system, consisting of two electric heaters with a total capacity of 6 kW. Similarly, an air pre-heating chamber for was provided which comprised a stainless-steel box provided with two electric heaters each having a capacity of 3 kW. Temperature measurements and monitoring was performed using EGT K-Type thermocouples controlled using REX-C100 PID controllers which ensured the bed and air temperature was maintained within ±5 °C of the desired temperature.

The air flow rate, which was supplied from a compressor, was measured using rotameters of LZQ type with ±4% accuracy. It was passed into a NEIKO water/oil separator to remove any moisture or oil before supplying to the fluidized bed.

The experimental work majorly focused on the measurements of the bed pressure drop for the determination of the minimum fluidization point. Pressured drops through the sand bed material were measured at various air flow rates and bed temperatures. The bed pressure drop was the pressure difference across the distributor when the bed had material and when it was empty (Al-Farraji and Taofeeq, 2020). The pressure drops were obtained from the pressures measured using pressure taps P1 at the plenum section and P2 at the freeboard area. AUTEX pressure transducers having ±1% full scale accuracy, were employed to measure the pressures.

The pressure drop measurements began with an empty bed to measure the distributor plate pressure drop (ΔPDP) at the desired temperatures. Subsequently, the pressure drop of the bed containing materials (ΔPBD) was measured separately at the same desired temperatures. The overall bed pressure drop (ΔPB) for a particular temperature and air flow rate was determined using Equation (3.43).

$$\Delta PB = \Delta PBD - \Delta PDP \tag{3.43}$$

Equation (3.44) was used to calculate bed voidage at the minimum fluidization velocity (ε_{mf}). A steel rule, having a precision of 1 mm, was fixed to the quartz glass tube for measuring bed heights at inception of fluidization (H_{mf}).

$$\varepsilon_{mf} = \frac{(m/\rho_s)}{H_{mf} A_c} \tag{3.44}$$

where m and ρs are the mass and the density of the sand respectively. Ac is the cross-sectional area of the bed column.

Gasification experiments were conducted using the setup in Figure 3.15. Seven EGT K type thermocouples, T1-T7, were positioned along the gasifier height. As seen in the setup, the thermocouples were arranged to ensure sufficient coverage of the entire gasification zone for temperature profile assessment. In addition, a cyclone separator and a heat exchanger were incorporated to remove ash particles and cool the syngas, respectively, prior to its storage in a gas bag for offline analysis.

3.5.1 Experimental Procedure

a) Fluidized Bed Hydrodynamics

Silica sand, of known size and mass corresponding to an aspect ratio (H/D) of 2 or 1, was introduced from the top of the system into the fluidized bed section. Initially, the bed and air heating systems were adjusted to the desired temperature using a PID controller, and then activated for heating.

To initiate fluidization, compressed air from the compressor was introduced into the fluidized bed, gradually increasing the flow rate until the bed materials started to fluidize. The process of fluidization was visually observed through a transparent quartz glass tube. Adequate time was allowed for the bed to reach the desired steady-state temperature, after which the superficial gas velocity was further increased until the bed exhibited vigorous fluidization

After approximately five minutes of operation, the airflow rate entering the gasifier was gradually decreased until the fluidization of the bed ceased. Adequate time was provided for the air and bed materials within the gasifier to reach a specified temperature. During this process, pressure drop values were measured at different superficial velocities. These values of superficial velocities were then plotted against the corresponding pressure drop values, enabling the determination of the minimum fluidization point (U_{mf}). This procedure was repeated using a different set of elevated temperatures, with the same particle size of the bed materials. The obtained U_{mf} value was then utilized to determine the bed height at that specific temperature. Finally, the bed material was emptied from the fluidized bed after the test, and a new particle size was introduced for another set of experiments. To ensure the reliability of the measurements, a minimum of three tests were conducted for each run. The calculated mean error for all the measurements was less than 5 %, indicating a satisfactory level of accuracy.

b) Gasification Process

The bed was heated to an initial temperature of 500 °C before the experiments were conducted, and the air supply was turned on and heated to the desired temperature. In order to keep the residence time constant for all the values of equivalence ratio, a constant air flow rate of 7.6 kg/h, which was 1.5 U_{mf}, was used in all the experiments. In this batch-fed gasifier, a predetermined mass of biomass was fed into the gasifier once the temperature condition of the bed materials was achieved. The quantity of biomass fed corresponded to the mass required for a specific air flow rate to maintain the desired ER. The bed material heating was switched off as the gasification temperature was provided by combustion. After attaining steady state conditions, the heat exchanger and the suction pump were activated and the gas directed to the gas bag for storage.

3.5.2 Gasifier Performance Metrics

Four metrics which included combustible gas species concentration, syngas HHV, gas yield and the tar amount in syngas, were used to assess the gasification performance. These gases are important because they are the primary combustible gas species present in syngas and significantly contribute to the energy density of syngas.

To determine the concentration of various gases, syngas was sampled from the gas storage bag and taken for offline gas analysis using GC-2014 Shimadzu gas chromatograph (F. I. Njuguna et al., 2023). A gas sample was drawn from the gas bag and injected to the gas chromatograph which was calibrated with the instrument grade gases for characterization. The composition of the sampled gas was reported in percentages. The gas components which were considered for analysis included hydrogen (H_2), carbon dioxide (CO_2), carbon monoxide (CO) and methane (CH_4).

The higher heating value is a key metric for assessing the energy content and quality of the produced syngas. It represents the amount of energy released during the complete combustion of a unit quantity of the fuel or gas and considers the heat of vaporization. A higher HHV indicates a more energy-rich gas, which is desirable for efficient utilization in power generation, heating, or other applications (Ngamchompoo and Triratanasirichai, 2017). Higher heating value was obtained from Equation (3.45) (Liu et al., 2018).

$$HHV_{syngas} = \sum_{i=1}^{i} \quad X_i \times HHV_i \qquad 3.45$$

where X_i is the molar concentrations of CO, H_2 and CH_4 and HHV_i is the higher heating value of gas species, shown in Table 3.14 (Ngamchompoo and Triratanasirichai, 2017). The concentrations of the individual gases ware obtained from the experiments and simulation conducted in this study.

Table 3.14: HHV of Various Gas Species

Gas	HHV (MJ/Nm3)
Carbon monoxide	13.1
Hydrogen	13.2
Methane	41.2

Source: (Ngamchompoo & Triratanasirichai, 2017)

Gas yield, which refers to the total volume of gas produced per unit of feedstock during gasification, provides an important measure of overall process efficiency. A higher gas yield indicates a more efficient conversion of the feedstock into gaseous product. Gas yield was computed using Equation (3.46) (Jayathilake and Rudra, 2017). The nitrogen content of biomass was ignored while calculating the gas yield. Only the nitrogen content of air and producer gas was considered during mass balance (D. Singh et al., 2019).

$$y = \frac{Q \times 79\,\%}{m_f \times N_2\%} \qquad 3.46$$

Where Q, mf, and N_2 are air volumetric flow rate, biomass flow rate, and nitrogen concentration in syngas, respectively. These values were obtained from the experiments and simulations performed in this study.

Finally, tar content was another critical metric used to evaluate gasification performance in this study. Tars are complex organic compounds produced during biomass gasification and can cause issues such as equipment fouling, corrosion, and reduced gas quality (Liu et al., 2018).

3.5.3 Tar Measurements

Tar was measured using cold trapping method. This method is a standard of the European tar protocol outlined in the Neeft J.P.A 2005 (Naryanto et al., 2020; Ngamchompoo and Triratanasirichai, 2017), and is shown in Figure 3.16. It involves the utilization of six gas wash bottles and an isopropanol (IPA) solution, which acts as a trapping medium for the tar components. The IPA solution helped to condense and collect the tar from the gas stream. Three bottles (1, 2, 4) were placed in a hot water bath at 35 °C and the other three (3, 5, 6) in an ice-water-salt bath which achieved a temperature of close to -20 °C. Bottles 1-5 were filled with 50 mL of IPA solution (99 % concentration) while bottle 6 was left empty as a drop collector. Bottle 1 absorbed moisture, the hot bath removed heat from cooling and condensation, and the remaining bottles captured tar. A small adjustable speed gas sampling suction pump was used to induce syngas through the sampling unit. It was adjusted to achieve a gas flow rate of 5 L/min using 10 L/Min capacity LZQ rotameter with ±4 % accuracy. After 30 minutes of sampling, the bottles and tubing were rinsed with IPA to make a homogeneous solution in a flask. Gravimetric tar analysis was used to characterize tar by transferring the tar-IPA mixture to an oven at 105 °C for one hour to evaporate IPA, then weighing the residual using OHAUS digital scale with a sensitivity of 0.01 g and an accuracy of 1 %.

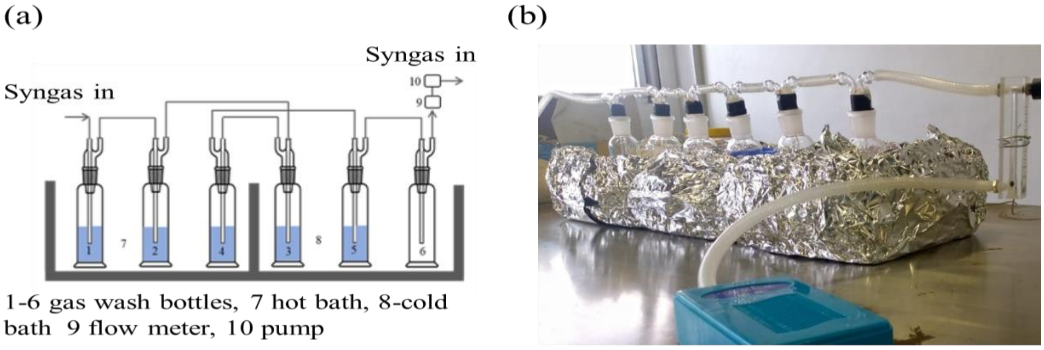

Figure 3.16: Tar Cold Trapping Method (a) Schematic Diagram (b) Experimental Setup

3.5.4 Screening Experiments

Bubbling fluidized bed gasifiers are operated above the minimum fluidization velocity. Operating bubbling fluidized bed gasifiers above the minimum fluidization velocity enhances gasification efficiency by promoting better mixing, but excessive velocity risks bed entrainment, reduced residence time, and fouling of equipment. Therefore, the selected velocity must be sufficient to prevent the entrainment of the bed material and the biomass particles (Ngamchompoo and Triratanasirichai, 2017).

Before conducting the experiments, a preliminary investigation was conducted to evaluate the potential entrainment of the sand and biomass particles. Assessment of the impact of the fluidization velocity factor (λ), which is the ratio of the superficial air velocity to the minimum fluidization velocity, on bed material entrainment involved measuring the mass of the solid particles retained in the cyclone separator.

Initially, 3.44 kg of sand (equivalence of H/D=2) was thoroughly mixed with an equal amount of biomass. The mixture was then poured into the fluidized bed, and the airflow was activated. Air flow rates ranging from 5.1 to 12.6 kg/h were tested for a period of 10 minutes, representing a fluidization velocity factor range of 1 to 3.0. To ensure repeatability, the measurement procedure was repeated at least three times for averaging. Figure 3.17 illustrates the mass carryover as a function of fluidization velocity factor. It can be observed from this figure that there was no material carry over for the fluidization velocity factor values between 1 and 2. These values were, therefore, considered for further analysis. More information if found in Appendix III.

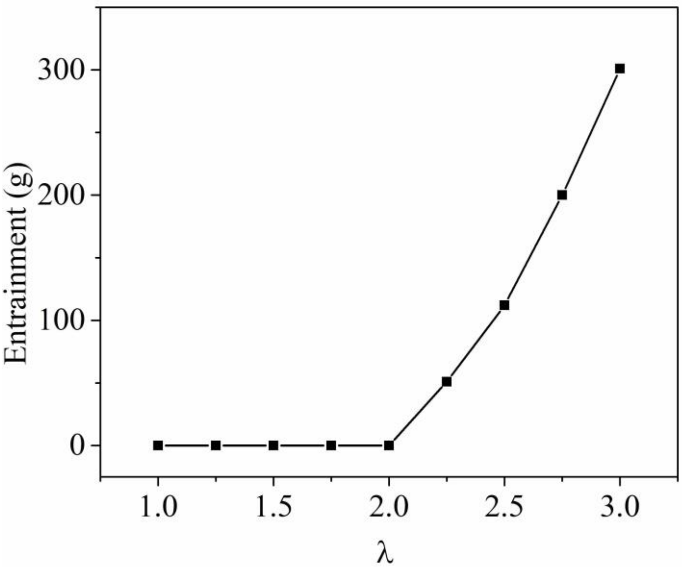

Figure 3.17: Bed Material Entrainment

The equivalence ratio is a significant input variable in gasifiers. It can be adjusted by varying either the air flow rate or the biomass throughput. In this study, it was essential to maintain a consistent flow rate throughout the entire range of equivalence ratios considered. This ensured that the fluidized bed remained within a bubbling state and maintained a uniform residence time for the fuel particles. A consistent residence time formed the basis for comparison of the gasification results at different equivalence ratios. The effect of flow rates, ranging from fluidization velocity factor values of 1.25 to 2 on the gasification performance in terms of gas concentration was investigated and the results are presented in Figure 3.18.

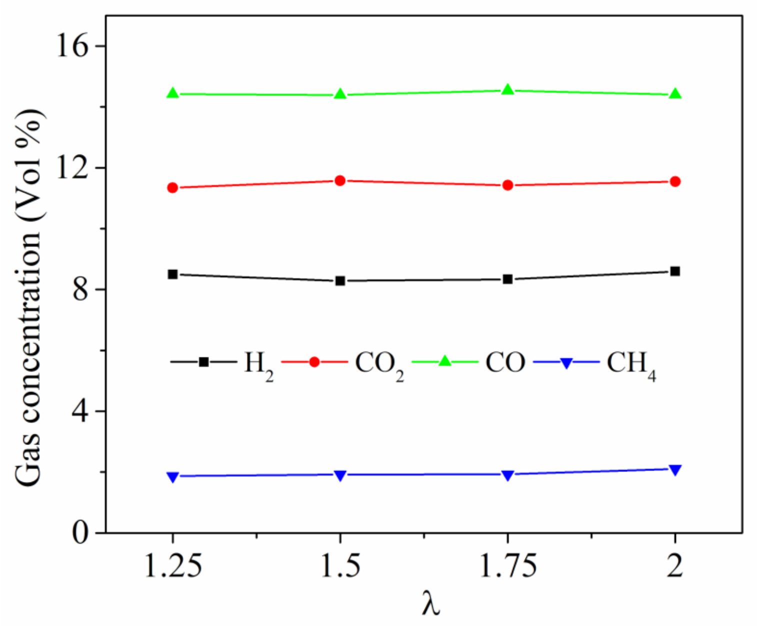

Figure 3.18: Effect of Fluidization Velocity Factor on Gas Concentrations

From this figure, it was clear that there was no significant difference in gas concentration for different values of λ. This was because, although different air flow rates were used, the equivalence ratio was maintained constant by varying the biomass throughput. The equivalence ratio is the major contributor to the syngas production and the fluidization process only facilitates the heat transfer between the biomass particles and the hot bed materials (Vogtenhuber et al., 2019). This explains why there was insignificant change in gaseous concentration for different values of λ. From the foregoing analysis, a value of λ=1.5 was selected for the subsequent gasification studies. A higher fluidization factor was also important to accommodate any potential effects on fluidization resulting from the introduction of biomass waste

3.6 Uncertainty Analysis

In order to ensure accurate and reliable experimental measurements, it was essential to analyze the uncertainty associated with the measured results. Measurement uncertainty refers to the variability observed in the values of a measurement, typically associated with the measurand. It represents the extent to which the measured values may deviate or scatter, providing an indication of the range within which the true value of the measurand is likely to lie (Vehkalahti, 2010).

Measurement errors can be classified into two distinct categories: systematic errors and random errors. Systematic errors, which arise from disturbances in the measurement system and environmental variations, are inherent and cannot be completely eliminated. They represent limitations of the instruments used and can introduce biases in the measured data. On the other hand, random errors result from the precision limitations of the equipment and potential human errors during the measurement process. To reduce the random errors, multiple measurements were conducted and their averages were taken.

Understanding and quantifying uncertainty in experimental measurements are crucial because it provides a measure of the reliability and accuracy of the obtained results. Accounting for the systematic and random errors ensures comprehensive assessment of the overall uncertainty associated with the measurements, allowing for a better evaluation of the significance and validity of study findings. The total uncertainty of the measured values was determined by employing Equation (3.47), which took into account both random and systematic errors. Similar methodologies have been employed by other researchers in the field (Bonilla et al., 2019; Vogtenhuber et al., 2019). Table 3.15 shows uncertainties that resulted from instrumentation.

$$\sigma_{xi}^2 = B_{xi}^2 + P_{xi}^2 \qquad 3.47$$

where B_{xi} and P_{xi} are systematic and random uncertainties of xi.

Table 3.15: Instruments Relative Uncertainties

Instrument	Parameter	Accuracy	Resolution	Capacity	Uncertainty
Rotameter	Air flow rate	±4 %	0.4 m^3/h	16 m^3/h	±4.72 %
Thermocouples	Temperature	±0.5 %	0.5 °C	1100 °C	±0.5 %
Scale	Biomass sample	±1 %	5 g	30 kg	±1 %
Scale	Tar	±1 %	0.01 g	3 kg	±1 %
Pressure transducer	Pressure drop	±1 %	0.001 psi	15 psi	±1 %

The standard uncertainty of the measured values was calculated using Equation (3.48), while the combined uncertainty, which accounts for situations where the output is influenced by multiple variables, was computed using Equation (3.48). This approach considers the interaction of various factors and their respective uncertainties to determine the overall uncertainty associated with the final output (Vehkalahti, 2010).

$$\sigma_i = \sqrt[2]{\frac{\sum_{i=1}^{N} \left(x_i - \underline{x}\right)^2}{N-1}} \tag{3.48}$$

$$\sigma_R^2 = \sum_{i=1}^{N} \left(\frac{\partial R}{\partial xi}\right)^2 \times \sigma_{xi}^2 \tag{3.49}$$

The partial derivatives of syngas HHV and gas yield were computed from Equations (3.45) and (3.46), respectively. Table 3.16 shows the parameters considered in this study and their respective computed values of uncertainties.

Table 3.16: Uncertainties of the Measured Parameters

Output	Uncertainty (%)
Pressure drop	±3.55
Minimum fluidization velocity	±3.01
Equivalence ratio	±4.75
Hydrogen	±4.36
Carbon dioxide	±2.27
Carbon monoxide	±4.06
Methane	±3.12
HHV	±1.5
Gas yield	±1.76
Tar	±3.44

3.7 Hydrodynamics Numerical Simulations

3.7.1 Governing Equations

The hydrodynamics of the gas phase and solid phase in fluidized beds were modeled using the Euler-Euler approach. In this approach, both phases were considered as interpenetrating continua within the same computational volume, allowing for the conservation of mass, momentum, and energy for each phase simultaneously (Dos Santos et al., 2020). The governing equation for the ith phase is shown below.

The mass conservation equation is presented in Equation (3.50) (Savuto et al., 2019).

$$\frac{\partial}{\partial t}(\rho_i . \varepsilon_i) + \nabla . (\rho_i . \varepsilon_i . v_i) = 0 \tag{3.50}$$

Where i denote the phase (gas and solid, i.e., i=g, s). Volume fractions of gas (g) and solid (s) phases are related as shown in Equation (3.51).

$$\varepsilon_s + \varepsilon_g = 1 \qquad 3.51$$

The momentum conservation Equation (3.52) for the ith phase included the momentum transfer terms between the phases.

$$\frac{\partial}{\partial t}(\varepsilon_i.\rho_i.v_i) + \nabla.\left(\varepsilon_i.\rho_i.v_g v_s\right) = -\varepsilon_i.\nabla p + k_{gs}.\left(\overrightarrow{v_g} - \overrightarrow{v_s}\right) + \nabla.\underline{\tau_i} + \varepsilon_i.\rho_i.g \qquad 3.52$$

The viscous stress tensor for the phase, $\underline{\tau_i}$, were given by;

$$\underline{\tau_g} = \varepsilon_g\mu_g\left[\nabla.v_g) + \left(\nabla.v_g\right)^T\right] - \frac{2}{3}\varepsilon_g\mu_g(\nabla.v_g)\bar{I} \qquad 3.53$$

$$\underline{\tau_s} = \varepsilon_s\mu_s\left[\nabla.v_s + \left(\nabla.v_g\right)^T\right] - \varepsilon_s\left[\lambda_s - \frac{2}{3}\mu_s\right](\nabla.v_s)\bar{I} \qquad 3.54$$

Where μ_g , $\mu_s, and\ \lambda_s$ are the gas viscosity, solid shear viscosity and solid bulk viscosity.

The energy equation was solved for the ith phase as presented in Equation (3.55).

$$\frac{\partial[\varepsilon_i\rho_i(h_i+k_i)]}{\partial t} + \nabla.\left[\varepsilon_i\rho_i(h_i + k_i)\overrightarrow{v_i}\right] = \varepsilon_i\frac{\partial p}{\partial t} + \nabla.\varepsilon_i\alpha_{eff}\nabla h_i + K_{ht}\nabla T \qquad 3.55$$

The energy balance equation considered the kinetic energy of the ith phase k_i, enthalpy h_i, and the thermal diffusivity α_{eff}.

3.7.2 Kinetic Theory of Granular Flow

The kinetic theory of granular flow is a set of mathematical models for the kinetic and collision regimes and uses the concept of granular temperature as shown in Equation (3.56) (Savuto et al., 2019). The granular temperature represents the energy from collision of random particles at motion and is calculated in Equation (3.57).

$$\frac{3}{2}\left[\frac{\partial}{\partial t}(\varepsilon_s.\rho_s\theta_s) + \nabla.(\varepsilon_s.\rho_s\theta_s\overrightarrow{v_s})\right] = (-\rho_s\bar{I} + \bar{\bar{\tau_s}}) : \nabla.\overrightarrow{v_s} + \nabla.(K_{\theta s}\nabla\theta_s) - \gamma_s + \varphi_{gs} \quad 3.56$$

$$\theta_s = \frac{1}{3}v'^2 \qquad 3.57$$

Where v' is the fluctuating energy of the particle.

$$K_{\theta s} = \frac{15 d_s\rho_s\varepsilon_s\sqrt{\eta\theta_s}}{4(41-33\eta)}\left[1 + \left(\frac{12}{5}\right)\eta^2(4\eta-3)\varepsilon_s g_0 + \frac{16}{15\pi}(41-33\eta)\eta\varepsilon_s g_0\right] \qquad 3.58$$

$$\eta = \frac{(1+e)}{2} \qquad 3.59$$

Where γ_s is the energy produced due to collision between particles while φ_{gs} is the fluctuating energy between the dispersed and the continuous phases, calculated using Equations (3.60) and (3.61), respectively.

$$\gamma_s = 12\,(1 - e_{ss}^2)\frac{\varepsilon_s^2\rho_s g_0}{d_s\sqrt{\pi}}\theta_s^{\frac{3}{2}} \qquad 3.60$$

$$\varphi_{gs} = -3K_{gs}\theta_s \qquad 3.61$$

where g_0 is the radial distribution function, proposed by Sinclair and Jacksons (Savuto et al., 2019), which describes the probability of particle-particle collision, and is calculated from Equation (3.62).

$$g_0 = \left[1 - \left(\frac{\varepsilon_s}{\varepsilon_{s,max}}\right)^{\frac{1}{3}}\right]^{-1} \qquad 3.62$$

In fluidized bed, kinetic energy and the particle-particle interraction causes solid pressure which is directly proportional to solid collisions. The solid pressure is a representation of the tangential force caused by the interaction between particles in the solid phase. Equation (3.63) shows the solid phase pressure proposed by Lun and is generally accepted in the simulation of fluidized bed (Engen, n.d.).

Bulk viscosity of the dispersed phase represents the resistance of the particle to compression and is shown in Equation (3.64). The bulk viscosity model has been employed successfully by other authors Savuto et al. (2019 to simulate fluidized bed systems and was used in the present numerical modeling.

$$P_s = \varepsilon_s . \rho_s \theta_s + 2\rho_s (1 + e_{ss}) \varepsilon_s^2 g_0 \theta_s \qquad 3.63$$

$$\lambda_s = \frac{4}{3} \varepsilon_s . \rho_s^2 d_s g_0 \left(\frac{\theta_s}{\pi}\right)^{1/2} \qquad 3.64$$

3.7.3 Frictional Stress Model

Frictional stress becomes important in fluidized bed systems with high solid volume concentration. In such scenario, the assumption of instantaneous collision of solid particles, as in the case of the kinetic theory of granular flow (KTGF), is no longer valid and the frictional stress resulting from particle-particle and wall-particle contact should be accounted for. Johnson and Jackson model for solid shear stress accounts for both the kinetic theory and the frictional contributions as shown in Equation (3.65) (Rong et al., 2020a). The additional component is implemented when ε_s is greater than the specified minimum value.

$$\tau_s = \tau_{s,kt} + \tau_{s,f} \qquad 3.65$$

Where;

$$\tau_{s,f} = P_{s,f} I - \mu_{s,f} [\nabla v_s + (\nabla v_s)^T] \qquad 3.66$$

A semi-empirical correlation for the tangential frictional stress, $P_{s,f}$, is calculated in Equation (3.67) $\mu_{s,f}$ is the frictional viscosity.

$$P_{s,f} = F \ \frac{(\varepsilon_s - \varepsilon_{s,f,min})^r}{(\varepsilon_{s,f,max} - \varepsilon_s)^s} \qquad 3.67$$

F, r and s are empirical constants which are material dependent. $\varepsilon_{s,f,max}$ and $\varepsilon_{s,f,min}$ are the maximum and the minimum solid packing. The frictional viscosity and pressure are related as shown in Equation (3.68). The Johnson and Jackson frictional stress model has been used successfully in other studies (Rong et al., 2020b) and was applied in the current work to account for the particle frictional effects.

$$\mu_{s,f} = P_{s,f}\, sin\, sin\, \phi_{\, f} \tag{3.68}$$

Where ϕ_f is the internal frictional angle. This equation is valid for the friction between the particle and the wall by substituting ϕ_f with the wall frictional angle ϕ_w.

3.7.4 Drag Model

The drag force is represented by the product of the momentum exchange between the solid and the gas phases, kg_s, and the slip velocity, $\left(\overrightarrow{v_g} - \overrightarrow{v_s}\right)$ (Marchelli et al., 2020). Gidaspow model is a widely used drag model for gas-solid multiphase flow and is reported to predict dense fluidized bed hydrodynamic with high accuracy (Marchelli et al., 2020; Ngo et al., 2021). It also covers the whole range of void fraction from 0 to 1 by combining both the Ergun and Wen & Yu models shown in Equations (3.69) and (3.70), respectively. Ergun correlation is employed for the bed voidage of less than 0.8, while Wen & Yu correlation is for bed voidage greater than 0.8.

$$K_{gsErgun} = 150\, \frac{\varepsilon_s^2 \mu_g}{\varepsilon_g^2 d_s^2} + 1.75\, \frac{\varepsilon_s \rho_g \left|\overrightarrow{v_g} - \overrightarrow{v_s}\right|}{\varepsilon_g d_s} \qquad \text{for } \varepsilon_g \leq 0.8 \tag{3.69}$$

$$K_{gsWen-Yu} = \frac{3}{4} C_D\, \frac{\varepsilon_g \varepsilon_s \rho_g \left|\overrightarrow{v_g} - \overrightarrow{v_s}\right|}{d_p}\, \varepsilon_g^{-2.65} \qquad \text{for } \varepsilon_g \geq 0.8 \tag{3.70}$$

where;

$$C_{DWen-Yu} = \frac{24}{Re_s}\left(1 + 0.15 Re_s^{0.687}\right) \qquad \text{for } Re_s \leq 1000 \tag{3.71}$$

$$C_{DWen-Yu} = 0.44 \qquad \text{for } Re_s \geq 1000 \tag{3.72}$$

$$Re_s = \frac{\varepsilon_g \rho_g d_p \left|\overrightarrow{v_s} - \overrightarrow{v_g}\right|}{\mu_g} \tag{3.73}$$

3.7.5 Turbulence Model

The RNG k–ℰ turbulence model was employed in the current numerical study for the solid phase. RNG k–ℰ turbulence model has been reported to produce good results that compares well with experimental results for bubbling fluidized beds. Additionally, the

RNG k–$\mathcal{E}$ turbulence model does not require high computational resources and was therefore used in this study (Bhusare et al., 2017).

Conservation equations for the dispersed phase are based on the Kinetic theory of granular flow (KTGF), which is a widely used concept for calculating the dispersed phase properties (Rong et al., 2020b). The sub models used in KTGF were specified in the *turbulenceProperties.particle* file and are summarized in Table 3.17 shown below.

Table 3.17: KTGF Sub Models

KTGF sub model	Correlation
Kinetic particle pressure	Lun
Radial distribution	Sinclair and Jackson
Frictional viscosity	Johnson and Jackson
Kinetic viscosity	Gidaspow
Frictional particle pressure	Johnson and Jackson

3.7.6 Boundary Conditions and Solution Procedure

The solid particles' velocity was set to zero to prevent them from escaping through the inlet boundary (Gosavi et al., 2018; Ngo et al., 2021). For the gas flow, the inlet boundary condition was modelled as non-uniform, using Equation (3.74), to mimic the non-uniform flow induced by perforated distributor plates. This approach is advantageous over incorporating the perforated plate directly into the model. Perforated plates are complex due to their numerous intricate holes, which would complicate the geometry and introduced convergence issues (Bhusare et al., 2017).

$$\epsilon_g = \frac{\kappa+2}{\kappa}\left(\underline{\epsilon_g} - \epsilon_w\right)(1-\gamma^{\kappa}) + \epsilon_w \qquad 3.74$$

Where k is parameter for steepness and γ is the radial distance.

$$\gamma = \frac{r}{R} \qquad 3.75$$

$$k = 2.188 \times 10^3 Re_g^{-0.598} Fr_g^{0.146} Mo_s^{0.004} \qquad 3.76$$

$$Re_g = D\,V_g(\rho_s - \rho_g)/\mu_s \qquad 3.77$$

$$Fr_g = V_g^2/Dg \tag{3.78}$$

$$Mo_l = g\mu_s^4/(\rho_s - \rho_g)\sigma_s^3 \tag{3.79}$$

The inlet pressure boundary condition was specified as *fixedFluxPressure*. The pressure gradient within this boundary condition is modified in order to match the flux at the *boundaryspecified* by the velocity boundary condition. The outlet boundary was assigned a *fixedValue* pressure condition where the value was specifically defined as the atmospheric pressure. The air velocity at the outlet was defined as *pressureInletOutletVelocity*, which calculates the velocity from the difference between the total and static pressure.

The gas phase at the wall was subjected to a no-slip boundary condition, implying no relative velocity between the gas and the wall. On the other hand, for the solid phase, a slip wall boundary condition based on the Johnson and Jackson model, shown in Equation (3.80), was implemented to account for the effect of particle-wall collisions. This slip wall condition takes into consideration the slip velocity and tangential momentum accommodation coefficient, allowing for a more accurate representation of the wall-particle interactions (Koerich et al., 2020).

$$v_{s,w} = -\frac{6\mu_s\varepsilon_{s,max}}{\sqrt{3}\pi\Phi\rho_s\varepsilon_s g_0\sqrt{\theta}}\frac{\partial v_s}{\partial n} \tag{3.80}$$

In this simulation, a specularity coefficient (Φ) value of 0.1 was selected because lower values of Φ tend to provide more accurate predictions of the behavior observed in gas-solid systems. By using a lower Φ value, the simulation takes into account a higher degree of momentum transfer at the solid wall, which is a reflection of the behavior of gas-solid interactions (Eslami Afrooz et al., 2016). Moreover, the Johnson and Jackson particle frictional stress model was employed to incorporate the influence of friction resulting from particle-particle collisions, particularly at low velocities. This is particularly relevant when dealing with scenarios involving slow-moving particles where inter-particle friction becomes significant. The Johnson and Jackson particle frictional stress model helps to accurately capture and account for this frictional behavior, enhancing the accuracy of the simulation results.

The air viscosity, which was influenced by temperature, was determined by utilizing the Sutherland Law as indicated in Equation (3.81) (Gosavi et al., 2018).

$$\mu_T = \frac{A_S\sqrt{T}}{1+T_S/T} \qquad 3.81$$

where A_s is the Sutherland coefficient and T_s is the Sutherland temperature

$$A_s = 1.458 \times 10^{-6} \; and \; T_s = 110.4 \qquad 3.82$$

3.7.7 Numerical Discretization Schemes

Discretization schemes are used to discretize various terms of the governing equations. Discretization enables the convertion of the continuous domain into a discrete grid and allows solving the govering equations numerically. The discretization methods in OpenFOAM are specified in the *fvScheme* dictionary. OpenFOAM provides various numerical schemes. In the current simulation, *ddtSchemes*, *gradscheme* and *divSchemes* were specified.

The term *ddtSchemes*, in OpenFOAM, represents the choice of time scheme. Euler transient scheme was chosen because the simulations are transient in the current numerical investigations. The selected scheme, which is a first order implicit scheme, was a good choice because it is reported to produce fairly accurate results when small timesteps are involved (Bhusare et al., 2017). In the current study, the timesteps specified were very small due to the Courant number restrictions.

The *gradscheme* is the discretization method for the gradient terms in the governing equations. The default Gauss linear scheme was chosen for the current study. Specifying the term default ensured that the Gauss linear scheme was used in all the gradient terms.

The *divSchemes* was used to discretize the convective term in the momentum equation. In the current numerical study, the upwind, first order divergence scheme, was used because of its bounded nature and therefore it is considered accurate appropriate for fluidized bed systems (Bhusare et al., 2017). Table 3.18 shows the summary of the schemes employed in the current simulation study.

Table 3.18: Discretization Schemes

Modeling term	Keyword	Scheme
Time derivative	ddtSchemes	Euler
Gradient term	gradSchemes	default Gauss linear
Convective term	divSchemes	upwind

3.7.8 Convergence Criteria

It was important to ensure that the convergence of numerical solutions was achieved during simulations. A converged numerical solution indicates a physically correct simulation and can be monitored by ensuring convergence of the residuals and continuity errors. Residuals are computed by substituting the current solution for a timestep into the equations and taking the absolute value of the left and right hand side (Holzinger, 2020). They are evaluated before solving an equation, based on the current field values, and re-evaluated after every solver iteration.

The solver employed in the simulation stoped when the residuals fell below the solver tolerance, as specified in the *tolerance* parameter, or the ratio of the current residual to the initial residual fell below the relative tolerance specified in *relTol*. Additionally, the solver terminated if the number of iterations exceeded the maximum number of iterations defined in the *minIter* parameter. Tolerance, r*elTol* and *minIter* were specified in the *fvSolution* dictionary of the OpenFOAM. Absolute tolerances were specified as 10^{-7}, 10^{-6}, and 10^{-5} for the solid concentration, pressure, and bed voidage respectively (Alobaid et al., 2021).

Courant number, C_o, is also controlled in numerical simulations to ensure solution stability and avoid divergence of results. It indicates the fraction of the cell the field flow goes through during a specific time step. Courant number shows if the timestep used in a simulation is small enough for a good time discretization. In the current simulations, a small time-step of 10^{-4} s was specified to ensure the courant number, calculated in Equation (3.83), was less than 0.1 as suggested by Alobaid et al. (Alobaid et al., 2021).

$$C_o = \frac{\Delta t |U_r|}{\Delta x} \qquad 3.83$$

Where ∆t and ∆x is the timestep and cell size respectively.

3.7.9 Simulation Procedure and Post-processing

The *TwoPhaseEuleFoam* solver present in OpenFOAM was used to perform the simulations. This is a solver for two compressible fluids, one continuous (gas) and one dispersed phase (solids). *TwoPhaseEuleFoam* solver uses PIMPLE (PISO-SIMPLE). The PIMPLE algorithm in OpenFOAM is an iterative numerical method designed for solving transient, incompressible flow problems with turbulence modeling. It combines the PISO (Pressure-Implicit Splitting of Operators) algorithm, which handles the pressure-velocity coupling, with the SIMPLE (Semi-Implicit Method for Pressure-Linked Equations) algorithm. The PIMPLE algorithm iteratively solves the segregated equations, alternating between explicit treatment of the turbulence terms and implicit treatment of the pressure-velocity coupling. This iterative approach enhances stability and convergence, gradually improving the solution for both velocity and pressure fields (Bhusare et al., 2017).

Simulations were run for 10 s and then the average values were obtained with results between 5 s and 10 s. Paraview, an open-source visualization application, serves as the primary post-processing tool included with OpenFOAM and was used in this study. Paraview offers a wide range of capabilities for visualizing and analyzing simulation results generated by OpenFOAM.

3.7.10 Case Setup

A schematic, 3-D computational domain, numerical model used in this study is shown in Figure 3.19. Three particle sizes of silica sand were considered as the bed material of the fluidized bed and subjected at temperature ranging between 25 and 400 ^{o}C at various air flow rates. The computational domain was a cylinder of 110 mm and 700 mm internal diameter and height respectively. Three cases were considered as shown in the Table 3.19. All the cases, shown in Table 3.19, were run for ten seconds and the values were averaged between 5 and 10 seconds.

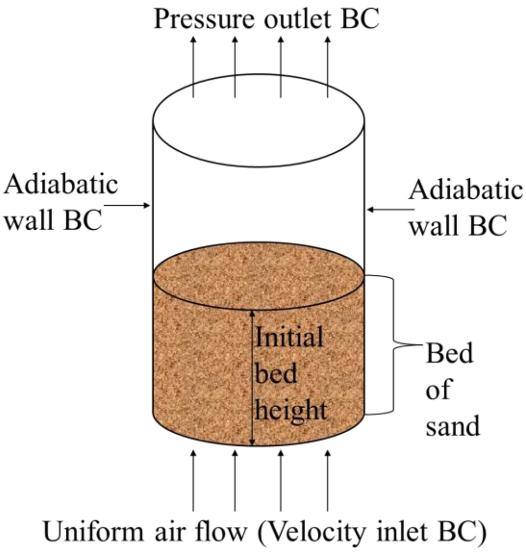

Figure 3.19: 3D Computational Domain

Table 3.19: Simulation Cases

Case	Particle size (μm)	Temperature (ºC)	Superficial velocity (m/s)
1	500	25 - 400	Varied
2	335	25 - 400	Varied
3	233	25 - 400	Varied

3.7.11 Meshing

The 3-D computational domain was modelled in a FreeCAD modeling software and imported to Gmsh software for mesh generation. The mesh was then imported to OpenFOAM to perform simulations using the *gmshToFoam* command. For accurately representing the hydrodynamics of Geldart group B particles, a mesh size 10 to 15 times the particle size is generally recommended. The mesh resolution of this size is considered fine enough to resolve the individual particles and the flow structures around them (Loha et al., 2014). To assess mesh independence, mesh analysis was performed using three different mesh sizes: 15 times the particle diameter (15dp), 10 dp, and 5 dp. Figure 3.20 shows a 3-D computational grid of a mesh size 10 dp generated for 500 μm particle size. A mesh refinement was performed near the walls, as shown in Figure 3.20 (b), to accurately capture the flow behavior in this region.

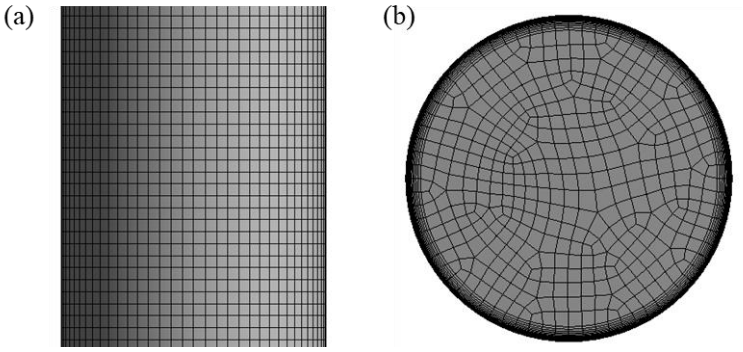

Figure 3.20: 3-D Computational Grid (a) Side View (b) Top View

3.7.12 Mesh Sensitivity Study

Prior to running the simulation, an examination of grid independence was conducted to assess its impact on the simulation results. Three different mesh sizes, fine, medium, and coarse were investigated for four significant fluidization parameters: pressure along the bed height, bed height, bubble growth, and time-averaged bed voidage (Al-Akaishi et al., 2017). Figure 3.21 shows the plots of mesh sensitivity study for pressure along the height of the fluidized bed and averaged bed voidage across the bed.

From Figure 3.21 (a), it can be observed that mesh sizes of 5 and 10 dp yielded comparable pressure drop values along the bed height. However, when a mesh size of 15 dp was employed, the results deviated by an average of 6 %. Regarding the bed porosity, as shown in Figure 3.21 (b), the mesh size of 15 dp exhibited a noticeable deviation from the bed porosity predicted by the mesh sizes of 5 and 10 dp, particularly at the center of the simulation domain.

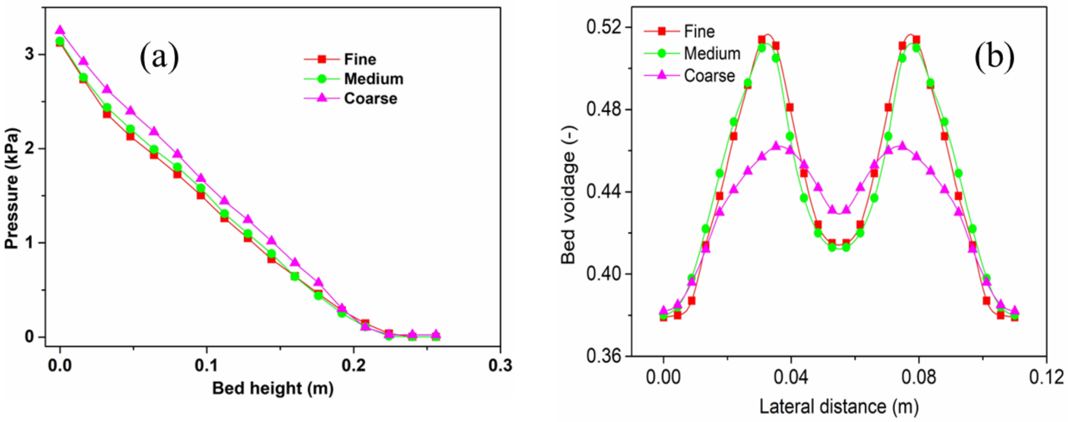

Figure 3.21: Mesh Sensitivity Study for dp =500 μm (a) pressure (b) bed voidage

Figure 3.22 shows the void fraction contours of sand particles, after 10 seconds, at air velocity of 0.25 m/s which was beyond U_{mf}. It can be seen from the figure that the mesh size of 15 dp did not capture the bubble growth appropriately. However, from figure (b) and (c), the mesh size of 10 dp and 5 dp performed relatively well with distinct bubble boundaries indicating that the fluidization phenomenon was captured well. The figures also show small bubbles at the lower part of the bed which became bigger as they moved to the upper part of the bed. In fluidized beds, small bubbles are formed at the bottom of the bed and coalesce and grow in size as they move towards the top of the bed (Eslami Afrooz et al., 2016).

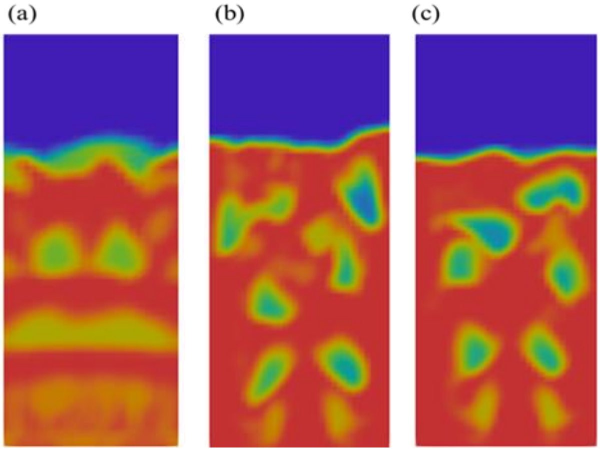

Figure 3.22: Instantaneous Contours of the Sand Volume Fraction

(a) Coarse (b) Medium (c) Fine

Additionally, the bed voidage along the height of the fluidized bed column was further compared as shown in Figure 3.23. The results indicated a close correlation between the bed voidage predicted by the fine and medium meshes across the entire column height. However, the coarse mesh exhibited a notably different bed voidage, particularly in the upper region of the fluidized bed.

Based on the foregoing analysis, the medium mesh size of 10 dp was chosen for this study. The mesh size of 5 dp and 10 dp had comparable performance, but the fine size mesh would require increased computational time without significant improvement of the results.

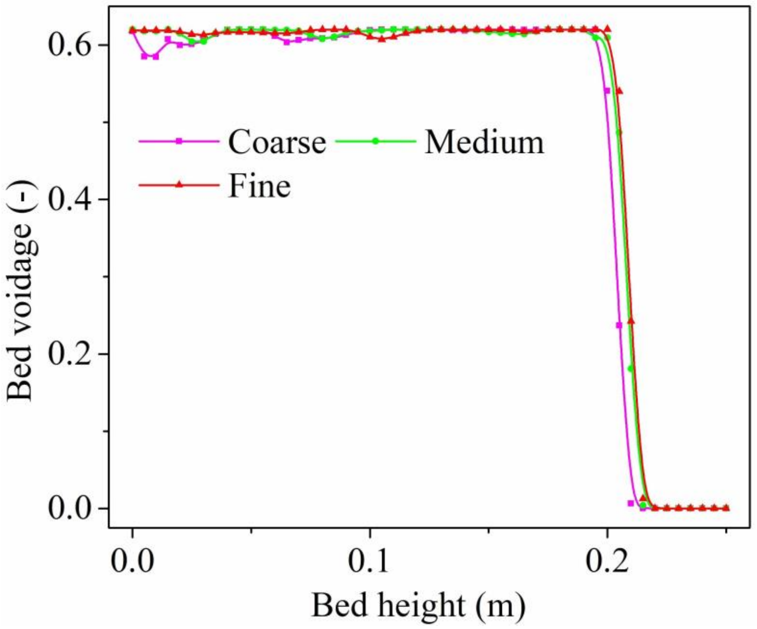

Figure 3.23: Bed Height for Different Mesh Sizes

3.8 Gasification Numerical Simulations

The second part of the numerical study study focused on the development and validation of a numerical model for biomass gasification. The model was designed to incorporate key aspects such as air preheating and included gasification stages such as pyrolysis, combustion, and reduction. Using Aspen Plus, a kinetic modeling approach was employed which incorporated chemical reactions, reaction rates, and correlations for the pyrolysis stage. Furthermore, parametric study of gasification parameters was performed on gasification performance considering combustible gas species concentration, higher heating value, gas yield and tar content in syngas. The purpose of the parametric study was to identify the optimal range of variables that would lead to desirable gasification outcomes. Subsequently, response surface methodology was applied for numerical optimization to maximize the performance of the gasifier.

3.8.1 Simulation Method

The kinetic modeling in the Aspen Plus platform was used to perform numerical investigation in the current study. Kinetic modeling approach considers reactors configuration details, reduction and oxidation reactions and their rates. Aspen Plus offers the flexibility to specify various blocks within the software for specific purposes, including heating, separation, reactions, and mixing. These blocks can be interconnected on a flow sheet, allowing for the construction of complex process models. Reactions blocks are designed to simulate chemical reactions, where users can define reaction kinetics, stoichiometry, and reaction mechanisms, while mixing blocks combines multiple streams, enabling the representation of blending processes.

Aspen Plus employs a sequential modular approach to calculate the outlet stream properties at each stage, relying on the characteristics of the inlet stream. Convergence is established at each stage, and it is possible to integrate Excel subroutines into the flow sheet to calculate the yield (Abdelouahed et al., 2012).

3.8.2 Gasification Process

Three main processes were considered to model the gasification process i.e., pyrolysis, oxidation and reduction processes as shown in Figure 3.24, with intermediate stages such as biochar decomposition, air preheating and ash separation via cyclone separator. Pyrolytic products were computed using the correlations shown in in Table 3.20 (Neves et al., 2011).

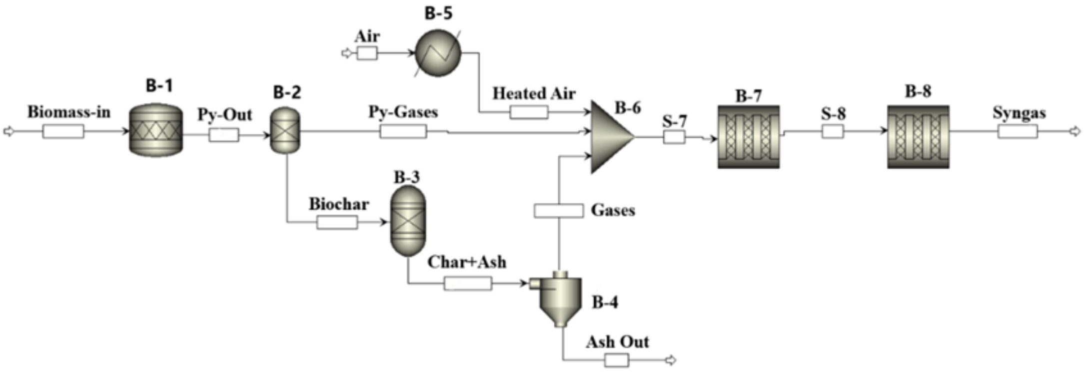

Figure 3.24: Gasification Process: Aspen Plus Flowsheet

Biomass was introduced as an unconventional feedstock into a pyrolizer block, designated as B-1, which facilitated the conversion of biomass into various products, as outlined in Table 3.20. The pyrolysis process resulted in the formation of biochar and gaseous compounds, which were subsequently, separated using a separator block B-2. The biochar underwent decomposition in a decomposer block, referred to as B-3, leading to the generation of ash and gases. The gaseous components were then directed to a mixture block, denoted as B-6, while the ash was separated from the gas using a cyclone separator. Air was introduced to the mixture, and there was an option to heat the air as desired using a heater B-5. The mixture blended the three streams into a homogeneous mixture, which was subsequently directed to an oxidizer block B-7. In this block, the oxidation reactions and their corresponding rates, specified in Table 3.21, were considered. The products resulting from the oxidation reactions were subsequently directed to a reducer block B-8, for the reduction process. The reduction reactions and their corresponding rates were defined within this block, and the final product obtained from this process was syngas.

In Aspen Plus, various models and correlations are employed for computing material properties such as density and enthalpy. PROXINAL and ULTINAL models are utilized for approximating properties of unconventional materials such as biomass and tar. The HCOALGEN model is used to compute the heat of combustion using biomass characterization data, while biomass density is calculated using the DCOALIGT model (Haydary, 2019). For gases and liquids, the Peng-Robinson equation of state was selected to calculate their thermodynamic properties. This equation of state is known for its accuracy over a wide range of gasification temperatures and pressures (Puig-Gamero et al., 2021).

The oxidation and reduction chemical equations, along with their respective rates, as shown in Table 3.21,were specified in the oxidation and reduction stages, respectively. The reaction rates k_i of the ith phase are computed using Equation (3.84).

$$K_i = A_i T . e\left(\frac{-E_i}{RT}\right) \qquad 3.84$$

Table 3.20: Pyrolysis Product Yields

Gaseous product	Yield
ch	$0.106 + 2.43 \times exp(-0.66 \times 10^{-2} \times T)$
C_{ch}	$0.93 - 0.92 \times exp(-0.42 \times 10^{-2} \times T)$
O_{ch}	$0.07 + 0.85 \times exp(-0.24 \times 10^{-2} \times T)$
H_{ch}	$-0.41 \times 10^{-2} + 0.1 \times exp(-0.42 \times 10^{-2} \times T)$
H_2	$1.362 \times 10^{-5}T^2 - 2.517 \times 10^{-2}T + 12.19$
CO	$-3.524 \times 10^{-5}T^2 + 9.77 \times 10^{-2}T - 34.93$
CO_2	$3.958 \times 10^{-5}T^2 - 9.126 \times 10^{-2}T + 64.02$
H_20	$5.157 \times 10^{-5}T^2 - 11.86 \times 10^{-2}T + 78.91$
CH_4	$-4.341 \times 10^{-5}T^2 + 10.12 \times 10^{-2}T - 51.08$
C_2H_4	$-6.873 \times 10^{-5}T^2 + 14.94 \times 10^{-2}T - 76.89$
C_2H_6	$8.265 \times 10^{-6}T^2 - 2.105 \times 10^{-2}T + 13.38$
C_6H_6	$-3.134 \times 10^{-5}T^2 + 7.544 \times 10^{-2}T - 42.72$
C_6H_6O	$1.508 \times 10^{-5}T^2 - 3.662 \times 10^{-2}T + 22.19$
C_7H_8	$-4.539 \times 10^{-6}T^2 + 0.687 \times 10^{-2}T + 1.462$
$C_{10}H_8$	$-8.548 \times 10^{-6}T^2 + 1.882 \times 10^{-2}T - 9.851$

Source: (Neves et al., 2011; Onay et al., 2004)

Where ch is the char; C_{ch} - carbon in char; O_{ch} - oxygen in char; H_{ch} - hydrogen in char.

The kinetic modeling on Aspen Plus utilized in this study was based on the following set of technical assumptions (Pala et al., 2017).

i. Ash was considered inert
ii. The gases were ideal.
iii. The reactor is isothermal.
iv. Pressure in the gasifier was uniform
v. Final syngas characteristics depended on the chemical reactions and their rates.
vi. Tar comprised benzene (C_6H_6), phenol (C_6H_6O), naphthalene ($C_{10}H_8$) and toluene (C_7H_8).
vii. Pyrolysis/devolatilization was instantaneous

Table 3.21: Oxidation, Reduction Reactions and the Kinetic Rates

Reaction No./Name	Reaction	rate (kmol/m^3. s)	Ref.
Oxidation reactions			
R1- C oxidation	$1.25C + O_2 \longrightarrow 0.5CO + 0.75CO_2$	$3.7 \times 10^{10} e^{\frac{-1.5 \times 10^5}{RT}} [O]$	(Choi et al., 2001)
R2 - Methane partial oxidation	$CH_4 + 0.5O_2 \longrightarrow CO + 2H_2$	$1.58 \times 10^{12} e^{\frac{-2.02 \times 10^5}{RT}} [CH_4]^{0.7} [O_2]^{0.8}$	(Puig-Gamero et al., 2021)
R3 - H_2 oxidation	$H_2 + 0.5O_2 \longrightarrow H_2O$	$1.08 \times 10^7 e^{\frac{-1.08 \times 10^4}{RT}} [H_2] [O_2]$	(Gonzalez et al., 2018)
R4 - CO oxidation	$CO + 0.5O_2 \longrightarrow CO_2$	$1.78 \times 10^7 e^{\frac{-1.8 \times 10^5}{RT}} [CO][O_2]^{0.25}[H_2O]^{0.5}$	(Gonzalez et al., 2018)
R5 - Phenol partial oxidation	$C_6H_6O + 4O_2 \longrightarrow 6CO + 3H_2O$	$655 e^{\frac{-8.02 \times 10^4}{RT}} [C_6H_6O]^{0.5}[O_2]$	(Gonzalez et al., 2018)
R6 - Benzene partial oxidation	$C_6H_6 + 4.5O_2 \longrightarrow 6CO + 3H_2O$	$2.4 \times 10^{11} e^{\frac{-1.26 \times 10^{11}}{RT}} [C_6H_6]^{0.5}[O_2]$	(Puig-Gamero et al., 2021)
Reduction reactions			
R7 - Water gas	$C + H_2O \longrightarrow CO + H_2$	$8 \times 10^{-3} e^{\frac{-4.99 \times 10^4}{RT}} [C][H_2O]$	(Gonzalez et al., 2018)
R8 - Boudouard	$C + CO_2 \rightleftarrows 2CO$	$1.05 \times 10^{13} e^{\frac{-1.35 \times 10^5}{RT}} [C]$	(Gonzalez et al., 2018)
R-9 - Methanation	$C + 2H_2 \longrightarrow CH_4$	$1 \times 10^{-4} e^{\frac{-1.0363 \times 10^5}{RT}} [C][H_2O]$	
R10 - Water-gas shift	$CO + H_2O \longrightarrow CO_2 + H_2$	$1.35 \times 10^5 e^{\frac{-102400}{RT}} [CO] [H_2O]$	(Dufour et al., 2008)
R11– CO_2 reduction	$CO_2 + H_2 \longrightarrow CO + H_2O$	$1.2 \times 10^{10} e^{\frac{-318000}{RT}} [CO_2] [H_2]^{0.5}$	(Bustamante et al., 2004)
R12- Methane reformation	$CH_4 + H_2O \longrightarrow CO + 3H_2$	$3.0 \times 10^{13} e^{\frac{-1.25 \times 10^5}{RT}} [CH_4] [H_2O]^{0.5}$	(Gonzalez et al., 2018)
R13 - Phenol reformation	$C_6H_6O + H_20 \longrightarrow 4CO + 0.5C_2H_4 + CH_4 + 3H_2$	$2.4 \times 10^{11} e^{\frac{-1.26 \times 10^{11}}{RT}} [C_6H_6O]$	(Puig-Gamero et al., 2021)
R14 - Thermal cracking of phenol:	$C_6H_6O \longrightarrow CO + 0.4C_{10}H_8 + 0.15C_6H_6 + 0.1CH_4 + 0.75H_2$	$1.0 \times 10^7 e^{\frac{-1.0 \times 10^5}{RT}} [C_6H_6O]$	(Gonzalez et al., 2018)
R15 - Naphthalene Thermal cracking	$C_{10}H_8 \longrightarrow 6.5C + 0.5C_6H_6 + 0.5CH_4 + 1.5H_2$	$1.0 \times 10^7 e^{\frac{-1.0 \times 10^5}{RT}} [C_{10}H_8][H_2]^{0.5}$	(Gonzalez et al., 2018)

3.8.3 Material and Energy Equations

The following mass and energy balance equations are used in Aspen Plus (Haydary, 2019).

Overall mass balance:

$$i = 1NMS_i\sigma_iF_i = 0 \qquad 3.85$$

Sub-stream mass balance for j=1 to NSS:

$$i = 1NMS_iF_if_{ij} = 0 \qquad 3.86$$

Component mass balance for K=1 to NC, j=1 to NSS:

$$i = 1NMS_iF_if_{ij}Z_{ijk} = 0 \qquad 3.87$$

Overall energy balance:

$$i = 1NMS_i\sigma_iF_ih_i + j = 1NHS_j\sigma_jH_j + k = 1NWS_k\sigma_kW_k = RHS \qquad 3.88$$

where S_i is the +1 for inlet streams, -1 for outlet streams; σ_i is the Stream scale factor; F_i is the Mass flow of stream i; f_{ij} is the Mass fraction of sub-stream j in stream i; Z_{ijk} is the Mass fraction of component k in sub-stream j of stream i; NM is the Number of combined inlet and outlet material streams; NH is the Number of combined inlet and outlet heat streams; NW is the Number of combined inlet and outlet work streams; NSS is the Number of sub-streams within material streams; NC is the Number of components specified; hi is the Mass enthalpy of stream i; H_j is the Heat flow of heat stream j; W_k is the of work stream k; RHS is the Right-hand side of the energy balance equation.

The convergence of the simulation model was checked for mass and energy balances around each block as it was executed and at the end of the simulation. The mass and the energy balance was checked with a relative tolerance of 0.0001 (Haydary, 2019).

3.9 Validation of the Numerical Models

The numerical models for the fluidized bed hydrodynamic behavior and the gasification process were validated using experimental data. Quantitative analysis was conducted using the root mean square error (RMSE) and the percentage mean absolute error (%MAE), computed according to Equations (3.89) and (3.90), respectively. This method was used in other studies to validate simulation models (Kombe et al., 2022; Sharma and Nath, 2023).

$$RMSE = \sqrt{\frac{\sum_{i=1}^{N} \quad (Experimen_i - Simulation_i)^2}{N}} \qquad 3.89$$

$$\%MAE = \sum_{i=1}^{N} \quad \frac{|Experiment_i - Simulation_i|}{N} \qquad 3.90$$

where N are the data points in consideration and i is the variable.

3.10 Optimization Technique

The numerical optimization aimed to determine the combination of input variables that would yield the best gasification performance and meet defined optimization objectives. In addition, prediction models were developed and the best operating conditions for atmospheric pressure and pressurized gasifiers were identified.

Figure 3.25, shows the flow chart of the response surface optimization technique that was used for numerical optimization of the gasification process parameters. Box-Behnken design (BBD) response surface methodology was utilized in this study.

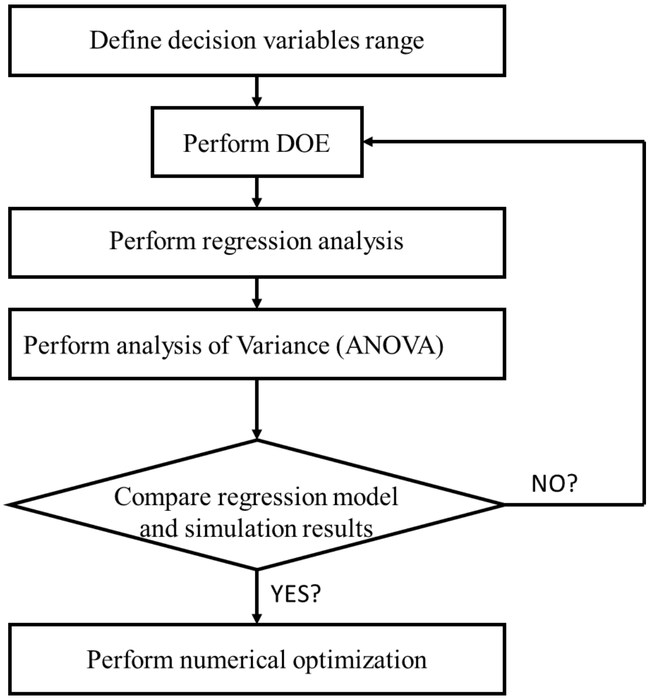

Figure 3.25: Response Surface Methodology Flow Chart

The Box-Behnken design is a widely used method in the field of response surface methodology (RSM) for conducting Design of Experiment (DOE). This technique employs a factorial design, but with fewer runs compared to a full factorial design. BBD achieves this by utilizing a combination of three-level orthogonal arrays, where each factor is examined at three levels: low, medium, and high. The design ensures an adequate representation of the curvature of the response surface, enabling the estimation of response contours and subsequent optimization. In this study, the Box-Behnken design was chosen to determine the number of experimental runs required, as indicated by Equation (3.91) (Parthasarathy and Narayanan, 2014).

$$N = 2 \times k(k-1) + cp \qquad 3.91$$

where cp is the number of central points, k is the number of input variables, and N is the number of runs.

The regression models between the independent variables and the output responses are based on the polynomial quadratic relation shown in Equation (3.92).

$$z = \beta_0 + \sum_{i=1}^{n} \beta_i x_i + \sum_{i=1}^{n} \beta_{ii} x_i^2 + \sum_{i=1}^{n-1} . \sum_{j=1}^{n} \beta_{ij} x_i x_j + \phi \ .... \ 3.92$$

where z is the output response, β_0, β_i, β_{ii}, and β_{ij} are constant, linear, quadratic, and interaction coefficients, respectively, x is decision parameters, n is the number of input variables, and ϕ is a statistical error.

After the regression model was developed, the statistical significance of the regression model was assessed using analysis of variance (ANOVA) and the following criterion (Betiku and Taiwo, 2015; Mostafaei et al., 2016)

i. Residual which is the difference between the observation values, zi and the predicted values $\widehat{zi}$ as shown in Equation (3.93)

$$ei = zi - \widehat{zi} \qquad 3.93$$

ii. Total sum of squares, SS, which was obtained using Equation (3.94).

$$SS_T = \sum_{i=1}^{n} z_i{}^2 - \frac{(\sum_{i=1}^{n} z_i)^2}{n} \qquad 3.94$$

where n is the number of observations.

iii. Sum squares of residuals, SST, which was obtained using Equation (3.95).

$$SS_E = \sum_{i=1}^{n} (z_i - \widehat{zi})^2 \qquad 3.95$$

iv. Coefficient of determination, R^2, which was obtained using Equation (3.96).

$$R^2 = 1 - \frac{SS_E}{SS_T} \qquad 3.96$$

The value of R^2 is usually between 0 and 1; however, a large value of R^2 does not always indicate a good regression model because adding a new variable, whether statistically significant or not, will always increase the value of R^2. For this reason, the adjusted coefficient of determination, R^2_{adj}, estimated using Equation (3.97), is usually preferred (Esfe et al., 2017; Parthasarathy and Narayanan, 2014).

$$R_{adj}^2 = 1 - \left(\frac{SS_E}{(n-p)} / \frac{SS_T}{(n-1)} \right) \qquad 3.97$$

where p is the number of independent variables in a regression model.

3.10.1 Optimization Parameter

When conducting multi-objective optimization for biomass gasification, the selection of equivalence ratio, air preheating temperature, and gasifier pressure was due to their significant impact on the process. The equivalence ratio dictates the balance between oxidation and reduction reactions and influences the syngas composition, yield and combustion temperature. Optimizing this ratio enhances syngas production and reduces tar formation (Mirmoshtaghi et al., 2016; Ngamchompoo and Triratanasirichai, 2017).

Air preheating temperature was chosen because it directly affects reaction kinetics and the energy content of the process. Preheated air accelerates gasification reactions, improving conversion efficiency and syngas quality. Higher preheating temperatures help thermal cracking of heavier hydrocarbons, reducing tar production (Ependi et al., 2019; Ngamchompoo and Triratanasirichai, 2017).

Gasifier pressure was selected for its influence on the thermodynamics and kinetics of gasification reactions. Increased pressure enhances reaction rates and promotes production of syngas with higher hydrogen and carbon monoxide concentrations. Additionally, higher gasifier pressure facilitates integration with other systems operating at elevated pressures and ensures seamless and efficient system performance (Motta et al., 2018).

CHAPTER FOUR

RESULTS AND DISCUSSIONS

This chapter presents results from the experimental measurements and the numerical modeling for the fluidized bed hydrodynamic behavior and the biomass gasification process. The experimental results, which were used for validation, are briefly introduced, followed by numerical modeling results.

4.1 Experimental Measurements

Experimental measurements involved non-reactive and reactive experiments for the fluidized bed hydrodynamic behavior and gasification process respectively.

4.1.1 Minimum Fluidization Point

Fluidized bed hydrodynamic behavior at the minimum fluidization point was used to validate the fluidized bed hydrodynamics numerical model. Initially, non-reactive experiments were carried out to evaluate the impact of bed aspect ratio on minimum fluidization to rule out the effect of initial bed height on the minimum fluidization velocity (U_{mf}). Two different bed aspect ratios, H/D = 2 and H/D=1, were employed, utilizing particles with a size of 500 µm, and temperatures ranging from 25 to 400 ^{o}C.

Figure 4.1 illustrate the relationship between air flow rates and bed pressure drop for sand particles size of 500 μm across a temperature range of 25 °C to 400 °C. The position of the minimum fluidization point is identified by dashed vertical lines, which were utilized to determine the experimental minimum fluidization velocity.

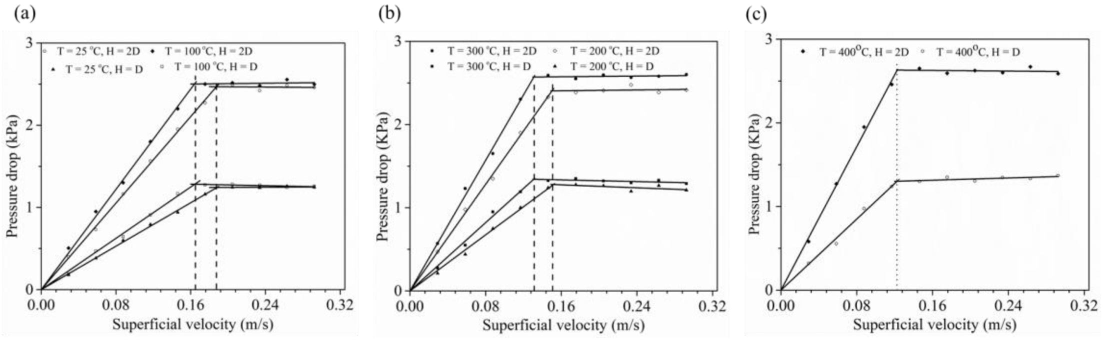

Figure 4.1: U_{mf} for the Particle Size of 500 µm at Temperatures (a) 25 and 100 (b) 200 and 300 (c) 400 °C

From the plots, it was observed that the pressure drop increased linearly as the superficial velocity increased. The linear section indicated the fixed bed regime which can be attributed to the increased drag force exerted by the fluid on the particles, leading to a greater resistance to flow (Shao et al., 2019). However, once the minimum fluidization point was reached, the bed transitioned into a fluidized bed regime, and the pressure drop becomes relatively constant. This behavior can be attributed to the balanced forces acting on the particles, where the upward drag force from the fluid balances the downward gravitational force (Al-Farraji and Taofeeq, 2020).

It can also be observed that changing the initial bed height from H=D to H=2D (twice the bed diameter), doubled the bed pressure drop. This can be attributed to the increased bed materials, leading to more resistance to fluid flow. However, the minimum fluidization point remained unaffected, suggesting that the minimum fluidization point depends on the particle properties rather than the geometry of the column. Escudero and Heindel (2011) reported that the bed pressure drop is normally proportional to the weight of the bed materials.

From Figure 4.1 (a), (b), and (c), the minimum fluidization point decreases with increasing temperature. This can be attributed to the expansion of air and its reduced density at high temperature. Local air velocities increase with the temperature, and thus bed materials at higher temperature requires lower air velocitiy to fluidize.

After establishing that the minimum fluidization point was independent of the bed height, further experiments were conducted using a bed aspect ratio of two (H=2D), for the sand particles sizes of 335 and 233 µm. The observed behavior of the bed remained consistent with the aforementioned findings, as shown in Figure 4.2, where both particle sizes exhibited the fixed bed regime and the fluidized bed regime. It is also observed that the minimum fluidization velocity decreased with inceasing temperature.

It can also be observed from Figure 4.2 that the minimum fluidization point increased witht particle size. For instance, at 25 ^{o}C, the minimum fluidization velocity was 0.125 m/s for the 335 µm particles (Figure 4.2 (a)) and 0.04 m/s for the 233 µm particles (Figure 4.2 (c)). This is because large particles have higher mass and resistance, requiring greater airflow rate to initiate fluidization.

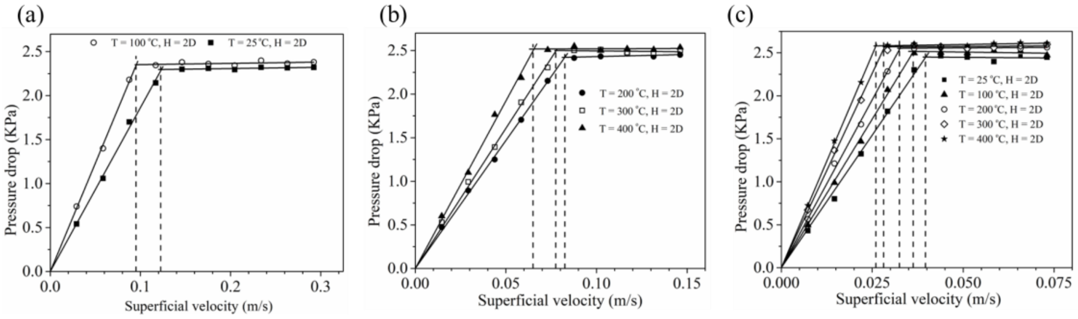

Figure 4.2: Umf for the Particle Sizes of 335 µm (a) & (b) and 233 µm (c)

4.1.2 Gasifier Temperature Profile

Gasifier temperature profile plays a crucial role in analyzing their performance. Figure 4.3 illustrates the variation of gasification temperature along the height of the gasifier. In Figure 4.3 (a)-(f), a peak temperature was observed near the top of the fluidized bed (thermocouple T2), indicating the zone where the oxidation of char and volatiles occurred in the presence of oxygen from the air. The char oxidation reactions, shown in Equations (4.1) and (4.2), are exothermic processes that generate heat to drive the gasification process. Consequently, a temperature increase is observed at the lower part of the gasifier (Bonilla and Gordillo, 2017).

$$C + 0.5O_2 \longrightarrow CO \qquad 4.1$$

$$C + O_2 \longrightarrow CO_2 \qquad 4.2$$

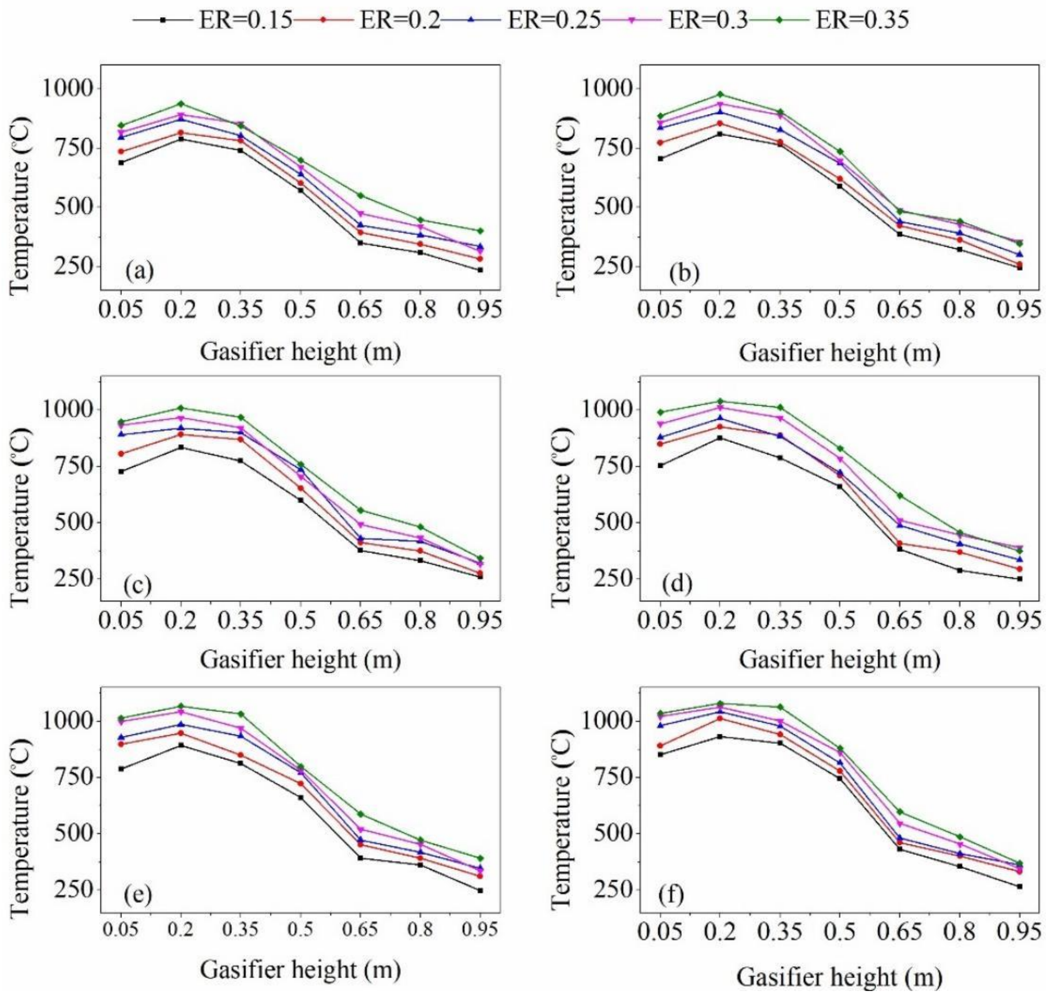

Figure 4.3: Gasifier Temperature Profile at Air Temperature of (a) 25 (b) 125 (c) 225 (d) 325 (e) 425 (f) 525 ºC

It can also be observed from Figure 4.3 (a)-(f) that the gasifier temperature decreased from the fluidized bed section upwards, reaching its lowest point at the top of the gasifier (thermocouple T7). This can be attributed to the depletion of available oxygen in the upper regions of the gasifier. Most of the oxygen is consumed during the oxidation zone, leaving limited oxygen for combustion in the upper section. In addition, biomass fuel undergoes pyrolysis and drying just above the oxidation zone. In this zone, a gaseous mixture comprising H_2, CO, CO_2, CH_4, and H_2O is produced.

At the upper part of the gasifier, CO reacts with steam in the water gas-shift reaction (4.3), resulting in the generation of more hydrogen and carbon dioxide. However, this reaction consumes heat, leading to a further reduction in temperature in the upper part of the gasifier (Bonilla et al., 2019).

$$CO + H_2O \longrightarrow CO_2 + H_2 \tag{4.3}$$

It was further observed that the gasification temperatures increased at different locations as the equivalence ratio (ER) was varied. From Figure 4.3, all thermocouples registered a temperature rise, indicating that changing ER impacted the entire gasifier. For instance, in Figure 4.3 (a) at 25 °C, thermocouple T2 recorded the highest temperature increase, rising from 789 °C to 937 °C when the ER was varied from 0.15 to 0.35. This temperature rise can be attributed to the exothermic char oxidation reactions which are promoted by the increased oxygen at higher ER.

4.1.3 Air Preheating and the Gasifier Temperature

The impact of air preheating on the gasifier temperature is illustrated in

Figure 4.4. (a) and (b).

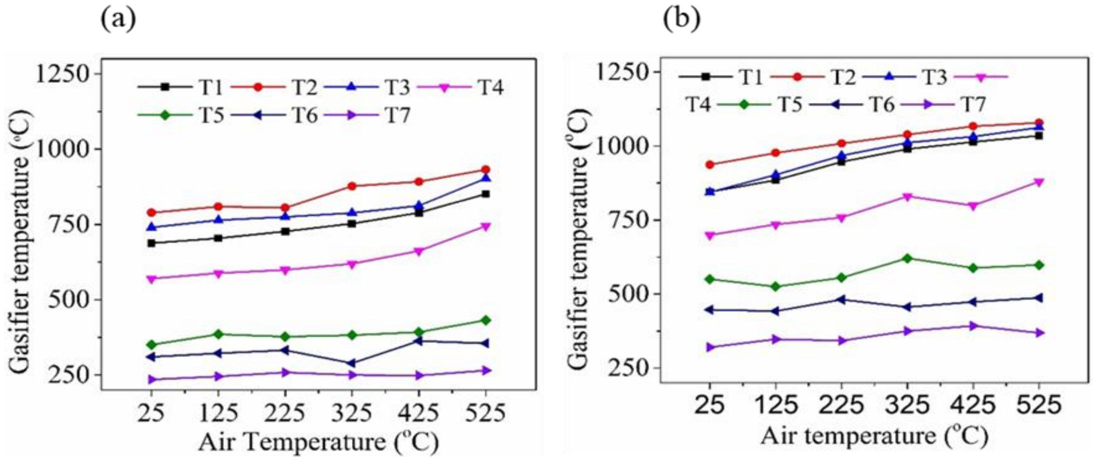

Figure 4.4: Effect of Air Preheating on Gasifier Temperature (a) ER= 0.15 (b) ER= 0.35

From this figure, air preheating had a more pronounced effect in the lower section of the gasifier, with diminishing influence towards the upper regions. In Figure 4.4 (a), heating air from 25 to 525 °C led to a 19 % increase in the highest temperature (T2), while the temperature at the upper part of the gasifier (T7) only rose by 8 %. This indicates that the majority of the sensible heat energy from the preheated air was consumed at the lower part of the gasifier. However, as reported by other researchers, the increase in temperature affects the overall performance of the gasifier, leading to improved syngas higher heating value and reduced amount of tar (Abdoulmoumine et al., 2014; Doherty et al., 2009).

Air preheating offers significant advantages, particularly when utilizing waste heat generated from other industrial processes (K. T. Wu and Chein, 2015). It is clear from Figure 4.4 that using low equivalence ratio (ER) and air preheating can be achieve the desired gasification temperature without relying entirely on high ER. Higher ER tends to reduce the higher heating value (HHV) of the syngas by reducing concentrations of carbon monoxide, hydrogen and methane which contributes to syngas HHV (Abdoulmoumine et al., 2014). For example, in Figure 4.4 (b), a peak temperature of 937 °C was attained by employing an ER of 0.35 and gasifying air at room temperature. On the other hand, Figure 4.4 (a) shows that a peak temperature of 932 °C was attained using a low ER of 0.15 and air at 525 °C. This suggests that the combination of a lower ER and air preheating can serve as an alternative to a higher ER with air at the room temperature. With this combination, the gasification equipment can be designed to be more compact as less amount of air is required to reach the desired operating temperature, facilitating a more efficient and compact gasifier design.

4.2 Validation of the Numerical Models

The fluidized bed hydrodynamics and gasification numerical models were validated by comparing the simulation results and the experimental results from the current study and those found in existing literature. Subsequently, other results derived from predictions of other conditions obtained using the validated models are presented.

4.2.1 Fluidized Bed Hydrodynamics Numerical Model

a) Minimum Fluidization Velocity (U_{mf})

Figure 4.5 shows the comparison between the experimental measurements and simulations values of the minimum fluidization velocity for the variation of U_{mf} with temperature. It can be observed that the CFD simulation results slightly overestimated U_{mf}, with the U_{mf} values ranging between 0.13–0.2, 0.07–0.12, and 0.025–0.045 m/s for 500, 335 and 233 μm, respectively. Percentage mean absolute error (MAE) and a root mean square error (RMSE) of approximately 6.6 % and 0.007, respectively, were computed, indicating a reasonable agreement with the experimental results.

It was observed that the minimum fluidization velocity decreased as the temperature was increased, which can be attributed to the change of properties of air and bed particles with temperature. At higher temperatures, the internal local air velocities increase due to the expansion of air, resulting in a reduced air velocity requirements for fluidization. Furthermore, the interparticle forces, such as Van der Waals forces, are weakened at high temperatures, leading to reduced agglomeration and easier particle dispersion, thereby affecting the minimum fluidization velocity.

It was further observed from Figure 4.5 that the minimum fluidization velocity (U_{mf}) increased with particle diameter, which is attributed to higher mass and inertia of the bigger particles, requiring a higher air velocity to initiate fluidization. Additionally, the drag force exerted by the air on the particles is influenced by their size. Larger particles experience greater drag forces, necessitating higher air velocities to achieve fluidization.

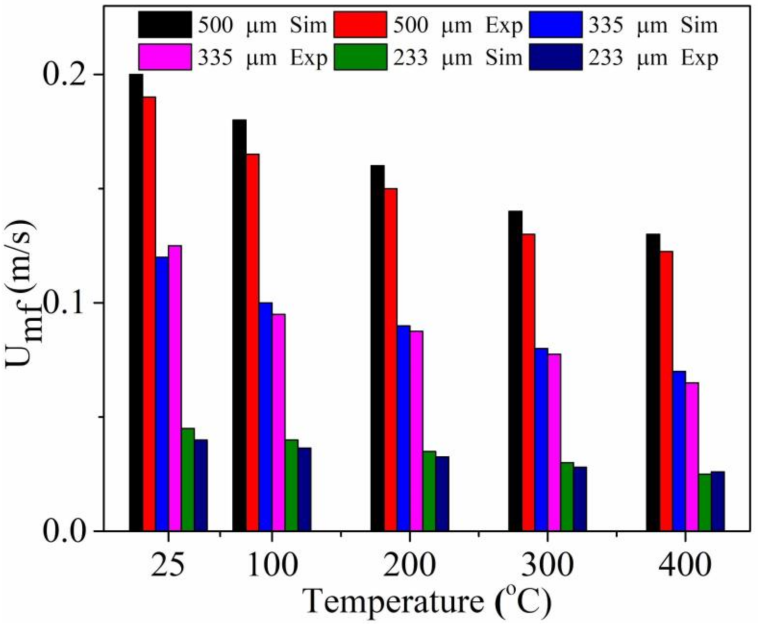

Figure 4.5: Variation of U_{mf} with Temperature: Experimental and Simulation Results

b) Bed Voidage

The effect or temperature on the bed voidage at the minimum fluidization point is shown in Figure 4.6. The simulation values were majorly underestimations although with a good agreement of percentage mean absolute error of approximately 5 % over the range of particle sizes and temperatures considered.

The bed voidage was directly proportional to the temperature of the bed materials. Increasing the temperature from 25 to 400 ^{o}C led to a mean increment of 4.6 and 6.3 % across all the particle sizes for the ε_{mf} values from simulation and experimental results, respectively. This behavior can be attributed to the reduced interparticle forces at higher temperature, leading to reduced resistance to flow and increased particle motion within the bed. Additionally, thermal expansion of the particles at elevated temperature contributes to increased spaces between the particles hence bed voidage.

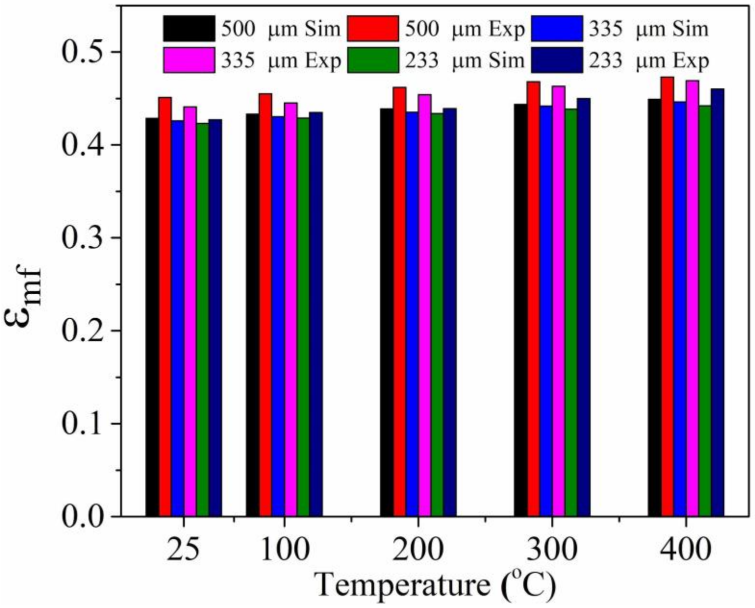

Figure 4.6: Effect of Temperature on ε_{mf}: Experimental and Simulation Results

It was further noted from Figure 4.6 that the bed voidage (ε_{mf}) increased with the particle size, which can be attributed to the loose packing associated with the larger particles, resulting in a higher void fraction. Conversely, smaller particles have better packing characteristics, with more volume concentration and are therefore able to fill the small voids in the bed leading to lower bed voidage.

c) Bed Pressure Drop

The bed pressure drop was examined at various bed temperature and minimum fluidization velocities. The measured values were then compared to the modeling results, as displayed in Figure 4.7. The numerical model predicted the pressure drop with a percentage mean absolute error of 6.6 % and a root mean square error of 0.09 kPa, indicating a good model agreement.

At the pressure drop at the minimum fluidization velocity remained relatively constant with the temperature variations. Pressure drop at the minimum fluidzation point is proprtional to the wight of the bed material which remains fairly constant with the temperature.

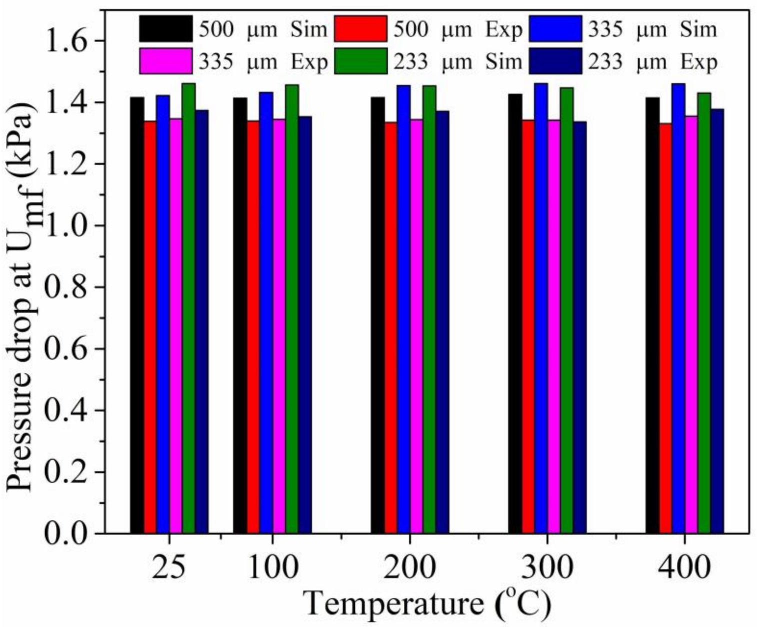

Figure 4.7: Bed Pressure Drop at the Minimum Fluidization Point: Experimental and Simulation Results

4.2.2 Gasification Numerical Model

a) Syngas Composition

The validation of the model involved comparing the experimental results and the simulation results for the effect of equivalence ratio (ER) and air temperature on gas composition as depicted in Figure 4.8 (a) and Figure 4.8 (b) respectively. The range of air temperature and ER was between 25-825 °C and 0.15-0.35, respectively.

On the effect of the equivalence ratio on gas composition, Figure 4.8 (a), the root mean square error was found to be 0.72, indicating a moderate level of deviation. The percentage mean absolute error was found to be 7 %, suggesting a reasonable agreement between the experimental and simulated data. Similarly, the effect of air temperature on gas composition, shown in Figure 4.8 (b), was examined and the RMSE was determined to be 0.59, indicating a slightly small deviation from the experimental results. The mean absolute error was calculated to be 5 %, indicating a good agreement between the experimental and simulated data.

It was further observed that the numerical simulation slightly overestimated the concentrations of hydrogen and carbon dioxide, while underestimating the concentrations of carbon monoxide and methane. This can be attributed to the simplifications and assumptions made in the kinetic model. During the gasification process, the pyrolysis stage generates high amount of methane and other hydrocarbons that may not undergo complete reactions with other gases. As a result, experimental measurements of CH_4 in syngas are usually high (Ren et al., 2022).

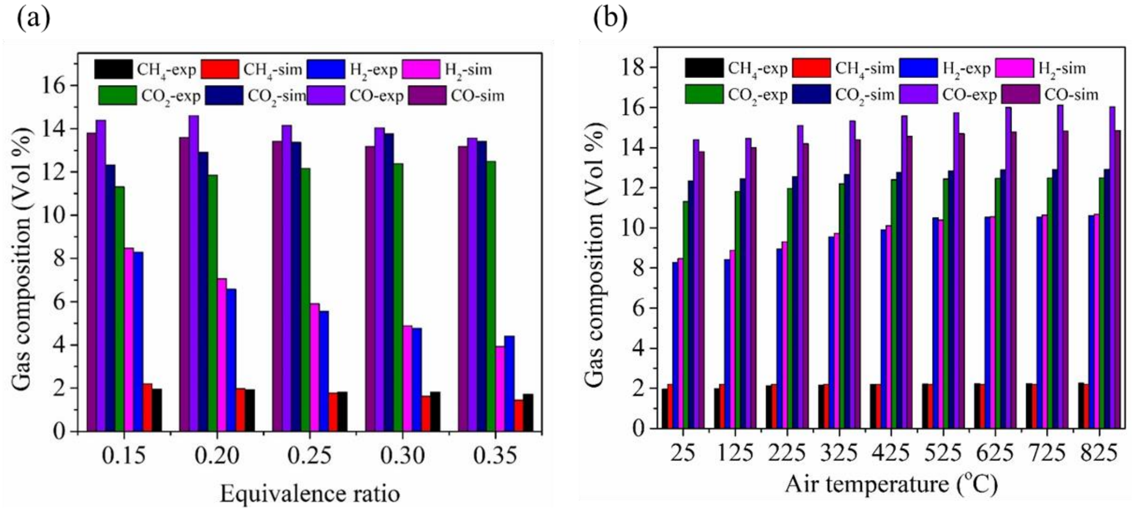

Figure 4.8: Experimental and Simulation Results of Gas Composition (a) Equivalence Ratio (b) Air Temperature

It was also observed that the concentrations of CH_4, CO, and H_2 decreased as the equivalence ratio was increased. This can be attributed to the greater amount of oxygen supply of oxygen at higher equivalence ratio, leading to enhanced oxidation reactions which lower concentrations of combustible gas species. Oxidation of H_2 and CO to H_2O and CO_2 due to the availability of more oxygen led to a decrease in the concentration of H_2 and CO as shown in oxidation reactions (4.4) and (4.5), respectively. Reaction (4.5) further shows that CO_2 concentration increased through CO oxidation.

$$H_2 + 0.5O_2 \rightarrow H_2O \tag{4.4}$$

$$\mathrm{CO} + 0.5\mathrm{O_2} \longrightarrow \mathrm{CO_2} \tag{4.5}$$

On the contrary, the concentrations of CO, H_2, and CH_4 increased when the air temperature was increased. Boudouard reaction ($C + CO_2 \leftrightarrow 2CO$) and water gas shift reactions reaction ($C + H_2O \leftrightarrow CO + H_2$) are favored at high temperature and could have contributed to production of more H_2, CO and CO_2 as the air temperature was increased (Abdoulmoumine et al., 2014).

b) Higher Heating Value

Figure 4.9 shows experimental and simulation results for the effect of equivalence ratio (ER) and air temperature on syngas higher heating value (HHV). From Figure 4.9 (a), a root mean square error of 0.134 and a percentage mean absolute error of 3.8 % were obtained. On the other hand, a root mean square error of 0.123 and a mean absolute error of 3 % were obtained by comparing the results in Figure 4.9 (b). Overall, the results revealed that HHV decreased as the equivalence ratio increased as shown in Figure 4.9 (a). On the other hand, Figure 4.9 (b) shows that increasing air temperatures led to an increase in syngas HHV. It was discussed in Section 4.2.2 (a) that the concentration of CO, CH_4 and H_2 decreases with the equivalence ratio but increases with the air temperature. These gases were utilized to obtain the syngas HHV as indicated in Equation (3.45), and hence its behaviour with ER and air preheating.

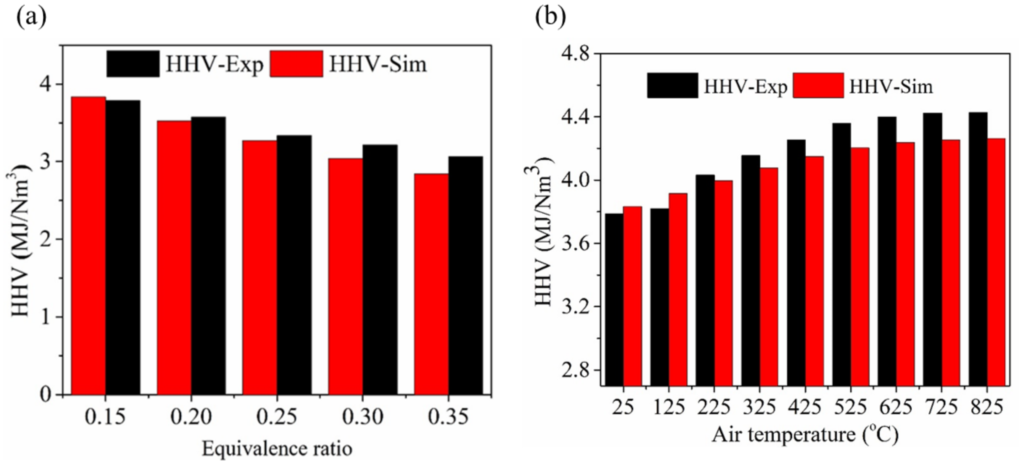

Figure 4.9: Experimental and Simulation Results of Syngas and HHV (a) Equivalence Ratio (b) Air Temperature

c) Gas Yield

Figure 4.10 shows gas yield as a function of the equivalence ratio and air temperature.

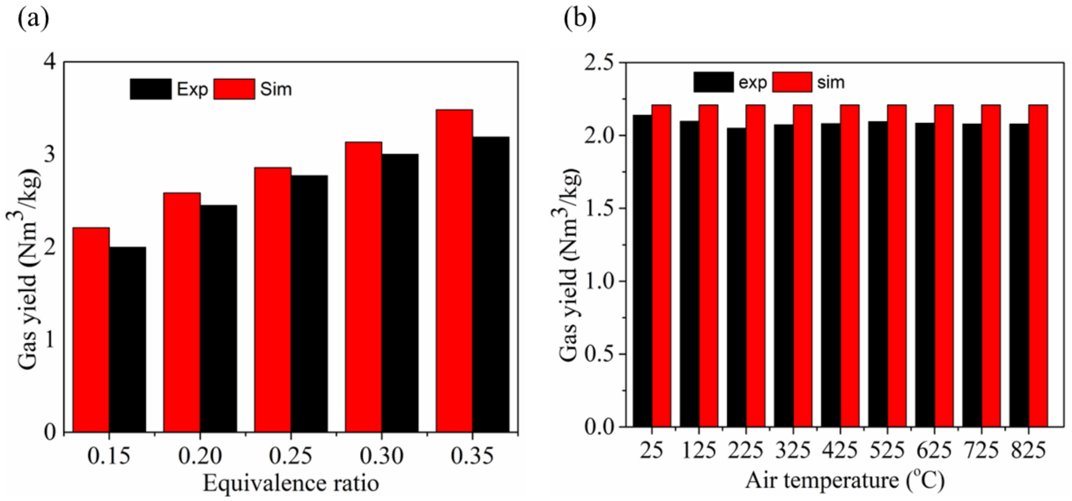

Figure 4.10: Experimental and Simulation Results of Gas Yield (a) Equivalence Ratio (b) Air Temperature

Based on Figure 4.10 (a) results, a root mean square error of 0.165 and a percentage mean absolute error of 5.1 % were obtained. Similarly, a root mean square error of 0.125 and a percentage absolute mean square errors of 5.9 % were obtained Figure 4.10 (b) results. The small errors indicated fairly accurate model, although with slight over-predictions.

It was further observed that the gas yield increased with the equivalence ratio while it remained fairly constant with the air preheating as shown in Figure 4.10 (a) and 9b), respectively. At higher ER, a larger portion of the carbon in the feedstock was converted into gaseous products like carbon monoxide, hydrogen, methane. This resulted in a more complete conversion of the carbonaceous material and subsequent increased gas yield. The gas yield remained fairly constant while varying air preheating. This behavior was expected since the equivalence ratio remained constant during the air preheating process.

d) Tar Content in Syngas

The numerical model was also validated using tar measurement results. From Figure 4.11 (a), on the effect of equivalence ratio on tar content, a root mean square error of 2.14 and a percentage mean absolute error of 7.4 % were obtained, indicating a fairly good numerical model. The results showed that tar content decreased as the ER and air temperature increased. Higher equivalence ratios resulted in a greater amount of oxygen supplied, promoting the thermal cracking of tar into lighter gases. On the other hand, at lower equivalence ratios, pyrolysis predominates, leading incomplete carbon conversion, and high amount of tar.

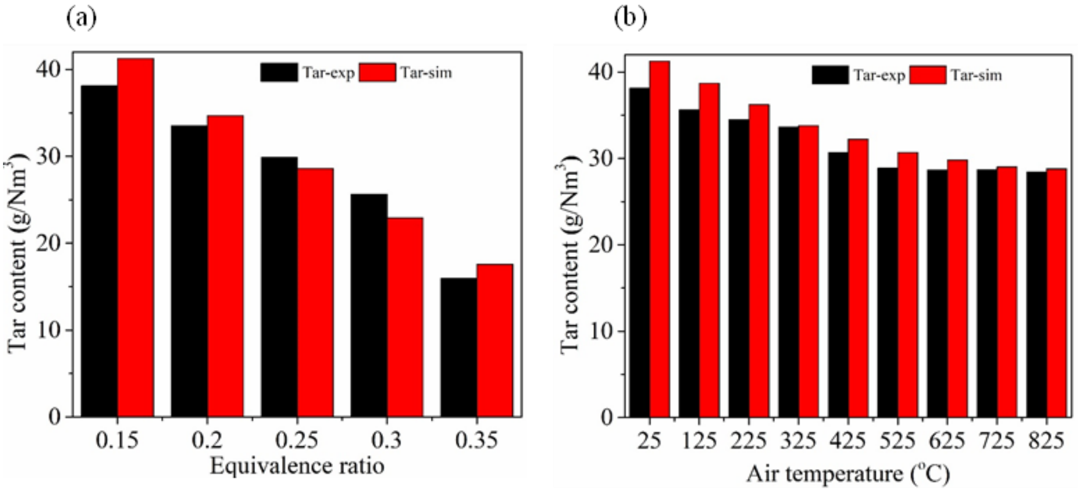

Figure 4.11: Experimental and Simulation Results of Tar Content (a) Equivalence Ratio (b) Air Temperature

From Figure 4.11 (b), a root mean square error of 1.8 and a mean absolute error of 5 % were obtained, confirming the model accuracy. It was observed that tar amount reduced with air preheating but stabilized at a temperature of 525 °C. Preheated air improved the overall gasification temperature, enhancing thermal cracking of tar into lighter gases. However, at a temperature of 525 °C, the tar reduction leveled off, indicating that air preheating beyond this temperature was not effecting. As discussed in Section 4.1.3, air preheating up to 525°C resulted in temperatures exceeding 900°C, which is crucial for thermal cracking of tar.

4.3 Numerical Modeling Results

This section presents the results obtained from the validated models. The results on the fluidized bed hydrodynamic behavior are presented first followed by the gasification sensitivity analysis results.

4.3.1 Hydrodynamics Numerical Modeling Results

a) Effect of Temperature on Pressure Drop

In Figure 4.12 shows the effect of temperature on the pressure drop for 500, 335 and 233 μm particles sizes at different velocities. The velocities were selected below and above the minimum fluidization values for the particle sizes and across the temperature range considered.

The superficial velocities of 0.02, 0.05, and 0.1 m/s in Figure 4.12 (a), (b), and (c), respectively, were lower than the minimum fluidization velocities for particles 233, 335, and 500 μm respectively. The figures show that when the velocities below U_{mf} were increased, the pressure drop also increased linearly but did not reach the minimum fluidization point within the range of temperature considered. The linear portion indicates the fixed bed regime. Additionally, it was observed that the pressure drop remained constant when the minimum fluidization point was reached. For instance, in Figure 4.12 (a), the pressure drop increased linearly with a superficial velocity of 0.03 m/s up to a temperature of 300 ^{o}C and then assumed a constant value. This indicates that the bed remained in a fixed bed regime until a bed temperature of 300 ^{o}C and then transitioned to the fluidized bed regime.

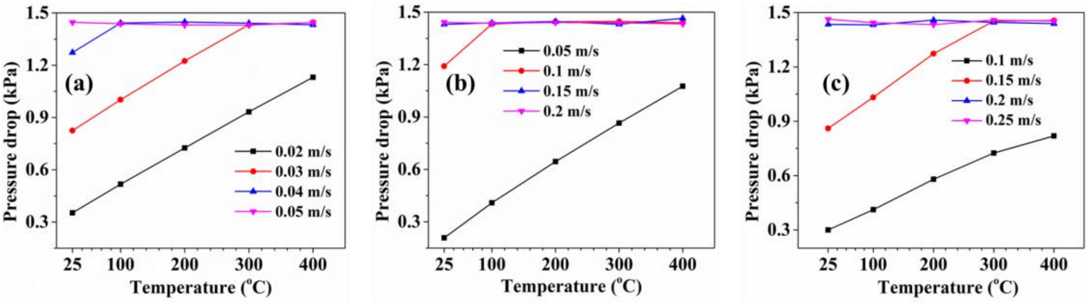

Figure 4.12: Effect of Temperature on Pressure Drop (a) 233 (b) 335 (c) 500 μm

In Figure 4.12 (a), (b) and (c), for a flow rate of 0.05, 0.2, and 0.25 m/s, the pressure drop remained constant across the entire range of temperature. This observation suggests that these flow rates exceeded the minimum fluidization velocity for 233, 335, and 500 μm particles and hence the bed remained in a fluidized bed regime. Al-Farraji and Taofeeq (2020) reported that the pressure drop at the minimum fluidization velocity remains constant and equals the weight of the bed materials per unit area of the fluidized bed column.

b) Effect of Temperature and air Flow Rates on Bubble Evolution and Size

Bed void fraction is the volume of air or empty spaces present within the bed and indicates bubble growth and size within the fluidized bed systems (Al-Akaishi et al., 2017). Figure 4.13 shows contours of solid volume fraction (VoF) at different air velocities and temperatures for 500 and 335 μm sand particle sizes. From these figures, the areas of higher or lower solid concentration can be distinguish, identifying spatial patterns and gradients in the distribution of solid material.

It can be observed from these contours that the onset of air bubble formation varied at different air flow rates. At 25 ^{o}C, (Figure 4.13 (a)), air bubbles emerged at 0.2 m/s. However, when the bed material temperature was raised to 400 ^{o}C, (Figure 4.13 (e)), the bubbles appeared at a lower air flow rate of 0.13 m/s.

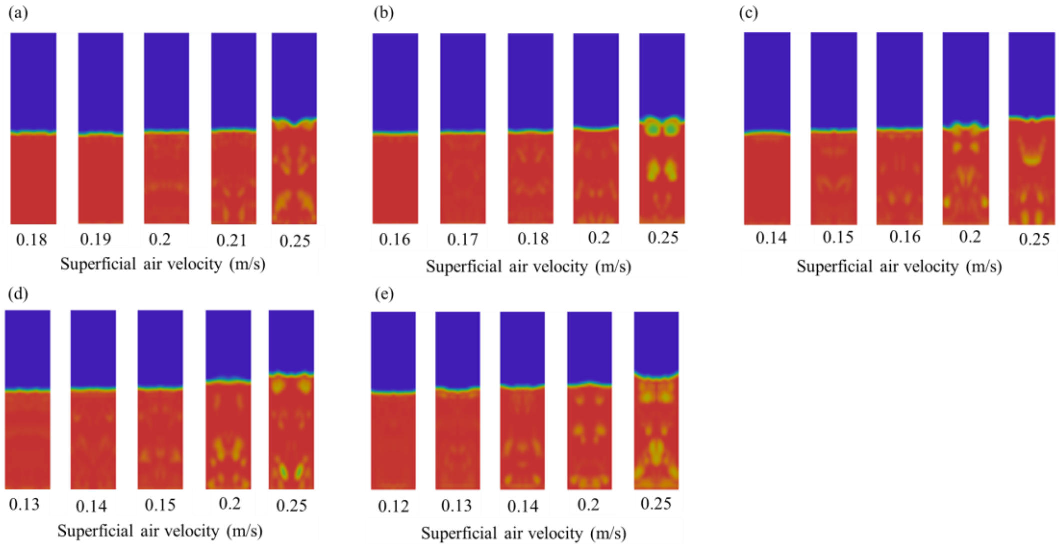

Figure 4.13: Solid Volume Fraction for dp=500 μm at Temperatures of (a) 25 (b) 100 (c) 200 (d) 300 (e) 400 ^{o}C

It was further noted that prior to emergence of the bubbles, the contours indicated a relatively stable bed height, suggesting a fixed bed regime. However, the bed height began to change when bubbles emerged, indicating a transition to a fluidized bed regime. The bed height increased gradually and became more pronounced as the air flow rate exceeded the minimum fluidization velocity (U_{mf}). For instance, in Figure 4.13 (e), the bed height remained relatively constant prior to reaching a flow rate of 0.13 m/s. However, the bed height started to vary when the bubbles appeared and continued to expand steadily thereafter.

In terms of bubble evolution and size, it was observed that smaller bubbles appeared at air flow rates above U_{mf}. However, as the air flow rate was raised, the bubbles exhibited growth in both intensity and size. For example, Figure 4.13 (e) illustrates the evolution of bubbles from an air velocity of 0.13 m/s to 0.25 m/s when maintaining the same bed temperature. As more air was supplied, the bubbles increased in both magnitude and size and appeared to burst as they approached the top of the bed. Al-Akaishi et al. (2017) reported that small bubbles tend to merge and coalesce as they move upwards, forming larger bubbles which burst at the top of the bed.

Figure 4.14 shows transient bubble evolution for the particle size of 500 μm at bed temperature of 25 ^{o}C and superficial air velocity of 0.25 m/s which was above the minimum fluidization velocity. As the air was introduced, a voidage wave was noticed at 0.5 s and the bed was visibly unstable for the upward movement of the bed materials. Huge bubbles were observed at 1 s and 1.5 s, with the bed achieving a maximum expanded height of approximately 0.23 m and the bubbles bursting. The suppression of the growth of bubbles at 2 s was because of the falling down of the bed materials which happens when the bed attains a maximum height. Additionally, it was observed that the big unstable air bubbles were not observed further after 3 s.

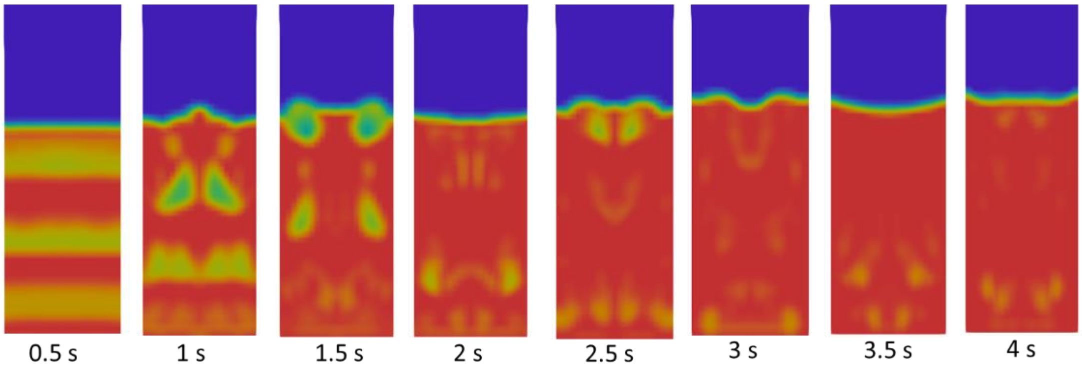

Figure 4.14: Instantaneous Solid Volume Fraction for dp=500 μm at V= 0.25 m/s

c) Effect of Temperature and Air Flow Rates on the Expanded Bed Height

Figure 4.15 illustrates the effect of temperature on the expanded bed height at various airflow rates. In Figure 4.15 (a), no bed movement was observed at an airflow rate of 0.17 m/s between 25 °C and 100 °C. Beyond this temperature, the bed height increases linearly with temperature. This indicates that the bed remained in a fixed bed regime between 25°C and 100°C and transitioned to a fluidization regime beyond 100 °C. The increase in bed height at higher temperatures is attributed to the expansion of air, which increases local velocities and creates more air spaces within the bed materials, resulting in an overall increase in height.

In Figure 4.15 (b), a linear relationship was observed between bed movement and an air flow rate of 0.25 m/s, indicating a fluidized bed regime across the entire temperature range. At 25 °C, the expanded bed height was approximately 0.238 m, increasing by 17% at 400 °C. Besides air expnsion at high temperatures, this increament can also be attributed to decreased cohesive forces between particles at elevated temperatures, as reported by Shao et al. (2019). Reduced inter-particle forces enhance the mobility of bed materials, leading to improved fluidization and a greater expanded height at higher temperatures.

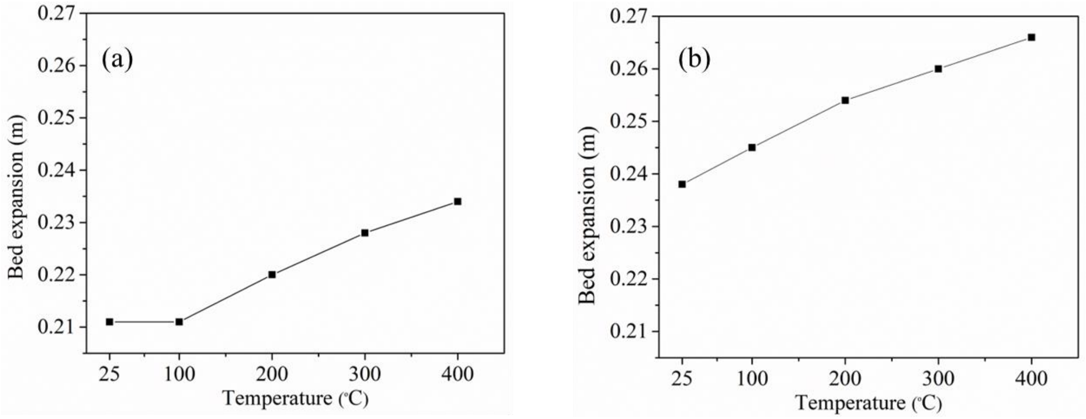

Figure 4.15: Bed Expansion for the Particle Size of 500 μm At Air Flow Rates of (a) 1.7 (e) 0.25 m/s

Figure 4.16 illustrates the effect of air flow rates on the expanded height. According to the figure, the bed height remained constant until the minimum fluidization point was reached. For instance, at 25 °C (Figure 4.16 (a)), the bed height did not change until a superficial velocity of 0.2 m/s was reached. However, at 100 °C, the velocity required decreased by about 10 %. A similar trend was observed for the sand particle sizes of 335 and 233 μm, as seen in Figure 4.16 (b) and (c). At 25 ^{o}C, the bed remained static until air flow rates of 0.12 and 0.045 m/s were reached for particle sizes 335 and 233 μm, respectively. Beyond these velocities, the bed height increased steadily. This pattern was consistent across different temperatures. Shukrullah et al. (2019) observed a similar pattern in their experiments with a swirling fluidized bed at room temperature, noting that the bed height remains constant before reaching Umf and then increases as air velocity rises beyond Umf.

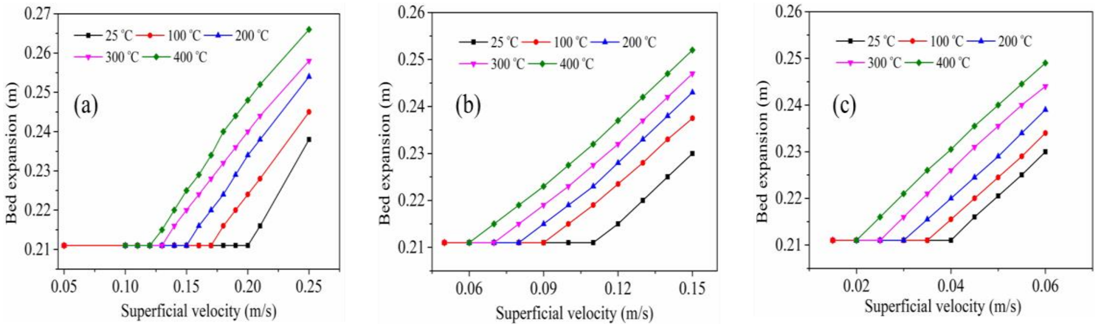

Figure 4.16: Effect of Air Velocity on Bed Expansion for the Particle Sizes: (a) 500 μm (b) 335 μm (c) 233 μm

d) Effect of Temperature on Mean Porosity

In Figure 4.17, the relationship between the mean porosity and the lateral distance is depicted at various temperatures, while maintaining an air velocity at 0.25 m/s, which exceeded the minimum fluidization velocity within the considered temperature range. The figure shows an increase in bed porosity with rising temperature. Two distinct low-porosity peaks were observed near the wall and at the center of the fluidized bed. These peaks indicate the presence of solid-phase clusters, leading to a higher solid volume fraction and decreased porosity. The no-slip condition applied at the walls in simulations cause lower particle mobility, resulting in a denser region with lower porosity near the walls. Additionally, during fluidization, bed material rises and falls towards the center, increasing the likelihood of a material slug forming at the core, especially in narrow bed diameters. Kumar and Agarwal (U. Kumar and Agarwal, 2017) investigated fluidized bed hydrodynamics at ambient temperature conditions and reported similar trend.

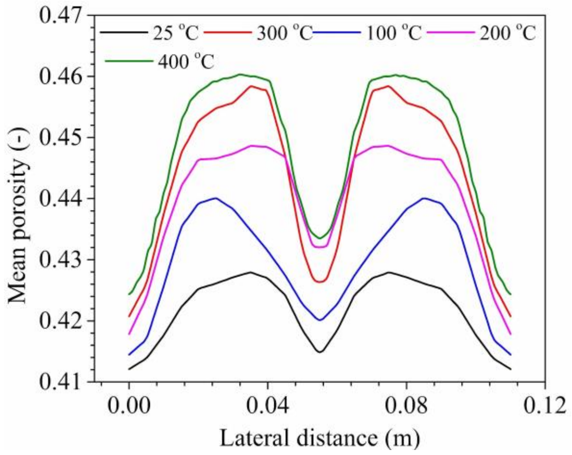

Figure 4.17: Variation of Bed Porosity with Temperature

e) Residuals

Typical residual graphs for selected cases were plotted as shown in Figure 4.13. Oscillations were observed in the residuals and this could be likely due to the constant change of flow which is expected in bubbling fluidized beds. However, the residuals were sufficiently for the voidage, solid concentration and dynamic pressure. They were lower than 10^{-5}, which was expected as this was the convergence criteria discussed in Section 3.7.8. These parameters were selected for residuals because they are critical fluidized bed hydrodynamic parameters.

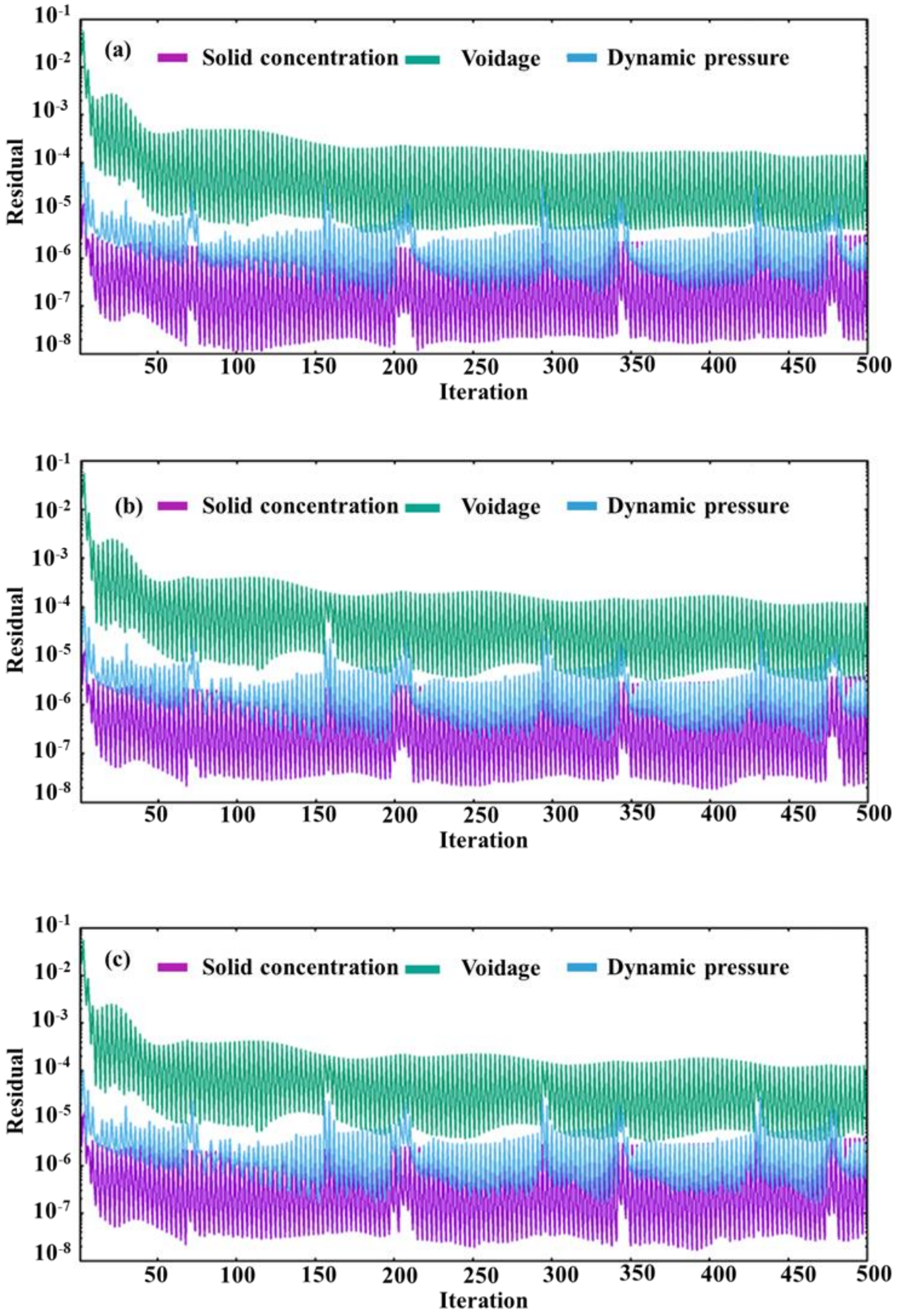

Figure 4.18: Residual Plots for Particle Sizes (a) 500 μm (b) 335 μm (c) 233 μm

4.3.2 Gasification Sensitivity Analysis

The gasification numerical model was applied for the simulation of macadamia nutshells gasification process after successful validation. Sensitivity analysis was conducted to explore the effects of key gasification parameters such as the equivalence ratio, air preheating, gasification pressure, and oxygen-enrichment on the gasification process. In this study, three important gasification metrics were used to assess the gasification process i.e., syngas gaseous concentration, higher heating value (HHV), gas yield and the tar amount in the syngas.

a) Equivalence Ratio

The influence of equivalence ratio (ER) on gas composition was examined in the study, and the results are presented in Figure 4.19. ER values were varied between 0.15 and 0.4 in a batch process. while the air temperature was kept constant at 25 ^{o}C. It was observed that as the equivalence ratio increased, the concentrations of carbon monoxide, hydrogen, and methane decreased. Between the ER range of 0.15 and 0.4, the CO concentration dropped from 13.8 % to 11.9 %, representing a decrease of 13.8 %. Similarly, the H_2 concentration decreased from 8.5 % to 4.1 %, indicating a reduction of 51.8 %. Furthermore, the CH_4 concentration experienced a significant drop from 2.2 % to 0.25 %, resulting in a substantial decrease of 88.6 %. It was however observed that the biggest change occurred in the ER range of between 0.33 and 0.4. It was noted that within this narrow range, there was a rapid decrease in the concentrations of CH_4 and CO. For instance, CH_4 concentration dropped from 1.56 % to 0.25 %, while CO concentration decreased from 12.9 % to 11.9 %.

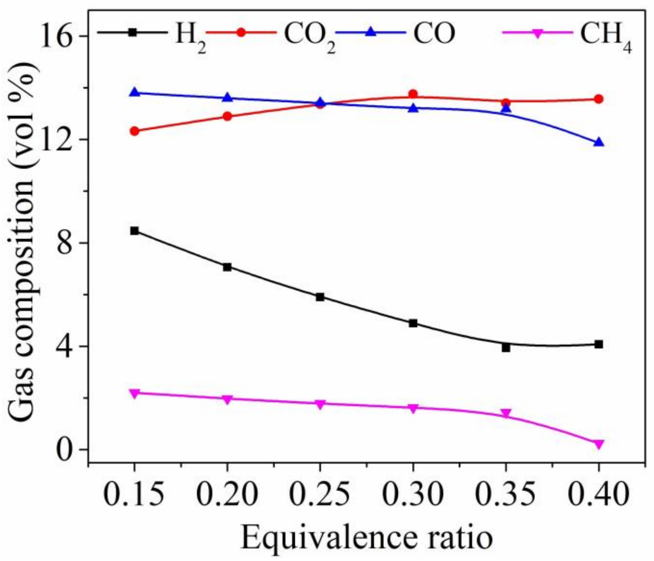

Figure 4.19: Effect of Equivalence Ratio on Gas Composition

The observed decrease in CO, CH_4 and H_2 concentrations with increasing ER can be attributed to the changes in the gasification reactions and the availability of more oxygen. Higher ER values typically imply a higher ratio of oxygen to fuel, resulting in more complete combustion and promotion of oxidation reactions as shown in reactions (4.6) and (4.7). This consumed carbon monoxide and hydrogen and produced carbon dioxide and steam.

$$CO + 0.5O_2 \longrightarrow CO_2 \qquad 4.6$$

$$H_2 + 0.5O_2 \longrightarrow H_2O \qquad 4.7$$

Methane, being a hydrocarbon, is formed as a byproduct of incomplete combustion. In the gasification process, unreacted carbon can react with hydrogen to produce additional methane, according to reaction (4.8). However, increasing the equivalence ratio promotes more complete combustion, decreasing unreacted carbon available for reacting with hydrogen. This reduces methane production.

$$C + H_2 \longrightarrow CH_4 \qquad 4.8$$

Within the same range of the equivalence ratio, the concentration of CO_2 rose from 12.3 % to 13.6 %, an increase of 10.56 %. The rise in CO_2 concentration can be attributed to the high amount of oxygen associated with higher ER values. This promotes more efficient combustion and oxidation processes within the gasifier, favoring oxidation of char and CO which forms more CO_2.

Figure 4.20 presents syngas higher heating value, tar content and gas yield as function of the equivalence ratio. Figure 4.20 (a) revealed that syngas HHV reduced when ER was increased, with the most significant decrease of 24.4 % observed within the ER range of 0.33 to 0.4. The decrease in syngas HHV can be attributed to its direct correlation with the concentration of combustible gas species, which decreases with ER as discussed earlier. Combustible gases are the primary contributor to the energy content of the syngas, and their depletion results in a reduction in syngas HHV as reported by Abdoulmoumine et al. (2014).

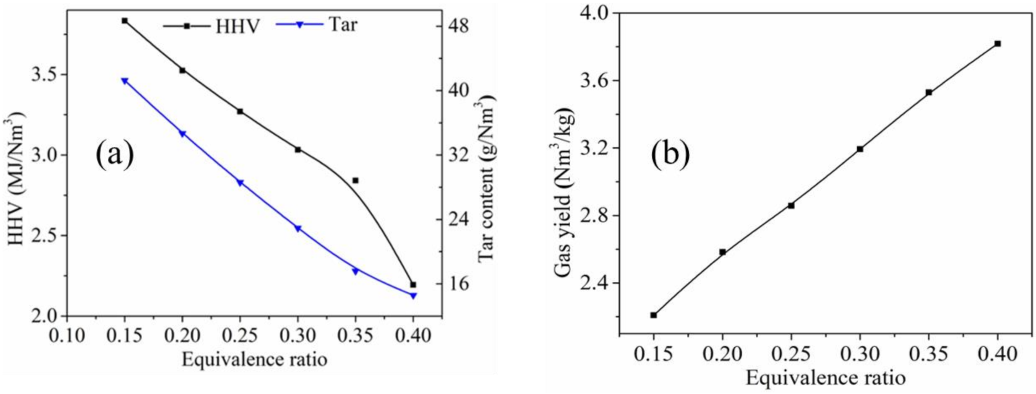

Figure 4.20: Effect of Equivalence Ratio on (a) Syngas HHV and Tar Content (b) Gas Yield

Figure 4.20 (a) shows that increasing the equivalence ratio from 0.15 to 0.4 led to a reduction of 65 % of tar. This can be attributed to the increased amount of oxygen supplied at higher ER which promoted more complete combustion and oxidation processes. As a result, the volatile hydrocarbons that contribute to tar formation were more effectively oxidized, leading to a decrease in tar production (Guo et al., 2021). Additionally, lower values of ER tend to favor pyrolysis, which results in increased tar formation. However, as the equivalence ratio value is raised, the gasification process shifts towards combustion, leading to higher gasification temperatures and promoting thermal cracking of tar (Puig-Gamero et al., 2021).

Referring to Figure 4.20 (b) on the effect of the equivalence ratio on gas yield, it was noted that the gas yield increased with ER, with the highest value observed at an ER of 0.4. When ER was varied from 0.15 to 0.4, the gas yield rose by approximately 65 %. The increased supply of oxygen at higher ER values promoted the combustion and oxidation reactions, leading to a more complete conversion of the biomass into gaseous products, which increased the gas yield.

b) Air Preheating

Figure 4.21 shows gas composition as a function of air preheating. The results indicated that air preheating led to an increase in gaseous concentration, with hydrogen registering the highest increase of 73.7 %. Carbon monoxide concentration increased by 15.78 % while methane and carbon dioxide concentrations reduced by 18 and 4 %, respectively.

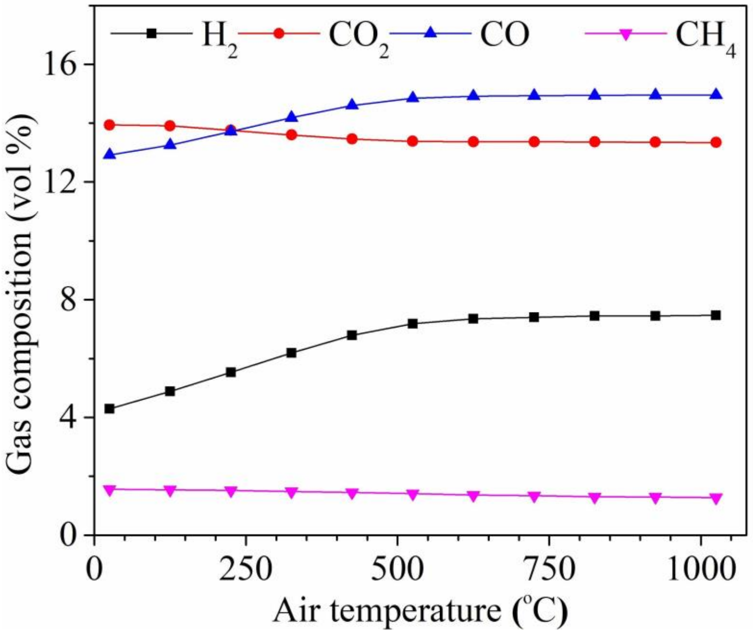

Figure 4.21: Effect Air Preheating on Gas Composition

It was further observed that the significant change in gaseous concentration happened within the temperature range of 25 to 550 °C, while there was negligible change observed beyond this temperature.

The increase in gaseous concentration can be attributed to the additional thermal energy within the gasifier resulting from the preheated air. This led to a temperature rise, promoting the water-gas reaction ($C + H_2O \longrightarrow CO + H_2$), where steam interacts with carbon-based compounds to produce hydrogen and carbon monoxide. Methane reformation reaction ($CH4 + H2O \longrightarrow CO + 3H2$), is also favored at higher temperatures to produce more carbon monoxide and hydrogen at the expense of methane. The concentration of CO_2 reduced slightly due to promotion of endothermic Boudouard reaction ($C + CO_2 \longrightarrow 2CO$), which favors production of carbon monoxide and consumption of carbon dioxide. The findings in this study are similar to the experimental study by Doherty et al. (2009) on gas composition using hemlock wood as the biomass waste. They used an ER of 0.29 and reported that air preheating was only effective up to 560 ^oC.

The effect of air temperature on syngas HHV, tar content, and gas yield is presented in Figure 4.22. It can be observed from Figure 4.22 (a) that there was a corresponding increase in syngas HHV as the air temperature increased. This rise continued until a constant value was reached at 550 ^oC. The improvement in syngas HHV with air preheating can be attributed to the corresponding rise in the concentration of combustible gases at elevated temperatures, as depicted in Figure 4.21. Syngas HHV was determined from the energy densities of these gases as shown in Equation (3.45).

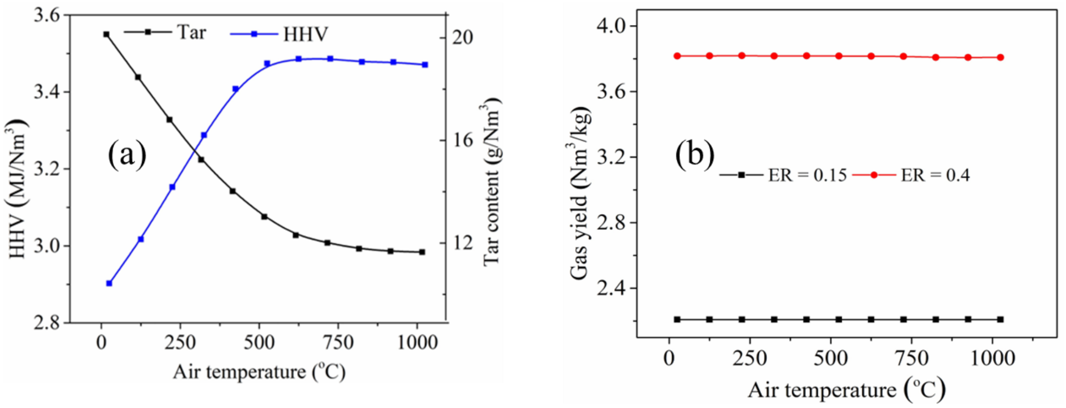

Figure 4.22: Effect of Air Preheating on (a) Syngas HHV (b) Gas Yield

On the other hand, tar content decreased with increasing air temperature and then levelled off. This can be attributed to the high gasification temperatures, promoting thermal cracking of tar into lighter gases. However, it is noteworthy that the effectiveness of the tar cracking was limited to air preheating up to 625 °C, beyond which there was minimal tar reduction. On the other hand, it was observed from Figure 4.22 (b) that the gas yield remained fairly constant and did not show any change with air preheating.

c) Gasifier Pressure

The impact of gasifier pressure on syngas composition is illustrated in Figure 4.23. Gasifiers typically operate within the pressure range of 1 to 10 atm, as reported in previous studies (Szul et al., 2021). This range was used and the simulations were conducted using an equivalence ratio 0.33

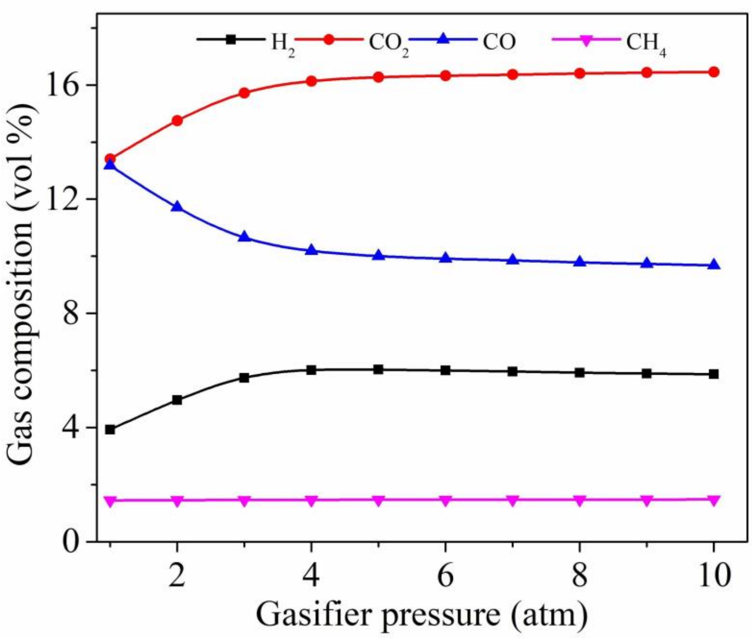

Figure 4.23: Effect of Gasifier Pressure on Gas Composition

From this figure, methane concentration did not show a notable change with the pressure. The concentration of hydrogen and carbon dioxide rose by 50 and 16 %, respectively, while the concentration of carbon monoxide decreased by 17 % between 1 and 4 atm. The concentrations of these gases remained constant beyond 4 atm. The changes in gas concentration can be attributed to the pressure effect on gasification kinetics. Higher pressure enhances the availability and diffusion of reactants, resulting in more efficient steam reforming and water-gas shift reactions. These reactions contribute to the production of H_2 and CO_2. A similar trend on the effect of pressure on coal gasification was reported in a study by Timofeeva and Ermolaev (2022), who used a pressure range of 1-4 MPa and found that higher pressure increased syngas production. Furthermore, Szul et al. (2021) reported that the optimal operating pressure for pressurized biomass gasifiers is between 3 to 4 atm.

The effect of gasifier pressure on syngas higher heating value and tar content is illustrated in Figure 4.24**.** As aforementioned, the concentrations of combustible gas species were affected by the gasifier pressure, yet the syngas higher heating value, which depends on these gases, remained fairly constant regardless of the pressure. Syngas HHV was obtained using energy densities of CO, CH_4 and H_2 as shown in

Equation (3.45) and the changes in the concentration of these gases seemed to offset each other. A study by Vaezi et al. (2011) reported a similar trend on syngas energy density.

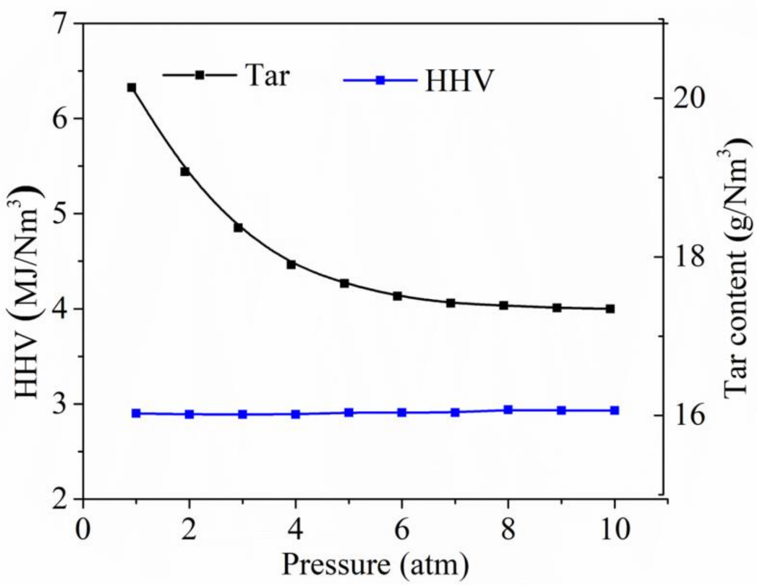

Figure 4.24: Effect of Gasifier Pressure on Syngas HHV and Tar content

It was also observed from the same figure that the tar content in syngas decreased by 11 % between the pressures of 1 and 4 atm. As Vaezi et al. (2011) pointed out, increasing the gasifier pressure raises gasification temperatures, which facilitates the thermal cracking of tar into lighter gases, reducing its content in syngas.

d) Oxygen Enrichment

Oxygen enrichment enables to study the effects of different gasifying agents on gasification performance, including air, oxygen-enriched air, and pure oxygen. In this simulation study, the oxygen content was varied from 21 % (typical atmospheric air composition) to 100 % (pure oxygen). Figure 4.25 illustrates the influence of oxygen enrichment on gas compositions using an ER of 0.33 and air temperature of 25 °C. In addition to monitoring the concentrations of combustible gases, the nitrogen concentration was also considered to examine its relationship with oxygen enrichment.

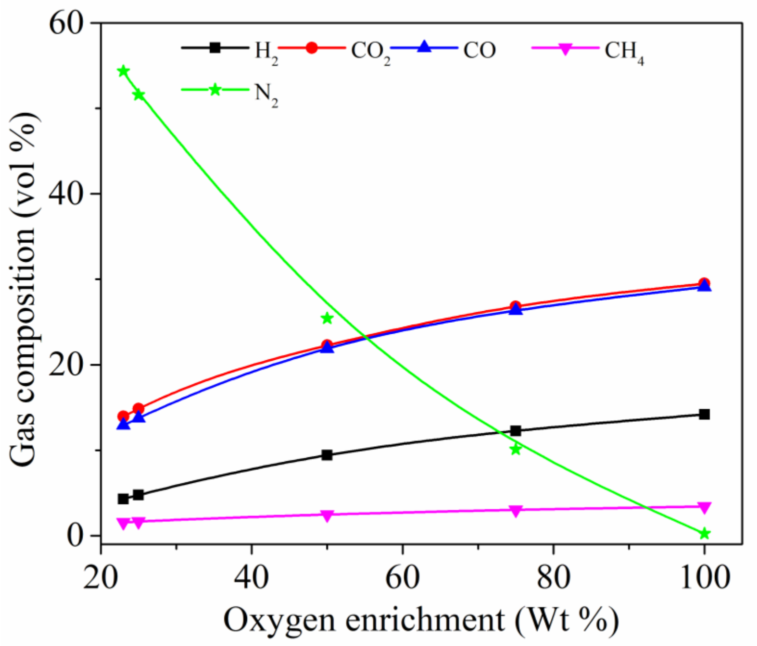

Figure 4.25: Effect of Oxygen Enrichment on Gas Composition

Figure 4.25 clearly shows that the concentrations of H_2, CO, and CH_4 rose by 238, 109, and 113 % respectively. This improvement coincides with a drastic reduction in nitrogen concentration, dropping from 54 % to 0 %. The availability of more oxygen for combustion enhanced the gasification conditions. Unlike hydrogen and carbon monoxide, nitrogen does not actively participate in the syngas energy density but dilutes it instead, reducing the concentration of valuable gases. Hence, minimizing the presence of nitrogen in syngas enhances its quality and usefulness. Experimental work by Vaezi et al. (2011), using heavy fuel as feedstock, and Park et al. (Park et al., 2018), on gasification of hardwood sawdust, reported similar trend as found in this simulation work.

Figure 4.26 presents the effect of oxygen enrichment on syngas higher heating value and tar content. It was observed that increasing the oxygen enrichment from raw air to pure oxygen led to a reduction in tar content by approximately 47 %. Higher oxygen concentration increases the gasification temperature and promotes the cracking of tar into lighter gases. These results agree with experimental studies conducted by Park et al. (2018) who observed a tar reduction of 52.46 % when using oxygen-enriched air with hardwood sawdust as the biomass fuel.

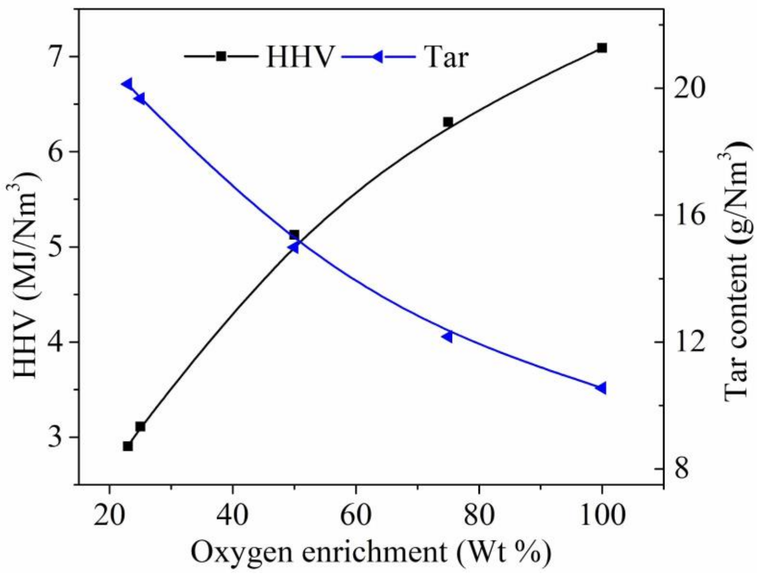

Figure 4.26: Effect of Oxygen Enrichment on Syngas HHV and Tar Content

Furthermore, the heating value of the syngas was greatly improved by 144 % as the oxygen level increases from air to pure oxygen. This improvement can be attributed to the increased concentration of combustible gas species, including CO, H_2, and CH_4, which are the primary contributors to the heating value of syngas. Vaezi et al. (2011) conducted experiments using heavy fuel oil and achieved an improvement of 108 % in the calorific value of the syngas.

4.4 Regression Analysis

The results from Section 4.3.2 were used for the optimization of the gasification process parameters. Three parameters viz the equivalence ratio, air temperature and the gasifier pressure shown in Table 4.1 were taken as the input variables. This method has been used by other authors but with different objectives (Mojaver et al., 2019; D. K. Singh and Tirkey, 2021). The data was used to develop regression models.

Table 4.1: Optimization Range of the Input Parameters

Input factor	**Code level**			
	Units	**Low (-1)**	**Center (0)**	**High (+1)**
Equivalence ratio (A)	-	0.15	0.24	033
Air temperature (B)	^{o}C	25	325	625
Gasifier pressure (C)	atm	1	2.5	4

Source: (F. Njuguna et al., 2023)

In this study, a three-level factorial Box-Behnken design was employed, resulting in a total of 17 simulation runs. Table 4.2 shows variables considered and their respective outputs. The small residuals showed that the regression models were satisfactory.

Table 4.2: Inputs Variables, Responses and Residuals

Run	A	B	C	Hydrogen			Carbon monoxide			Methane			Higher heating value			Tar content		
				Aspen	Regression	Residual	Aspen	Regression	Residual	Aspen	Regression	Residual	Aspen	Regression	Residual	Aspen	Regression	Residual
1	0.15	325	4	11.21	11.30	-0.0950	13.26	13.51	-0.2489	2.21	2.19	0.0123	4.13	4.12	0.0087	27.79	27.69	0.0975
2	0.33	25	2.5	5.63	5.64	-0.0115	11.14	11.28	-0.1445	1.55	1.53	0.0218	2.84	2.92	-0.0812	18.05	18.06	-0.0128
3	0.15	625	2.5	11.41	11.40	0.0115	14.34	14.19	0.1445	2.20	2.22	-0.0158	4.29	4.35	-0.0558	26.89	26.87	0.0128
4	0.15	325	1	9.72	9.66	0.0626	14.39	14.19	0.1966	2.20	2.20	0.0051	4.08	4.08	0.0012	31.06	31.43	-0.3677
5	0.24	325	2.5	8.65	8.65	0.0000	13.50	13.50	0.0000	1.82	1.82	-0.0077	3.66	3.63	0.0251	23.95	23.95	0.0000
6	0.24	325	2.5	8.65	8.65	0.0000	13.50	13.50	0.0000	1.82	1.82	-0.0077	3.66	3.63	0.0251	23.95	23.95	-9.4E-6
7	0.15	25	2.5	9.98	9.96	0.0209	12.34	12.43	-0.0922	2.20	2.17	0.0315	3.84	3.84	-0.0019	38.94	38.68	0.2574
8	0.24	25	1	6.11	6.20	-0.0835	13.45	13.56	-0.1044	1.82	1.84	-0.0270	3.32	3.36	-0.0436	30.40	30.29	0.1103
9	0.24	625	4	9.66	9.58	0.0835	14.76	14.65	0.1044	1.82	1.80	0.0131	3.96	3.91	0.0501	17.04	17.15	-0.1103
10	0.33	325	1	6.14	6.04	0.0950	14.27	14.02	0.2489	1.46	1.44	0.0148	3.28	3.15	0.1279	11.66	11.76	-0.0975
11	0.24	325	2.5	8.65	8.65	0.0000	13.50	13.50	0.0000	1.82	1.82	-0.0077	3.66	3.63	0.0251	23.95	23.95	-9.4E-6
12	0.24	325	2.5	8.65	8.65	0.0000	13.50	13.50	0.0000	1.82	1.82	-0.0077	3.66	3.63	0.0251	23.95	23.95	-9.4E-6
13	0.24	25	4	8.38	8.31	0.0741	11.89	11.55	0.3411	1.82	1.85	-0.0342	3.41	3.40	0.0112	26.36	26.72	-0.3550
14	0.33	325	4	7.22	7.28	-0.0626	12.18	12.38	-0.1966	1.49	1.46	0.0220	3.16	3.19	-0.0321	9.84	9.47	0.3677
15	0.24	325	2.5	8.65	8.65	0.0000	13.50	13.50	0.0000	1.82	1.82	-0.0077	3.66	3.63	0.0251	23.95	23.95	-9.4E-6
16	0.33	625	2.5	8.06	8.09	-0.0209	14.13	14.03	0.0922	1.36	1.38	-0.0255	3.47	3.52	-0.0459	9.35	9.60	-0.2574
17	0.24	625	1	8.74	8.81	-0.0741	15.22	15.41	0.1919	1.82	1.80	0.0203	3.90	3.92	-0.0227	19.96	19.60	0.3550
%MAE				0.51			0.94			0.94								

Source: (F. Njuguna et al., 2023)

After conducting the simulation runs, regression models were developed to establish the relationship between the gasification process parameters and the desired responses. The statistical significance of the models was assessed using analysis of variance (ANOVA) with a confidence level of 95 %.

4.4.1 Normal Probability and Residual Plots

The normal probability and the residual plots were used to assess the assumptions of normality and identify influential data points. Studentized residuals were estimated by dividing the residual by an estimate of its standard deviation in order comparable in terms of standard deviations. The plot in Figure 4.27 (a) shows a fairly linear pattern with the majority of points falling along the expected normal values line, suggesting that the assumption of normality was met and indicating normally distributed residuals.

Figure 4.27 (b) shows the plot of externally studentized residuals versus predicted values which was used to assess the performance of the model and identify potential outliers. From this figure, the model exhibited a random scattering of points around the horizontal line at zero, indicating that the residuals were normally distributed and there was no systematic pattern or outliers.

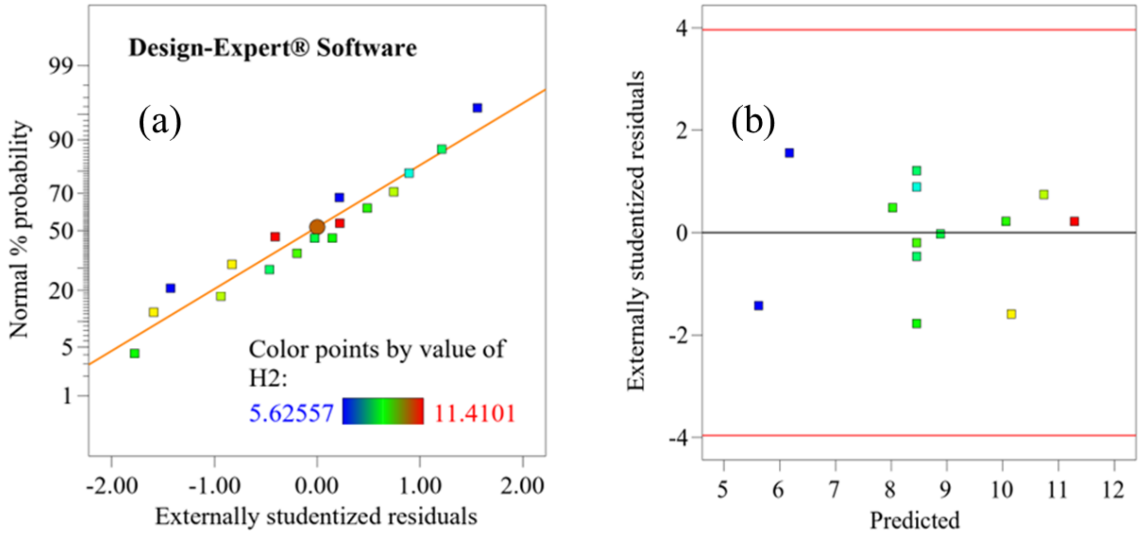

Figure 4.27: H_2 Concentration (a) Normal Probability (b) Residuals

Similarly, the plots of normal probability and the residuals were plotted for the other output responses as shown in Figure 4.28 to Figure 4.31.

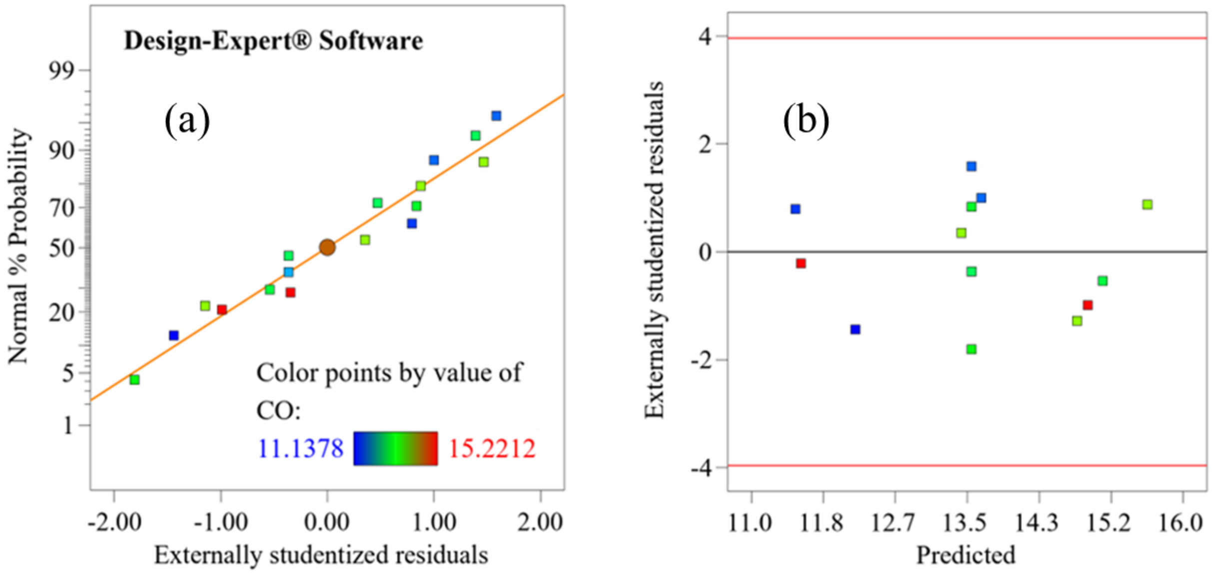

Figure 4.28: CO Concentration (a) Normal Probability (b) residuals

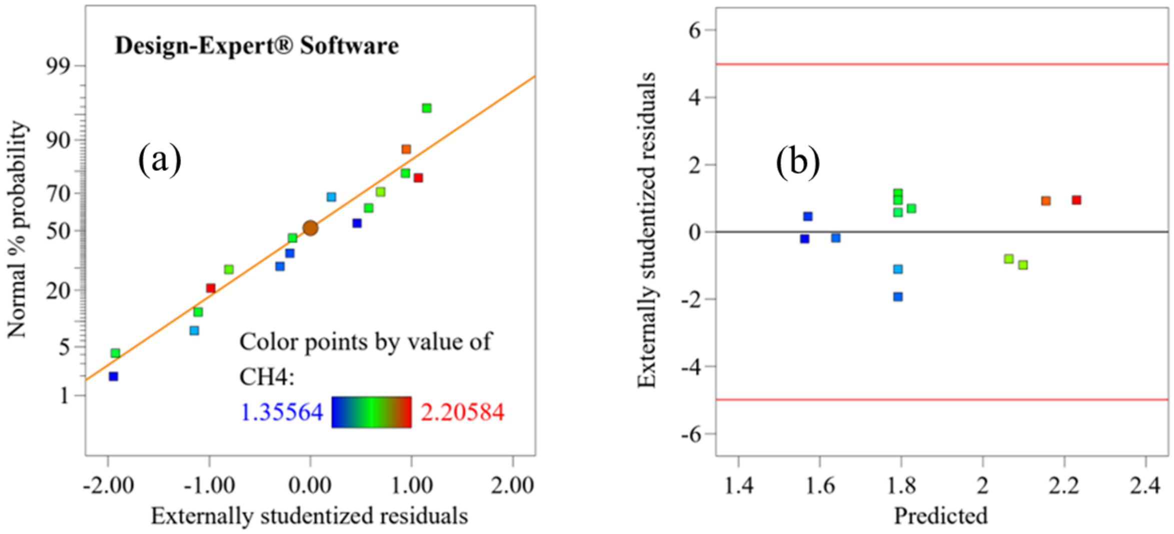

Figure 4.29: CH_4 Concentration (a) Normal Probability (b) Residuals

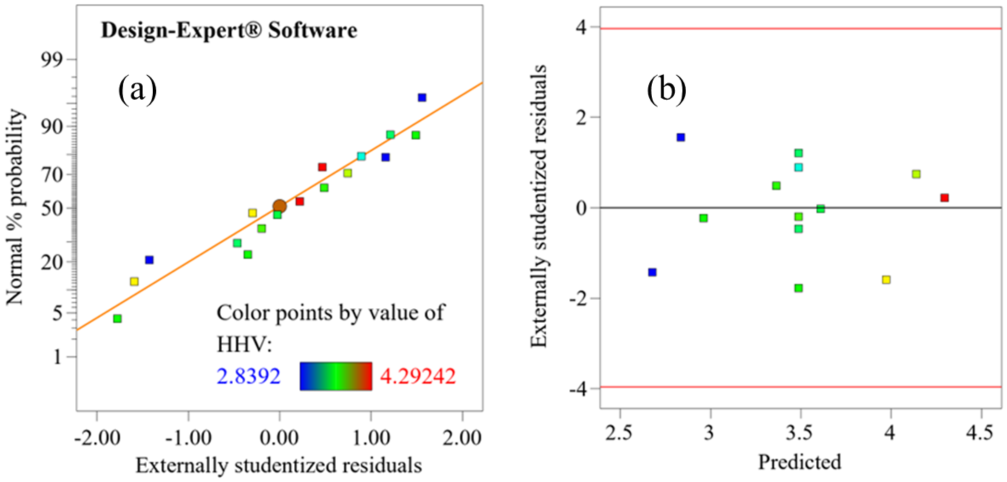

Figure 4.30: Syngas HHV (a) Normal Probability (b) Residuals

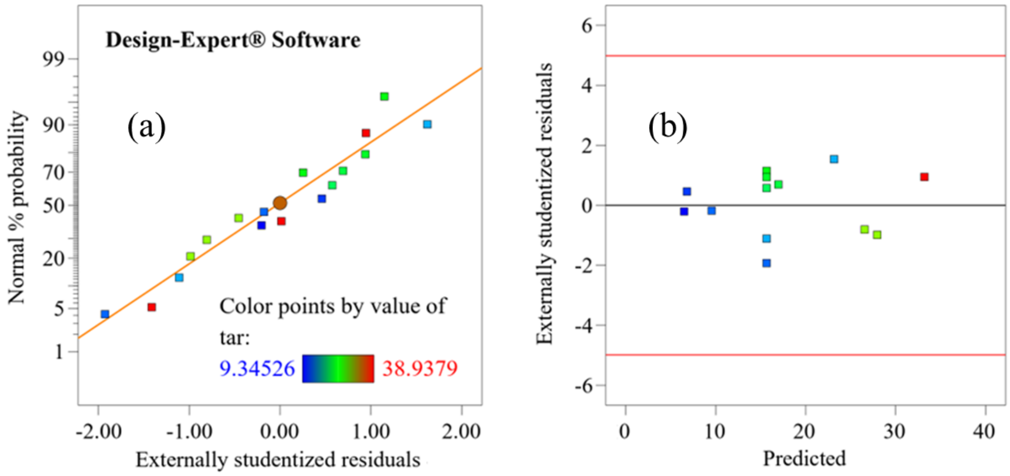

Figure 4.31: Tar (a) Normal Probability (b) Residuals

4.4.2 Analysis of Variance

In this study, the influence of process parameters on the composition of combustible gas was investigated. The primary objective of gasification is typically to maximize the concentrations of H_2 and CO. However, CH_4 concentration was also considered due to its significant impact on the energy of syngas, as measured by its higher heating value. Table 4.3 presents the outcomes of the ANOVA analysis, displaying the responses for gas composition. The regression model for H_2, CO, and CH_4 accounted for 99.88 %, 96.85 %, and 100 % of the data, respectively. The predicted R-squared values closely matched the adjusted R-squared values, differing by less than 0.2. The results indicate that the variables were suitable for the regression model.

F-values were used to evaluate the impact of each parameter on gas compositions. The results revealed that the equivalence ratio had the most influence on hydrogen production, accounting for 68.94 % of the variation. Air temperature and pressure followed, contributing 17.83 % and 9.81 % respectively. Regarding carbon monoxide production, air temperature contributed 63.68 %, while gasifier pressure and the equivalence ratio contributed 18.8 % and 4.68 % respectively. Additionally, the equivalence ratio contributed 98.7 % of methane production, while air preheating had a minimal impact of 0.41 %. Pressure, on the other hand, showed no effect on methane production.

Table 4.3: ANOVA Results for H_2, CO and CH_4

Source	Hydrogen				Carbon monoxide				Methane			
	S-S	Contribution	F-value	P-value	SS	Contribution	F-value	P-value	S-S	Contribution	F-value	p-value
Model	42.29	99.88	632.93	< 0.0001	18.09	98.91	71.70	< 0.0001	1.12	100	309.14	< 0.0001
A	29.17	68.94	3929.56	< 0.0001	0.85	4.68	30.38	0.0009	1.10	98.7	1831.26	< 0.0001
B	7.55	17.83	1016.34	< 0.0001	11.57	63.68	412.67	< 0.0001	0.0046	0.41	7.71	0.0196
C	4.15	9.81	559.30	< 0.0001	3.42	18.80	121.85	< 0.0001	0.0001	0.01	0.1762	0.6835
AB	0.256	0.60	34.44	0.0006	0.245	1.35	8.75	0.0212	0.0093	0.83	15.39	0.0029
AC	0.040	0.09	5.36	0.0537	0.23	1.26	8.20	0.0242	0.0002	0.012	0.280	0.6045
BC	0.453	1.07	61.08	0.0001	0.30	1.64	10.68	0.0137	1.92e-6	0.00	0.0032	0.9562
A^2	0.230	0.54	31.04	0.0008	0.714	3.93	25.46	0.0015	-	-	-	-
B^2	0.055	0.13	7.37	0.030	0.047	0.260	1.69	0.2346	-	-	-	-
C^2	0.411	0.97	55.42	0.0001	0.795	4.38	28.36	0.0011	-	-	-	-
Residual	0.052	-	-	-	0.196	-	-	-	0.0060	-	-	-
Total	42.34	-	-	-	18.29	-	-	-	1.12	-	-	-
R^2	0.9988				0.9693				0.9946			
R^2_{adj}	0.9972				0.9755				0.9914			
R^2_{pred}	0.9804				0.8283				0.9735			

Analysis of variance was also performed to assess the influence of process parameters on the syngas and tar content, and the results are presented in Table 4.4. Based on the sum of squares, the models for syngas higher heating value and the amount of tar accounted for 98.23 % and 99.93 % of the data, respectively. Furthermore, the predicted R^2 values were found to be 0.9708 and 0.9886, respectively, which closely related with the adjusted R^2 values of 0.9904 and 0.9984, respectively.

The equivalence ratio had the most impact on syngas HHV, accounting for 71.97 %, while air temperature accounted for 27.29 % with gasifier pressure having negligible effect. Similarly, the equivalence ratio, air temperature, and pressure contributed to 72.94 %, 20.86 %, and 1.84 % of the tar production, respectively. Based on these findings, regression models represented by Equations (4.9) to (4.13) were developed to estimate the output responses.

$$H_2 = 11.831 - 36.277A + 0.00368B + 1.5955C + 0.00946AB - 0.739AC - 0.000748BC + 28.882A^2 - 1.266B^2 \times 10^{-6} - 0.1389C^2 \qquad 4.9$$

$$CO = 12.4574 + 22.2311A + 0.00105B - 1.17272C + 0.00917389AB - 1.77588AC + 0.000608032\,BC - 50.8301A^2 - 1.17932B^2 \times 10^6 + 0.193129C^2 \qquad 4.10$$

$$CH_4 = 2.7244 - 3.6696A + 0.000351B - 0.00874C - 0.00178AB + 0.0486AC - 1.5378BC \times 10^{-6} \qquad 4.11$$

$$HHV_{syngas} = 4.4534 - 4.7544A + 0.00056B + 0.0882C + 0.0017AB - 0.3101AC - 1.9741BC \times 10^{-5} \qquad 4.12$$

$$Tar\ content = 43.9465 - 3.5590A - 0.03568B + 2.2858C + 0.0310AB + 2.6906AC - 0.000623BC - 246.9025A^2 + 000015 \times B^2 - 0.8277C^2 \qquad 4.13$$

Table 4.4: ANOVA Results; Higher Heating Value and Tar Content

	Higher heating value					**Tar content**				
Source	**SS**	**df**	**% Contribution**	**F-value**	**P-value**	**SS**	**df**	**% Contribution**	**F-value**	**P-value**
Model	2.23	6	99.55	275.48	< 0.0001	983.72	9	99.93	1095.01	< 0.0001
A-ER	1.60	1	71.97	1189.42	< 0.0001	717.91	1	72.94	7192.18	< 0.0001
B-Air temperature	0.6086	1	27.29	451.05	< 0.0001	205.30	1	20.86	2056.75	< 0.0001
C-pressure	0.0010	1	0.04	0.7162	0.4172	18.16	1	1.84	181.95	< 0.0001
AB	0.0085	1	0.34	6.27	0.0313	2.81	1	0.28	28.16	0.0011
AC	0.0070	1	0.31	5.20	0.0458	0.5277	1	0.05	5.29	0.0150
BC	0.0003	1	0.01	0.234	0.6390	0.3144	1	0.03	3.15	0.1192
A^2	-	-	-	-	-	16.84	1	1.71	168.71	< 0.0001
B^2	-	-	-	-	-	7.73	1	0.78	77.43	< 0.0001
C^2	-	-	-	-	-	14.60	1	1.48	146.29	< 0.0001
Residual	0.0135	10				0.6987	7			
Total	2.24	16				984.41	16			
R^2	0.9940					0.9993				
R^2_{adj}	0.9940					0.9984				
R^2_{pred}	0.9708					0.9886				

Source: (Njuguna et al., 2023).

4.4.3 Multi-objective Optimization Using Surface Plots

Figure 4.32 to Figure 4.36 shows the impact of decision variables on the concentrations output responses. These figures present 3D response surfaces and contours for visualizing interactions among the most influential input variables and the output.

It was observed from Figure 4.32 that the highest concentration of hydrogen gas of 11.4 % was achieved by using an equivalence ratio of 0.15, an air temperature of 625 ^{o}C, and a gasifier pressure of 4 atm. The data showed a direct correlation between hydrogen concentration and air temperature, while an inverse relationship was observed with ER values. This behavior can be attributed the high oxygen amount supplied to the gasification at higher equivalence ratios. Consequently, there was an increased tendency for hydrogen to oxidize, forming water and thus reducing hydrogen concentration.

On the other hand, the rise in hydrogen concentration with air temperature was due to the water-gas reaction. As the temperature rises, the equilibrium of the water-gas shift reaction shifts towards increased hydrogen formation, leading to an elevated concentration of hydrogen in syngas.

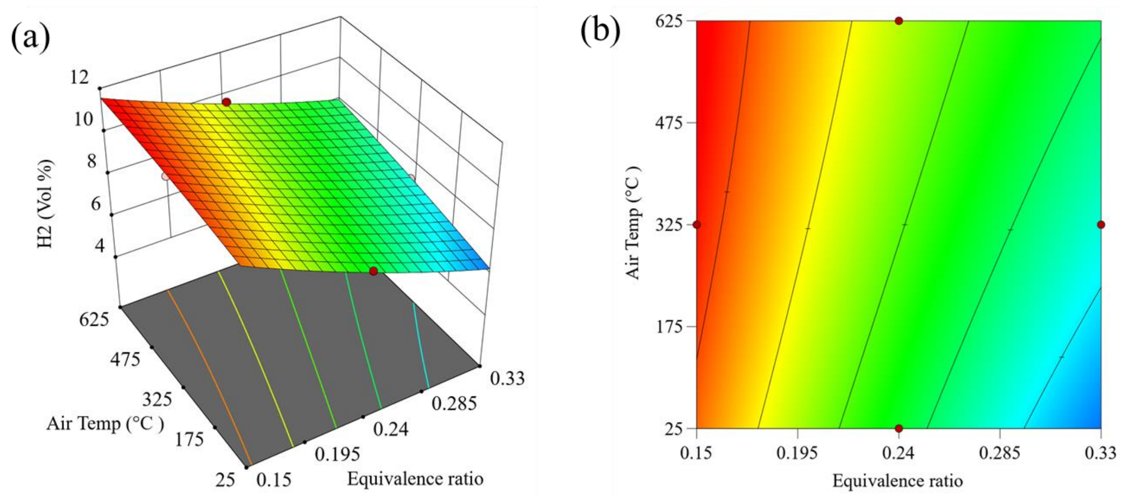

Figure 4.32: Surface Plots for Hydrogen

Figure 4.33 depicts surface plots for the carbon monoxide concentration. The highest concentration of carbon monoxide, amounting to 15.22 %, was achieved under the gasifier pressure of 1 atm, an air temperature of 625 ^{o}C, and equivalence ratio of 0.24. The increased carbon monoxide concentration at higher air temperatures can be attributed to the endothermic water-gas reaction ($CO + H_2O \rightleftharpoons CO_2 + H_2$) and Boudouard reaction ($C + CO_2 \longrightarrow 2CO$). These reactions are favored at elevated temperatures, producing carbon monoxide (Doherty et al., 2009).

Figure 4.34 shows that the methane concentration reached a maximum value of 2.21 % under the conditions of an air temperature of 625 °C, an equivalence ratio of 0.15, and a pressure of 4 atm. Among the variables considered, the equivalence ratio exhibited the most significant influence on methane production.

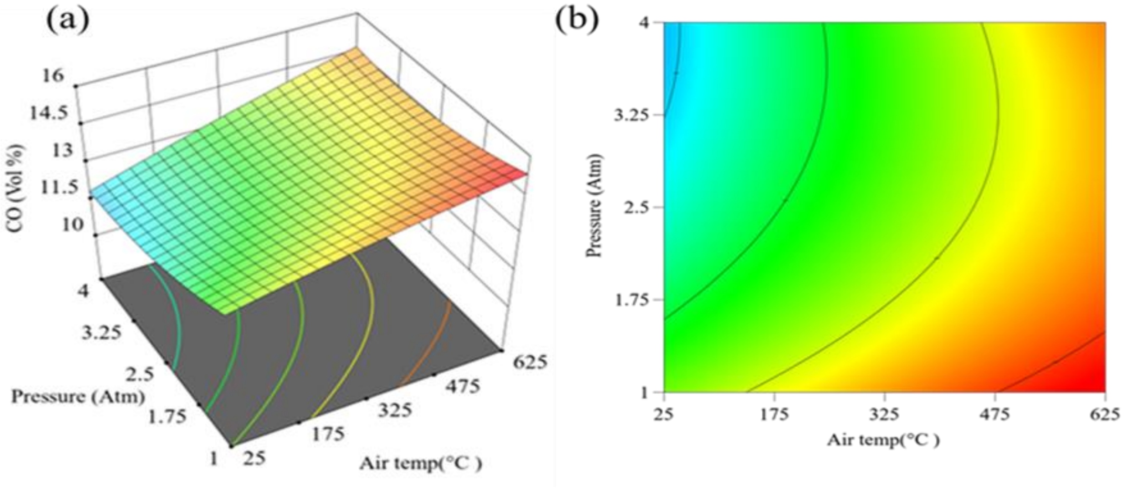

Figure 4.33: Surface Plots for Carbon Monoxide

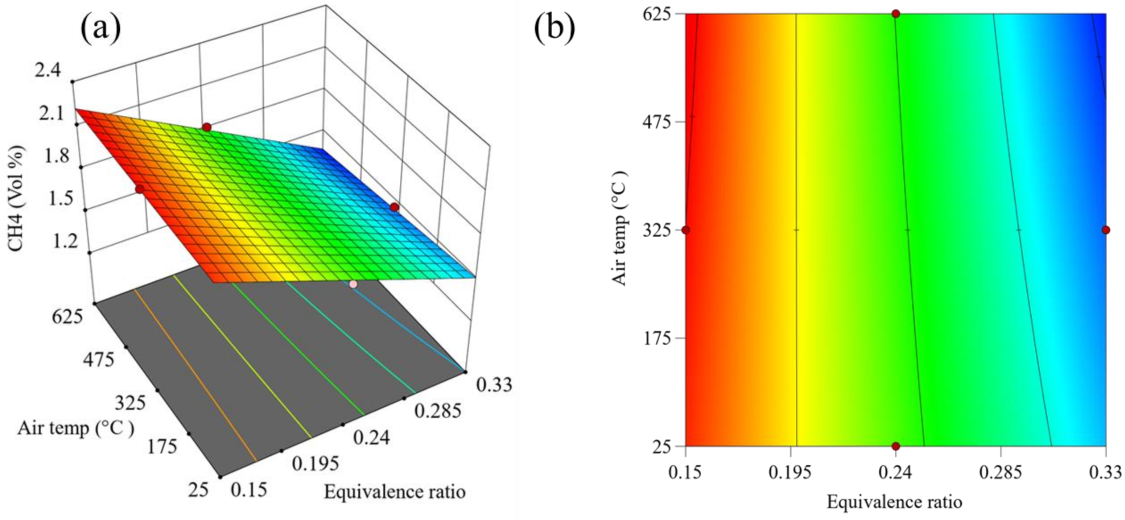

Figure 4.34: Surface Plots for Methane

From Figure 4.34, the methane concentration decreased as ER increased. Methane concentration is high at lower equivalence ratio because it is a byproduct of incomplete combustion. Incomplete carbon conversion favors methane production as depicted in the methanation reaction ($C + H_2 \longrightarrow CH_4$). At lower equivalence ratios, there is a greater proportion of unreacted carbon, leading to a higher concentration of methane in the syngas. The availability of oxygen at higher ER facilitates the complete conversion of carbon, resulting in a decrease in the concentration of unreacted carbon and, consequently decreasing methane concentration (Bonilla et al., 2019).

Figure 4.35 and Figure 4.36 shows 3D and contour surface plots for syngas higher heating value (HHV) and tar content, respectively. The maximum syngas HHV of 4.29 MJ/Nm^3 occurred at an equivalence ratio (ER) of 0.15, an air temperature of 625 ^{o}C, and a pressure of 4 atm. The minimum tar amount of 9.35 g/Nm^3 was realized using an ER of 0.33, air temperature of 625 ^{o}C, and a gasifier pressure of 4 atm.

Syngas HHV rose with temperature because of the corresponding rise in the concentrations of hydrogen, carbon monoxide, and methane as the temperature increased. On the other hand, tar content decreased with temperature because of the availability of oxygen for complete fuel oxidation. Additionally, incomplete combustion happens at lower ER, resulting in increased amount of tar. These observations agree well with the findings of Abdelouahed et al. (2012).

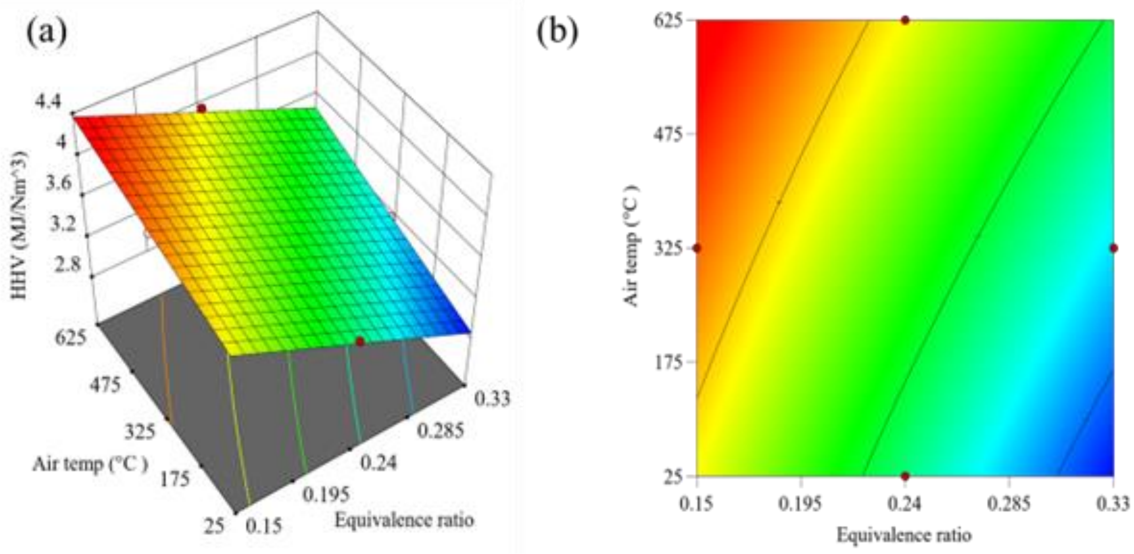

Figure 4.35: Surface Plots for Syngas HHV

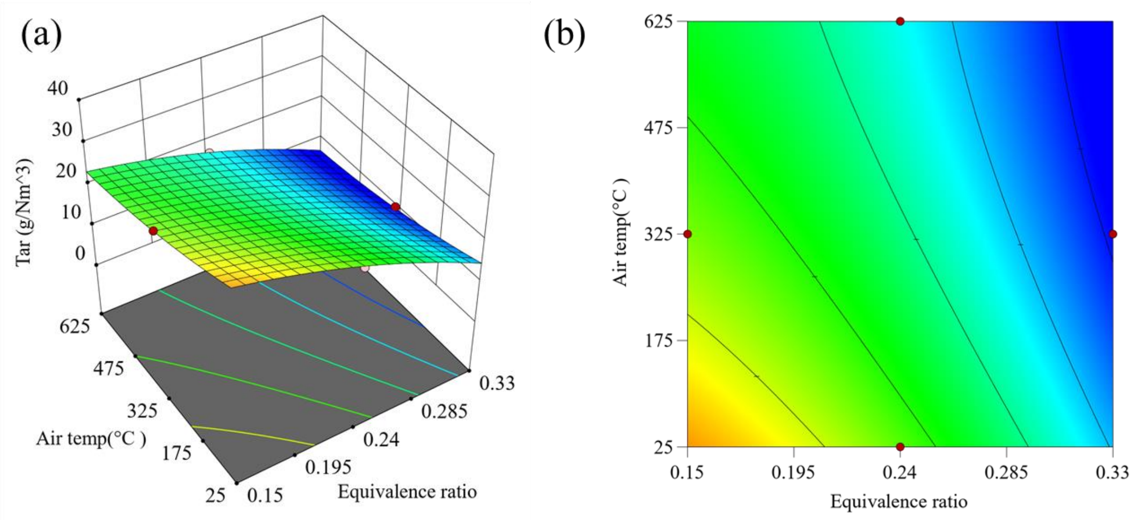

Figure 4.36: Surface Plots for Tar Content

4.4.4 Optimal Conditions

The optimal parameters were achieved by executing the multi-objectiveoptimizationsof the input variables using RSM Box Benkhen Desisn optimizer package of the Design of Expert software. Each response is characterized using a desirability factor that fall between 0 and 1, with the results with the highest desirability factor selected. Table 4.5 provides a summary of the decision variables and the corresponding responses.

Table 4.5: Optimization Data

Output	Level of significance			Optimization goal	Range
	Equivalence ratio (A)	**Air temperature (B)**	**Gasifier pressure (C)**		
Hydrogen	1	2	3	Maximize	5.63-11.41
Carbon monoxide	3	1	2	Maximize	11.14-15.22
Methane	1	2	3	Maximize	1.36-2.21
Syngas HHV	1	2	3	Maximize	2.84-4.29
Tar content	1	2	3	Minimize	9.35-38.94

Level of significance: 1 = most significant, 2 = significant, 3=least significant (F. Njuguna et al., 2023)

Two optimal solutions were obtained for gasifiers. The first solution is a pressurized gasifier, operating at 4 atm, with a composite desirability of 0.85. The optimal values for hydrogen, carbon monoxide, methane, higher heating, and tar were 11.41 %, 14.41 %, and 2.19%, 4.30 MJ/Nm^3, and 23.68 g/Nm^3, respectively. The most optimized points for the equivalence ratio and air temperature were 0.16, an air temperature of 575 ^{o}C, respectively.

The second solution is an atmospheric gasifier, operating at 1 atm, with a composite desirability of 0.89. The optimal values for hydrogen, carbon monoxide, methane, higher heating, and tar were 10.07 %, 14.52 %, 2.21 %,.4.14 MJ/Nm^3 and 29.17 g/Nm^3, respectively. The most optimized points for the equivalence ratio and air temperature were 0.15, an air temperature of 445 ^{o}C, respectively.

CHAPTER FIVE

CONCLUSION AND RECOMMENDATIONS

5.1 Conclusion

The following conclusions can be drawn from this study:

1. Minimum fluidization velocity (U_{mf}) increased with particle size but decreased with temperature. It can therefore be concluded that both the particle size and the temperature of the bed material should be taken into account when designing and operating fluidized bed systems.
2. The expanded bed height increased with the temperature of the bed materials. It is therefore concluded that the temperature effect should be considered when designing for the maximum expanded height in a fluidized bed system.
3. The temperature and air flow rates affected bubble growth and size in the fluidized bed. It can therefore be concluded that changes in these variables can lead to changes in the performance of fluidized bed systems because bubbles determine bed porosity, which in turn affect heat transfer in fluidized bed systems.
4. A peak temperature of 937 °C was attained by employing an ER of 0.35 and gasifying air at room temperature while a peak temperature of 932 °C was attained using a low ER of 0.15 and air at 525 °C. It can therefore be concluded that the combination of a lower ER and air preheating offers a viable alternative to employing a higher ER with air at room temperature, enabling design of compact gasification equipment.
5. An equivalence ratio exceeding 0.33 led to a significant decrease in the higher heating value of syngas. Consequently, it can be concluded that gasifiers should be operated within this range to consistently produce high-quality syngas.
6. Raising the air preheating temperature beyond 625 °C and operating the gasifier at pressures exceeding 4 atm did not result in significant improvements in syngas quality. Therefore, it can be concluded that operating gasifiers within these limits will provide advantage for air preheated and pressurized gasifiers.

5.2 Recommendations

Based on the findings of this research, the following recommendations can be made for future consideration. These recommended tasks were not performed because of resource limitations.

i. Further studies should explore the influence of additional parameters, such as particle shape in order to improve the accuracy of the fluidized bed hydrodynamics.
ii. Further studies should consider the effect of hydrodynamic parameters on heat transfer.
iii. The kinetic model performance can be investigated with other biomass fuels to assess its scalability and facilitate the adoption of gasification technology in diverse biomass applications.
iv. It is recommended to include the analysis of alkali metals in the ultimate analysis, considering their potential impact on the reactivity of SiO_2 in silica sand bed materials.

REFERENCES

Abdelouahed, L., Authier, O., Mauviel, G., Corriou, J. P., Verdier, G., and Dufour, A. (2012). Detailed modeling of biomass gasification in dual fluidized bed reactors under aspen plus. In *Energy and Fuels* (Vol. 26, Issue 6, pp. 3840–3855). https://doi.org/10.1021/ef300411k

Abdoulmoumine, N., Kulkarni, A., and Adhikari, S. (2014). Effects of temperature and equivalence ratio on pine syngas primary gases and contaminants in a bench-scale fluidized bed gasifier. *Industrial and Engineering Chemistry Research*, *53*(14), 5767–5777. https://doi.org/10.1021/ie404401n

AFA. (2021). *Agriculture and Food Authority Nuts and Oil Crops Directorate Validated Statistical Report 2020*. *March 2021*, 1–52.

Ahmed, A. M. A., Salmiaton, A., Choong, T. S. Y., and Azlina, W. A. K. G. W. (2015). Review of kinetic and equilibrium concepts for biomass tar modeling by using Aspen Plus. *Renewable and Sustainable Energy Reviews*, *52*, 1623–1644. https://doi.org/10.1016/j.rser.2015.07.125

Al-Akaishi, A., Valera-Medina, A., Chong, C. T., and Marsh, R. (2017). CFD Analysis of the Fluidised Bed Hydrodynamic Behaviour inside an Isothermal Gasifier with different Perforated Plate Distributors. *Energy Procedia*, *142*, 835–840. https://doi.org/10.1016/j.egypro.2017.12.134

Al-Farraji, A. (2017). *Chemical engineering and reactor design of a fluidised bed gasifier*. Cardiff University.

Al-Farraji, A., and Taofeeq, H. (2020). Effect of elevated temperature and silica sand particle size on minimum fluidization velocity in an atmospheric bubbling fluidized bed. *Chinese Journal of Chemical Engineering*, *28*(12), 2985–2992. https://doi.org/10.1016/j.cjche.2020.07.054

Alghamdi, Y. A., Peng, Z., Almutairi, Z., Alibrahim, H., Al-Alweet, F. M., Moghtaderi, B., and Doroodchi, E. (2021). Assessment of correlations for minimum fluidization velocity of binary mixtures of particles in gas fluidized beds. *Powder Technology*, *394*, 1231–1239.

Alobaid, F., Almohammed, N., Farid, M. M., May, J., Rößger, P., Richter, A., and Epple, B. (2021). Progress in CFD Simulations of Fluidized Beds for Chemical and Energy Process Engineering. *Progress in Energy and Combustion Science*, 100930.

Armstrong, L. M., Gu, S., and Luo, K. H. (2010). Study of wall-to-bed heat transfer in a bubbling fluidised bed using the kinetic theory of granular flow. *International Journal of Heat and Mass Transfer*, *53*(21–22), 4949–4959.

Ayub, H. M. U., Park, S. J., and Binns, M. (2020). Biomass to syngas: Modified stoichiometric thermodynamic models for downdraft biomass gasification. *Energies*, *13*(20). https://doi.org/10.3390/en13205383

Azad, A. K., Rasul, M., Khan, M. M., and Sharma, S. (2017). Macadamia biodiesel as a sustainable and alternative transport fuel in Australia. *Energy Procedia*, *110*, 543–548.

Bandason, W., Parwada, C., and Mushunje, A. (2022). Macadamia Nuts (Macadamia integrifolia) Value Chain and Technical Efficiency among the Small-scale Farmers in Zimbabwe. *Research on World Agricultural Economy*, *3*(4), 25–35. https://doi.org/10.36956/rwae. v3i4.700

Basu, P. (2006). *Combustion and gasification in fluidized beds*. CRC press.

Betiku, E., and Taiwo, A. E. (2015). Modeling and optimization of bioethanol production from breadfruit starch hydrolyzate vis-à-vis response surface methodology and artificial neural network. *Renewable Energy*, *74*, 87–94.

Bhattacharya, S. C., and Abdul Salam, P. (2002). Low greenhouse gas biomass options for cooking in the developing countries. *Biomass and Bioenergy*, *22*(4), 305–317. https://doi.org/10.1016/S0961-9534(02)00008-9

Bhusare, V. H., Dhiman, M. K., Kalaga, D. V., Roy, S., and Joshi, J. B. (2017). CFD simulations of a bubble column with and without internals by using OpenFOAM. *Chemical Engineering Journal*, *317*, 157–174. https://doi.org/10.1016/j.cej.2017.01.128.

Bonilla, J., and Gordillo, G. (2017). Adiabatic Fixed-Bed Gasification of Colombian Coffee Husk Using Air-Steam Blends for Partial Oxidation. *Journal of Combustion*, *2017*.

https://doi.org/10.1155/2017/3576509

Bonilla, J., Gordillo, G., and Cantor, C. (2019). Experimental Gasification of Coffee Husk Using Pure Oxygen-Steam Blends. *Frontiers in Energy Research*, *7*(November), 1–11. https://doi.org/10.3389/fenrg.2019.00127

Bustamante, F., Enick, R. M., Cugini, A. V, Killmeyer, R. P., Howard, B. H., Rothenberger, K. S., Ciocco, M. V, Morreale, B. D., Chattopadhyay, S., and Shi, S. (2004). High-temperature kinetics of the homogeneous reverse water–gas shift reaction. *AIChE Journal*, *50*(5), 1028–1041.

Cai, J., and Liu, R. (2007). Research on water evaporation in the process of biomass pyrolysis. *Energy & Fuels*, *21*(6), 3695–3697.

Cammarata, L., Lettieri, P., Micale, G. D. M., and Colman, D. (2003). 2D and 3D CFD simulations of bubbling fluidized beds using Eulerian-Eulerian models. *International Journal of Chemical Reactor Engineering*, *1*(1).

Cavalaglio, G., Cotana, F., Nicolini, A., Coccia, V., Petrozzi, A., Formica, A., and Bertini, A. (2020). Characterization of various biomass feedstock suitable for small-scale energy plants as preliminary activity of biocheaper project. *Sustainability (Switzerland)*, *12*(16), 1–10. https://doi.org/10.3390/su12166678

Chalermsinsuwan, B., Li, Y. H., and Manatura, K. (2023). Optimization of gasification process parameters for COVID-19 medical masks using response surface methodology. *Alexandria Engineering Journal*, *62*, 335–347. https://doi.org/10.1016/j.aej.2022.07.037

Chang, J., Wang, G., Gao, J., Zhang, K., Chen, H., and Yang, Y. (2012). CFD modeling of particle – particle heat transfer in dense gas-solid fl uidized beds of binary mixture. *Powder Technology, 217,* 50–60. https://doi.org/10.1016/j.powtec.2011.10.008

Chang, Y. M., Chou, C. M., Su, K. T., Hung, C. Y., and Wu, C. H. (2005). Elutriation characteristics of fine particles from bubbling fluidized bed incineration for sludge cake treatment. *Waste Management*, *25*(3), 249–263. https://doi.org/10.1016/j.wasman.2004.08.013

Chirone, R., Poletto, M., Barletta, D., and Lettieri, P. (2020). The effect of temperature on the minimum fluidization conditions of industrial cohesive particles. *Powder Technology, 362*, 307–322. https://doi.org/10.1016/j.powtec.2019.11.102

Choi, Y. C., Li, X. Y., Park, T. J., Kim, J. H., and Lee, J. G. (2001). Numerical study on the coal gasification characteristics in an entrained flow coal gasifier. *Fuel, 80*(15), 2193–2201.

Cortazar, M., Santamaria, L., Lopez, G., Alvarez, J., Zhang, L., Wang, R., Bi, X., and Olazar, M. (2023). A comprehensive review of primary strategies for tar removal in biomass gasification. *Energy Conversion and Management*, *276*, 116496.

Demirbas, A. (2004). Combustion characteristics of different biomass fuels. *Progress in Energy and Combustion Science*, *30*(2), 219–230.

Din, Z. U., and Zainal, Z. A. (2016). Biomass integrated gasification–SOFC systems: Technology overview. *Renewable and Sustainable Energy Reviews*, *53*, 1356–1376.

Doherty, W., Reynolds, A., and Kennedy, D. (2009). The effect of air preheating in a biomass CFB gasifier using ASPEN Plus simulation. *Biomass and Bioenergy*, *33*(9), 1158–1167. https://doi.org/10.1016/j.biombioe.2009.05.004

Dos Santos, D. A., Baluni, S., and Bück, A. (2020). Eulerian multiphase simulation of the particle dynamics in a fluidized bed opposed gas jet mill. *Processes*, *8*(12), 1–19. https://doi.org/10.3390/pr8121621

Dufour, A., Celzard, A., Fierro, V., Martin, E., Broust, F., and Zoulalian, A. (2008). Catalytic decomposition of methane over a wood char concurrently activated by a pyrolysis gas. *Applied Catalysis A: General*, *346*(1–2), 164–173.

Ehsani, M., Movahedirad, S., Shahhosseini, S., and Ashtiani, M. (2015). Effects of Restitution and Specularity Coefficients on Solid-Liquid Fluidized Bed Hydrodynamics. *Chemical Engineering & Technology*, *38*(10), 1827–1836.

Eikeland, M. S., Thapa, R. K., and Halvorsen, B. M. (2015). Aspen Plus Simulation of Biomass Gasification with Known Reaction Kinetic. *Proceedings of the 56th Conference on*

Simulation and Modelling (SIMS 56), October, 7-9, 2015, Linköping University, Sweden, *119*, 149–156. https://doi.org/10.3384/ecp15119149

Ependi, D. R., Saleh, A. R., and Sudarmanta, B. (2019). The Experimental Study of The Effect of Air Preheating in MSW Pellet Multi-Stage Downdraft Gasifier. *IPTEK The Journal for Technology and Science*, *30*(2), 36. https://doi.org/10.12962/j20882033.v30i2.5005

Escudero, D., and Heindel, T. J. (2011). Bed height and material density effects on fluidized bed hydrodynamics. *Chemical Engineering Science*, *66*(16), 3648–3655.

Esfe, M. H., Hajmohammad, H., Moradi, R., and Arani, A. A. A. (2017). Multi-objective optimization of cost and thermal performance of double walled carbon nanotubes/water nanofluids by NSGA-II using response surface method. *Applied Thermal Engineering*, *112*, 1648–1657.

Eslami Afrooz, I., Sinnathambi, C. M., Karuppanan, S., Ling, D., and Ching, C. (2016). *CFD Simulation of Bubbling Fluidized Bed: Effect of Distributor Plate Orifice Pattern Configuration on Hydrodynamics of Gas-Solid Mixing*. *11*(20). www.arpnjournals.com

Etim, A. O., Jisieike, C. F., Ibrahim, T. H., and Betiku, E. (2022). Biodiesel and its properties. In *Production of Biodiesel from Non-Edible Sources* (pp. 39–79). Elsevier.

Fair, J. R. C. W. R. P. J. R., and Walas, S. M. (2012). *Chemical Procces Equipment*.

Falciglia, P. P., Mancuso, G., Scandura, P., and Vagliasindi, F. G. A. (2015). Effective decontamination of low dielectric hydrocarbon-polluted soils using microwave heating: Experimental investigation and modelling for in situ treatment. *Separation and Purification Technology*, *156*, 480–488. https://doi.org/10.1016/j.seppur.2015.10.038

Fang, S., Wei, Y., Fu, L., Tian, G., and Qu, H. (2020). Modeling of the minimum fluidization velocity and the incipient fluidization pressure drop in a conical fluidized bed with negative pressure. *Applied Sciences (Switzerland)*, *10*(24), 1–19. https://doi.org/10.3390/app10248764

Fryda, L. E., Panopoulos, K. D., and Kakaras, E. (2008). Agglomeration in fluidised bed gasification of biomass. *Powder Technology*, *181*(3), 307–320.

https://doi.org/10.1016/j.powtec.2007.05.022

Fu, Z., Zhu, J., Barghi, S., Zhao, Y., Luo, Z., and Duan, C. (2019). Minimum fluidization velocity of binary mixtures of medium particles in the air dense medium fluidized bed. *Chemical Engineering Science*, *207*, 194–201.

Ganesh, A., Yang, Y. Bin, Ryu, C., Khor, A., Yates, N. E., Sharifi, V. N., Swithenbank, J., Science, P., Resources, N., Banos, L., Pellets, S. F., Chen, P. Y. S., Workman, E. C., Service, F., and Lenka, R. (1990). Characterization of The Properties of Some Biomass Species and Estimation of Their Power Generation Potentials Master of Technology Characterization of The Properties of Some Biomass Species and Estimation of Their. *Fuel*, *6*(16), 2116–2130.

Ghaly, A., Ergudenler, A., and Ramakrishnan, V. (2015). Effect of Distributor Plate Configuration on Pressure Drop in a Bubbling Fluidized Bed Reactor. *Advances in Research*, *3*(3), 251–268. https://doi.org/10.9734/air/2015/8240

Glushkov, D., Nyashina, G., Shvets, A., Pereira, A., and Ramanathan, A. (2021). Current status of the pyrolysis and gasification mechanism of biomass. *Energies*, *14*(22). https://doi.org/10.3390/en14227541

Glushkov, D. O., Nyashina, G. S., Anand, R., and Strizhak, P. A. (2021). Composition of gas produced from the direct combustion and pyrolysis of biomass. *Process Safety and Environmental Protection*, *156*, 43–56.

Gómez-Barea, A., and Leckner, B. (2010). Modeling of biomass gasification in fluidized bed. *Progress in Energy and Combustion Science*, *36*(4), 444–509. https://doi.org/10.1016/j.pecs.2009.12.002

Gonzalez, A. M., Lora, E. E. S., Palacio, J. C. E., and del Olmo, O. A. A. (2018). Hydrogen production from oil sludge gasification/biomass mixtures and potential use in hydrotreatment processes. *International Journal of Hydrogen Energy*, *43*(16), 7808–7822.

Gosavi, S., Kulkarni, N., Mathpati, C. S., and Mandal, D. (2018). CFD modeling to determine the minimum fluidization velocity of particles in gas-solid fluidized bed at different temperatures. *Powder Technology*, *327,* 109–119. https://doi.org/10.1016/j.powtec.2017.12.026

Grace, J. R., Bi, X., and Ellis, N. (2020). *Essentials of fluidization technology*. John Wiley & Sons.

Greenshields, C. J. (2015). OpenFOAM user guide. *OpenFOAM Foundation Ltd, Version*, *3*(1), 47.

Guo, S., Wei, X., Che, D., Liu, H., and Sun, B. (2021). Experimental study on influence of operating parameters on tar components from corn straw gasification in fluidized bed. *Frontiers in Energy*, *15*, 374–383.

Haydary, J. (2019). Chemical Process Design and Aspen Plus and Aspen HYSYS Applications. In *General Procedure for Process Simulation*.

Holzinger, G. (2020). *OpenFOAM A little User-Manual*. http://www.k1-met.com

Hulme, I., Clavelle, E., Van Der Lee, L., and Kantzas, A. (2005). CFD modeling and validation of bubble properties for a bubbling fluidized bed. *Industrial and Engineering Chemistry Research*, *44*(12), 4254–4266. https://doi.org/10.1021/ie049837j

IEA. (2019). *Africa Energy Outlook 2019 - Analysis and key findings. A report by the International Energy Agency*. 288. www.iea.org/africa2019%0Ahttps://www.oecd-ilibrary.org/energy/africa-energy-outlook_g2120ab250-en%0Ahttps://www.iea.org/africa2019

Islam, M. W. (2020). Effect of different gasifying agents (steam, H2O2, oxygen, CO2, and air) on gasification parameters. *International Journal of Hydrogen Energy*, *45*(56), 31760–31774. https://doi.org/10.1016/j.ijhydene.2020.09.002

ISO, E. N. (2015). 16948: 2015 Solid Biofuels—Determination of Total Content of Carbon, Hydrogen and Nitrogen. *European Committee for Standardization (CEN): Brussels, Belgium*.

Issaoui, R., and Mansour, L. Ben. (2019). Experimental study of temperature effects on bubble characteristics and gas holdup in electroflotation column. *Desalination and Water Treatment*, *162*, 186–192. https://doi.org/10.5004/dwt.2019.24407

Janajreh, I., and Al Shrah, M. (2013). Numerical and experimental investigation of downdraft gasification of wood chips. *Energy Conversion and Management*, *65*, 783–792. https://doi.org/10.1016/j.enconman.2012.03.009

Jayathilake, R., and Rudra, S. (2017). Numerical and experimental investigation of equivalence ratio (ER) and feedstock particle size on birchwood gasification. *Energies*, *10*(8). https://doi.org/10.3390/en10081232

Kabeyi, M. J. B., and Olanrewaju, O. A. (2022). Biogas Production and Applications in the Sustainable Energy Transition. *Journal of Energy*, *2022*, 1–43. https://doi.org/10.1155/2022/8750221

Kabir Ahmad, R., Anwar Sulaiman, S., Yusup, S., Sham Dol, S., Inayat, M., and Aminu Umar, H. (2022a). Exploring the potential of coconut shell biomass for charcoal production. *Ain Shams Engineering Journal*, *13*(1), 101499. https://doi.org/10.1016/j.asej.2021.05.013

Kabir Ahmad, R., Anwar Sulaiman, S., Yusup, S., Sham Dol, S., Inayat, M., and Aminu Umar, H. (2022b). Exploring the potential of coconut shell biomass for charcoal production. *Ain Shams Engineering Journal*, *13*(1), 101499. https://doi.org/10.1016/j.asej.2021.05.013

Koerich, D. M., Lopes, G. C., and Rosa, L. M. (2020). Numerical study on the hydrodynamics of a fluidized-bed of bioparticles in tapered bioreactors with square shape cross-section. In *Brazilian Journal of Chemical Engineering* (Vol. 37, Issue 1, pp. 101–115). https://doi.org/10.1007/s43153-020-00010-4

Komarova, E., Guhl, S., and Meyer, B. (2015). Brown coal char CO2-gasification kinetics with respect to the char structure. Part I: Char structure development. *Fuel*, *152*, 38–47. https://doi.org/10.1016/j.fuel.2015.01.107

Kombe, E. Y., Lang’at, N., Njogu, P., Malessa, R., Weber, C.-T., Njoka, F., and Krause, U. (2022). Process modeling and evaluation of optimal operating conditions for production of hydrogen-rich syngas from air gasification of rice husks using aspen plus and response surface methodology. *Bioresource Technology*, *361*, 127734.

Kreith, F., and Manglik, R. M. (2016). *Principles of heat transfer*. Cengage learning.

Kumar, A., Jones, D. D., and Hanna, M. A. (2009). Thermochemical biomass gasification: a review of the current status of the technology. *Energies*, *2*(3), 556–581.

Kumar, U., and Agarwal, V. K. (2017). Simulation of 3D gas–solid fluidized bed reactor hydrodynamics. *Particulate Science and Technology*, *35*(1), 1–13. https://doi.org/10.1080/02726351.2015.1119227

Kumar, U., and Paul, M. C. (2019). CFD modelling of biomass gasification with a volatile break-up approach. *Chemical Engineering Science*, *September*, 413–422. https://doi.org/10.1016/j.ces.2018.09.038

Li, X., Jaworski, A. J., and Mao, X. (2018). Comparative study of two non-intrusive measurement methods for bubbling gas-solids fluidized beds: Electrical capacitance tomography and pressure fluctuations. *Flow Measurement and Instrumentation*, *62*, 255–268. https://doi.org/10.1016/j.flowmeasinst.2017.08.002

Libra, J. A., Ro, K. S., Kammann, C., Funke, A., Berge, N. D., Neubauer, Y., Titirici, M.-M., Fühner, C., Bens, O., and Kern, J. (2011). Hydrothermal carbonization of biomass residuals: a comparative review of the chemistry, processes and applications of wet and dry pyrolysis. *Biofuels*, *2*(1), 71–106.

Lindgren, J. (2016). *Renewable energy scenarios for South Karelia–non-industrial energy demands*.

Linh, V. N., Van Dong, N., and Nam, N. H. (2021). Investigation on gasification of agricultural wastes: the case of macadamia husk. *Vietnam Journal of Chemistry*, *59*(5), 599–605. https://doi.org/10.1002/vjch.202100011

Liu, L., Huang, Y., Cao, J., Liu, C., Dong, L., Xu, L., and Zha, J. (2018). Experimental study of biomass gasification with oxygen-enriched air in fluidized bed gasifier. *Science of the Total Environment*, *626*, 423–433. https://doi.org/10.1016/j.scitotenv.2018.01.016

Loha, C., Chattopadhyay, H., and Chatterjee, P. K. (2012). Assessment of drag models in simulating bubbling fluidized bed hydrodynamics. *Chemical Engineering Science*, *75*, 400–407. https://doi.org/10.1016/j.ces.2012.03.044

Loha, C., Chattopadhyay, H., and Chatterjee, P. K. (2013). Euler-Euler CFD modeling of fluidized bed: Influence of specularity coefficient on hydrodynamic behavior. *Particuology*, *11*(6), 673–680. https://doi.org/10.1016/j.partic.2012.08.007

Loha, C., Chattopadhyay, H., and Chatterjee, P. K. (2014). Effect of coefficient of restitution in Euler-Euler CFD simulation of fluidized-bed hydrodynamics. *Particuology*, *15*, 170–177. https://doi.org/10.1016/j.partic.2013.07.001

Lv, X., Xiao, J., Shen, L., and Zhou, Y. (2016). Experimental study on the optimization of parameters during biomass pyrolysis and char gasification for hydrogen-rich gas. In *International Journal of Hydrogen Energy* (Vol. 41, Issue 47, pp. 21913–21925). https://doi.org/10.1016/j.ijhydene.2016.09.200

Ma, S., Song, Y., Liu, J., Kang, X., and Yue, Z. Q. (2023). Extended wet sieving method for determination of complete particle size distribution of general soils. *Journal of Rock Mechanics and Geotechnical Engineering*, *xxxx*. https://doi.org/10.1016/j.jrmge.2023.03.006

Machedi, S., Ejidike, I. P., Mtunzi, F. M., Pakade, V. E., and Klink, M. J. (2019). Chlorinated phenols sorption performance by macadamia activated carbon and grafted macadamia activated carbon: characterization, kinetics, and thermodynamic studies. *Oriental Journal of Chemistry*, *35*(5), 1469–1479.

Mahinpey, N., Vejahati, F., and Ellis, N. (2007). CFD simulation of gas-solid bubbling fluidized bed: An extensive assessment of drag models. *WIT Transactions on Engineering Sciences*, *56*, 51–60. https://doi.org/10.2495/MPF070061

Mandal, D., Sathiyamoorthy, D., and Vinjamur, M. (2013). Void fraction and effective thermal conductivity of binary particulate bed. *Fusion Engineering and Design*, *88*(4), 216–225. https://doi.org/10.1016/j.fusengdes.2013.02.033

Marcantonio, V., Bocci, E., Ouweltjes, J. P., Del Zotto, L., and Monarca, D. (2020). Evaluation of sorbents for high temperature removal of tars, hydrogen sulphide, hydrogen chloride and ammonia from biomass-derived syngas by using Aspen Plus. *International Journal of Hydrogen Energy*, *45*(11), 6651–6662. https://doi.org/10.1016/j.ijhydene.2019.12.142

Marchelli, F., Hou, Q., Bosio, B., Arato, E., and Yu, A. (2020). Comparison of different drag models in CFD-DEM simulations of spouted beds. *Powder Technology*, *360*, 1253–1270. https://doi.org/10.1016/j.powtec.2019.10.058

Mathiesen, V., Solberg, T., and Hjertager, B. H. (2000). An experimental and computational study of multiphase flow behavior in a circulating fluidized bed. *International Journal of Multiphase Flow*, *26*(3), 387–419. https://doi.org/10.1016/S0301-9322(99)00027-0

Mirmoshtaghi, G., Skvaril, J., Campana, P. E., Li, H., Thorin, E., and Dahlquist, E. (2016). The influence of different parameters on biomass gasification in circulating fluidized bed gasifiers. *Energy Conversion and Management*, *126*, 110–123. https://doi.org/10.1016/j.enconman.2016.07.031

Mohammed, M. A. A., Salmiaton, A., Azlina, W. A. K. G. W., Amran, M. S. M., and Fakhru, A. (2011). Air gasification of empty fruit bunch for hydrogen-rich gas production in a fluidized-bed reactor. *Energy Conversion and Management*, *52*(2), 1555–1561. https://doi.org/10.1016/j.enconman.2010.10.023

Mojaver, P., Khalilarya, S., and Chitsaz, A. (2019). Multi-objective optimization using response surface methodology and exergy analysis of a novel integrated biomass gasification, solid oxide fuel cell and high-temperature sodium heat pipe system. *Applied Thermal Engineering*, *156*, 627–639. https://doi.org/10.1016/j.applthermaleng.2019.04.104

Molino, A., Chianese, S., and Musmarra, D. (2016). Biomass gasification technology: The state of the art overview. *Journal of Energy Chemistry*, *25*(1), 10–25.

Mori, S., and Moriyama, A. (1978). Criteria for uniform fluidization of non-aggregative particles. *Int. Chem. Eng.;(United States)*, *18*(2).

Mostafaei, M., Javadikia, H., and Naderloo, L. (2016). Modeling the effects of ultrasound power and reactor dimension on the biodiesel production yield: Comparison of prediction abilities between response surface methodology (RSM) and adaptive neuro-fuzzy inference system (ANFIS). *Energy*, *115*, 626–636.

Motta, I. L., Miranda, N. T., Maciel Filho, R., and Wolf Maciel, M. R. (2018). Biomass gasification in fluidized beds: A review of biomass moisture content and operating pressure effects. *Renewable and Sustainable Energy Reviews*, *94*(June), 998–1023. https://doi.org/10.1016/j.rser.2018.06.042

Mustafa, A., Calay, R. K., and Mustafa, M. Y. (2017). A Techno-economic Study of a Biomass Gasification Plant for the Production of Transport Biofuel for Small Communities. *Energy Procedia*, *112*(October 2016), 529–536. https://doi.org/10.1016/j.egypro.2017.03.1111

Naryanto, R. F., Enomoto, H., Cong, A. V., Fukadu, K., Zong, Z., Delimayanti, M. K., Chunti, C., and Noda, R. (2020). The effect of moisture content on the tar characteristic of wood pellet feedstock in a downdraft gasifier. *Applied Sciences (Switzerland)*, *10*(8). https://doi.org/10.3390/APP10082760

Nazari, L., Yuan, Z., Ray, M. B., and Xu, C. (Charles). (2017). Co-conversion of waste activated sludge and sawdust through hydrothermal liquefaction: Optimization of reaction parameters using response surface methodology. *Applied Energy*, *203*, 1–10. https://doi.org/10.1016/j.apenergy.2017.06.009

Nemati, N., Zarghami, R., and Mostoufi, N. (2016). Investigation of Hydrodynamics of High-Temperature Fluidized Beds by Pressure Fluctuations. *Chemical Engineering and Technology*, *39*(8), 1527–1536. https://doi.org/10.1002/ceat.201500443

Neves, D., Thunman, H., Matos, A., Tarelho, L., and Gómez-Barea, A. (2011). Characterization and prediction of biomass pyrolysis products. *Progress in Energy and Combustion Science*, *37*(5), 611–630. https://doi.org/10.1016/j.pecs.2011.01.001

Ngamchompoo, W., and Triratanasirichai, K. (2017). Experimental investigation of high temperature air and steam biomass gasification in a fixed-bed downdraft gasifier. *Energy Sources, Part A: Recovery, Utilization and Environmental Effects*, *39*(8), 733–740. https://doi.org/10.1080/15567036.2013.783657

Ngo, S. I., Lim, Y. Il, Lee, D., and Seo, M. W. (2021). Flow behavior and heat transfer in bubbling fluidized-bed with immersed heat exchange tubes for CO2 methanation. *Powder Technology*, *380*, 462–474. https://doi.org/10.1016/j.powtec.2020.11.027

Njogu, P., Kinyua, R., Muthoni, P., and Nemoto, Y. (2015). Thermal gasification of rice husks from rice growing areas in Mwea, Embu County, Kenya. *Smart Grid and Renewable Energy*, *6*(05), 113.

Njuguna, F. I., Ndiritu, H. M., Gathitu, B. B., Hawi, M., and Munyalo, J. M. (2023). Experimental investigation and optimization of the gasification parameters of macadamia nutshells in a batch-fed bubbling fluidized bed gasifier with air preheating. *Energy Storage and Saving*. https://doi.org/10.1016/j.enss.2023.07.001

Njuguna, F., Ndiritu, H., Gathitu, B., Hawi, M., and Munyalo, J. (2023). Bioresource Technology Reports Kinetic modeling and optimization of process parameters for gasification of macadamia nutshells with air preheating : A combined use of Aspen Plus and response surface methodology (RSM). *Bioresource Technology Reports*, *22*(March), 101477. https://doi.org/10.1016/j.biteb.2023.101477

Nkosi, N., Muzenda, E., Gorimbo, J., and Belaid, M. (2021). Developments in waste tyre thermochemical conversion processes: gasification, pyrolysis and liquefaction. *RSC Advances*, *11*(20), 11844–11871.

Okati, A., Khani, M. R., Shokri, B., Rouboa, A., and Monteiro, E. (2022). Optimizing the operating conditions for hydrogen-rich syngas production in a plasma co-gasification process of municipal solid waste and coal using Aspen Plus. *International Journal of Hydrogen Energy*, *47*(63), 26891–26900.

Onay, Ö., Beis, S. H., and Koçkar, Ö. M. (2004). Pyrolysis of walnut shell in a well-swept fixed-bed reactor. *Energy Sources*, *26*(8), 771–782. https://doi.org/10.1080/00908310490451402

Ostermeier, P., Fischer, F., Fendt, S., DeYoung, S., and Spliethoff, H. (2019). Coarse-grained CFD-DEM simulation of biomass gasification in a fluidized bed reactor. *Fuel*, *255*(June), 115790. https://doi.org/10.1016/j.fuel.2019.115790

Pala, L. P. R., Wang, Q., Kolb, G., and Hessel, V. (2017). Steam gasification of biomass with subsequent syngas adjustment using shift reaction for syngas production: An Aspen Plus model. *Renewable Energy*, *101*, 484–492. https://doi.org/10.1016/j.renene.2016.08.069

Park, S. W., Lee, S. Y., Jeong, Y. O., Han, G. H., and Seo, Y. C. (2018). Effects of Oxygen Enrichment in Air Oxidants on Biomass Gasification Efficiency and the Reduction of Tar Emissions. *Energies*, *11*(10). https://doi.org/10.3390/en11102664

Parthasarathy, P., and Narayanan, S. K. (2014). Effect of Hydrothermal Carbonization Reaction Parameters on. *Environmental Progress & Sustainable Energy*, *33*(3), 676–680. https://doi.org/10.1002/ep

Pio, D. T., Tarelho, L. A. C., and Matos, M. A. A. (2016). Characteristics of the gas produced during biomass direct gasification in an autothermal pilot-scale bubbling fluidized bed reactor. *Energy*. https://doi.org/10.1016/j.energy.2016.11.145

Puig-Gamero, M., Argudo-Santamaria, J., Valverde, J. L., Sánchez, P., and Sanchez-Silva, L. (2018). Three integrated process simulation using aspen plus®: Pine gasification, syngas cleaning and methanol synthesis. *Energy Conversion and Management*, *177*(September), 416–427. https://doi.org/10.1016/j.enconman.2018.09.088

Puig-Gamero, M., Pio, D. T., Tarelho, L. A. C., Sánchez, P., and Sanchez-Silva, L. (2021). Simulation of biomass gasification in bubbling fluidized bed reactor using aspen plus®. *Energy Conversion and Management*, *235*. https://doi.org/10.1016/j.enconman.2021.113981

Qizilbash, M., and Malik, & S. R. (2015). *Effect of Aspect Ratio, Tubular Assembly and Materials on Minimum Fluidization Velocity in 3D-Atmospheric Fluidized Bed*.

Rasteh, M., Farhadi, F., and Ahmadi, G. (2018). Empirical models for minimum fluidization velocity of particles with different size distribution in tapered fluidized beds. *Powder Technology*, *338*, 563–575. https://doi.org/10.1016/j.powtec.2018.07.077

Ren, R., Wang, H., and You, C. (2022). Steam Gasification of Refuse-Derived Fuel with CaO Modification for Hydrogen-Rich Syngas Production. *Energies*, *15*(21), 1–16. https://doi.org/10.3390/en15218279

Reyes-Urrutia, A., Venier, C., Mariani, N. J., Nigro, N., Rodriguez, R., and Mazza, G. (2022). A CFD comparative study of bubbling fluidized bed behavior with thermal effects using the open-source platforms mfix and openfoam. *Fluids*, *7*(1). https://doi.org/10.3390/fluids 7010001

Rong, W., Feng, Y., Schwarz, P., Witt, P., Li, B., Song, T., and Zhou, J. (2020a). Numerical study of the solid flow behavior in a rotating drum based on a multiphase CFD model accounting for solid frictional viscosity and wall friction. *Powder Technology*, *361*, 87–98. https://doi.org/10.1016/j.powtec.2019.10.034

Rong, W., Feng, Y., Schwarz, P., Witt, P., Li, B., Song, T., and Zhou, J. (2020b). Numerical study of the solid flow behavior in a rotating drum based on a multiphase CFD model accounting for solid frictional viscosity and wall friction. *Powder Technology*, *361*, 87–98. https://doi.org/10.1016/j.powtec.2019.10.034

Safarian, S., Rydén, M., and Janssen, M. (2022). Development and Comparison of Thermodynamic Equilibrium and Kinetic Approaches for Biomass Pyrolysis Modeling. *Energies*, *15*(11). https://doi.org/10.3390/en15113999

Sait, H. H., Hussain, A., Salema, A. A., and Ani, F. N. (2012). Pyrolysis and combustion kinetics of date palm biomass using thermogravimetric analysis. *Bioresource Technology*, *118*, 382–389.

Saleh, S., and Samad, N. A. F. A. (2021). Effects of Gasification Temperature and Equivalence Ratio on Gasification Performance and Tar Generation of Air Fluidized Bed Gasification Using Raw and Torrefied Empty Fruit Bunch. *Chemical Engineering Transactions*, *88*(October), 1309–1314. https://doi.org/10.3303/CET2188218

Samaksaman, U., Pattaraprakorn, W., Neramittagapong, A., and Kanchanatip, E. (2023). Solid fuel production from macadamia nut shell: effect of hydrothermal carbonization conditions on fuel characteristics. *Biomass Conversion and Biorefinery*, *13*(3), 2225–2232. https://doi.org/10.1007/s13399-021-01330-2

Samiran, N. A., Jaafar, M. N. M., Ng, J. H., Lam, S. S., and Chong, C. T. (2016). Progress in biomass gasification technique - With focus on Malaysian palm biomass for syngas production. *Renewable and Sustainable Energy Reviews*, *62*, 1047–1062. https://doi.org/10.1016/j.rser.2016.04.049

Sánchez-Prieto, J., Soria-Verdugo, A., Briongos, J. V., and Santana, D. (2014). The effect of temperature on the distributor design in bubbling fluidized beds. *Powder Technology*, *261*, 176–184. https://doi.org/10.1016/j.powtec.2014.04.035

Sansaniwal, S. K., Pal, K., Rosen, M. A., and Tyagi, S. K. (2017). Recent advances in the development of biomass gasification technology: A comprehensive review. *Renewable and Sustainable Energy Reviews*, *72*, 363–384.

Sathiyamoorthy, D., and Horio, M. (2003). On the influence of aspect ratio and distributor in gas fluidized beds. *Chemical Engineering Journal*, *93*(2), 151–161. https://doi.org/10.1016/S1385-8947(02)00257-7

Savuto, E., Di Carlo, A., Gallucci, K., Stendardo, S., and Rapagnà, S. (2019). 3D-CFD simulation of catalytic filter candles for particulate abatement and tar and methane steam reforming inside the freeboard of a gasifier. *Chemical Engineering Journal*, *377*. https://doi.org/10.1016/j.cej.2018.10.227

Sengupta, D., Samburova, V., Bhattarai, C., Moosmüller, H., and Khlystov, A. (2023). Emission factors for polycyclic aromatic hydrocarbons from laboratory biomass-burning and their chemical transformations during aging in an oxidation flow reactor. *Science of The Total Environment*, *870*, 161857.

Shah, M., Agrawal, V., Shinde, Y., and ... (2017). Experiments of Bubbling Fluidized Bed using ECVT Measurements. *One Curtin ...*, *December 2017*, 6–11. https://espace.curtin.edu.au/handle/20.500.11937/75933

Shao, Y., Gu, J., Zhong, W., and Yu, A. (2019). Determination of minimum fluidization velocity in fluidized bed at elevated pressures and temperatures using CFD simulations. *Powder Technology*, *350*, 81–90. https://doi.org/10.1016/j.powtec.2019.03.039

Sharma, A., and Nath, R. (2023). H 2-rich syngas production from gasification involving kinetic modeling: RSM-utility optimization and techno-economic analysis. *RSC Advances, 13*(15), 10308–10321.

Shaul, S., Rabinovich, E., and Kalman, H. (2014). Typical fluidization characteristics for Geldart's classification groups. *Particulate Science and Technology, 32*(2), 197–205.

Shi, A., Pang, Y., Xu, G., and Li, C. (2015). Numerical simulation of biomass gasification in a fluidized bed. *2015 International Conference on Applied Science and Engineering Innovation*, 1585–1591.

Shrestha, S., Gan, J. Q., and Zhou, Z. Y. (2019). Micromechanical analysis of bubbles formed in fluidized beds operated with a continuous single jet. *Powder Technology*, *357*, 398–407. https://doi.org/10.1016/j.powtec.2019.08.091

Shukrullah, S., Javed, M. A., Naz, M. Y., Khan, Y., Alkanhal, M. A. S., and Anwar, H. (2019). PIV and statistical analysis of a swirling bed process carried out using a hybrid model of axial blade distributor. *Processes*, *7*(10). https://doi.org/10.3390/pr7100697

Simulation, H. (2010). *Hydrodynamic Simulation of Cyclone Separators*. *January*.

Singh, D. K., and Tirkey, J. V. (2021). Modeling and multi-objective optimization of variable air gasification performance parameters using Syzygium cumini biomass by integrating ASPEN Plus with Response surface methodology (RSM). *International Journal of Hydrogen Energy*, *46*(36), 18816–18831. https://doi.org/10.1016/j.ijhydene.2021.03.054

Singh, D., Yadav, S., Rajesh, V. M., and Mohanty, P. (2019). Groundnut shell gasification performance in a fluidized bed gasifier with bubbling air as gasification medium. *Environmental Technology (United Kingdom)*, *40*(24), 3140–3152. https://doi.org/ 10.1080/ 09593330.2018.1476592

Subramani, H. J., Mothivel Balaiyya, M. B., and Miranda, L. R. (2007). Minimum fluidization velocity at elevated temperatures for Geldart's group-B powders. *Experimental Thermal and Fluid Science*, *32*(1), 166–173. https://doi.org/10.1016/j.expthermflusci.2007.03.003

Sun, J., and Yan, Y. (2016). Non-intrusive measurement and hydrodynamics characterization of gas-solid fluidized beds: A review. *Measurement Science and Technology*, *27*(11), 112001. https://doi.org/10.1088/0957-0233/27/11/112001

Szul, M., Głód, K., and Iluk, T. (2021). Influence of pressure and CO2 in fluidized bed gasification of waste biomasses. *Biomass Conversion and Biorefinery*, *11*(1), 69–81. https://doi.org/10.1007/s13399-020-00840-9

Timofeeva, S., and Ermolaev, D. (2022). Study of the Effect of Gasification Pressure on the Composition of the Producer Gas From Coal. *IOP Conference Series: Earth and Environmental Science*, *988*(3). https://doi.org/10.1088/1755-1315/988/3/032043

Uddin, M. H., and Coronella, C. J. (2017). Effects of grid size on predictions of bed expansion in bubbling fluidized beds of Geldart B particles: A generalized rule for a grid-independent solution of TFM simulations. *Particuology*, *34*, 61–69. https://doi.org/10.1016/j.partic. 2016.12.002

Vaezi, M., Passandideh-Fard, M., Moghiman, M., and Charmchi, M. (2011). Gasification of heavy fuel oils: A thermochemical equilibrium approach. *Fuel*, *90*(2), 878–885. https://doi.org/10.1016/j.fuel.2010.10.011

Vaquerizo, L., and Cocero, M. J. (2018). CFD–Aspen Plus interconnection method. Improving thermodynamic modeling in computational fluid dynamic simulations. *Computers and Chemical Engineering*, *113*, 152–161. https://doi.org/10.1016/j.compchemeng. 2018.03.019

Vehkalahti, K. (2010). Dealing with Uncertainties: A Guide to Error Analysis, Second Edition by Manfred Drosg. In *International Statistical Review* (Vol. 78, Issue 1). https://doi.org/10.1111/j.1751-5823.2010.00109_6.x

Vogtenhuber, H., Pernsteiner, D., and Hofmann, R. (2019). Experimental and numerical investigations on heat transfer of bare tubes in a bubbling fluidized bed with respect to better heat integration in temperature swing adsorption systems. *Energies*, *12*(14), 1–26. https://doi.org/10.3390/en12142646

Vu, N. L., Nguyen, N. D., Dinh, T. M. T., and Nguyen, H. N. (2023). Cascading use of macadamia nutshell for production of energy and adsorbents through biomass gasification. *Industrial Crops and Products, 206*, 117662.

Vullo, V. (2014). *Circular Cylinders and Pressure Vessels Stress Analysis and Design*. Springer.

Wang, J. (2009). A review of Eulerian simulation of Geldart A particles in gas-fluidized beds. *Industrial & Engineering Chemistry Research*, *48*(12), 5567–5577.

Wang, J. (2010). Flow structures inside a large-scale turbulent fluidized bed of FCC particles: Eulerian simulation with an EMMS-based sub-grid scale model. *Particuology, 8*(2), 176–185.

Wang, S., Hu, C., Luo, K., Yu, J., and Fan, J. (2023). Multi-scale numerical simulation of fluidized beds: Model applicability assessment. *Particuology*, *80*, 11–41.

Welahettige, P., Lie, B., Vaagsaether, K., and Moldestad, B. M. . (2017). Study of Fluidization Regimes using OpenFOAM Computational Fluid Dynamics. *Proceedings of the 58th Conference on Simulation and Modelling (SIMS 58) Reykjavik, Iceland, September 25th – 27th, 2017, 138*, 128–136. https://doi.org/10.3384/ecp17138128

Wu, K. T., and Chein, R. Y. (2015). Modeling of Biomass Gasification with Preheated Air at High Temperatures. *Energy Procedia*, *75*, 214–219. https://doi.org/10.1016/j.egypro.2015.07.307

Wu, Y., Yang, W., and Blasiak, W. (2014). Energy and exergy analysis of high temperature agent gasification of biomass. *Energies*, *7*(4), 2107–2122. https://doi.org/10.3390/en7042107

Xavier, T. P., Lira, T. S., Jr, M. A. S., and Barrozo, M. A. S. (2016). *A Study Of Pyrolysis Of Macadamia Nut Shell : Parametric Sensitivity Analysis of the IPR model*. *33*(01), 115–122.

Xavier, T. P., Lira, T. S., Schettino Jr, M. A., and Barrozo, M. A. S. (2016). A study of pyrolysis of macadamia nut shell: parametric sensitivity analysis of the IPR model. *Brazilian*

Journal of Chemical Engineering, *33*, 115–122.

Xie, N., Battaglia, F., and Pannala, S. (2008). Effects of using two- versus three-dimensional computational modeling of fluidized beds. Part I, hydrodynamics. *Powder Technology*, *182*(1), 1–13. https://doi.org/10.1016/j.powtec.2007.07.005

Yahya, S., Wahab, S. K. M., and Harun, F. W. (2020). Optimization of biodiesel production from waste cooking oil using Fe-Montmorillonite K10 by response surface methodology. *Renewable Energy*, *157*, 164–172.

Yu, X., Blanco, P. H., Makkawi, Y., and Bridgwater, A. V. (2018). CFD and experimental studies on a circulating fluidised bed reactor for biomass gasification. *Chemical Engineering and Processing - Process Intensification*, *130*, 284–295. https://doi.org/10.1016/j.cep. 2018.06.018

Zhao, S., Luo, Y., Zhang, Y., and Long, Y. (2015). Experimental Investigation of Tar Reduction Properties by Coupling Oxidative Pyrolysis and Partial Oxidation in a Continuous Reactor for Biomass Gasification. *Energy Technology*, *3*(11), 1101–1107. https://doi.org/10.1002/ente.201500159

Zimmermann, S., and Taghipour, F. (2005). *CFD Modeling of the Hydrodynamics and Reaction Kinetics of FCC Fluidized-Bed Reactors*. https://doi.org/10.1021/ie050490

APPENDICES

Appendix I: Experimental Measurement Instrumentation

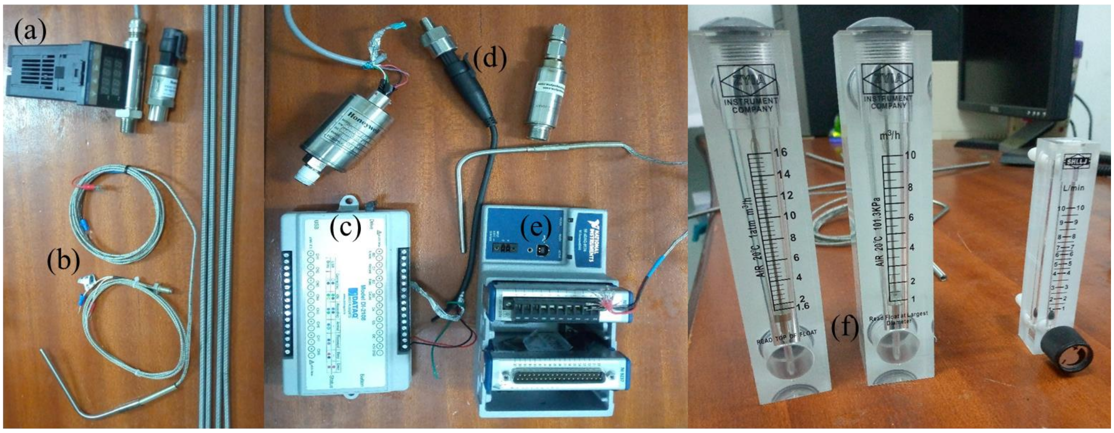

Devices: (a) PID controller, (b) thermocouples, (c) pressure data logger, (d) pressure sensors, (e) temperature data logger, (f) rotameters

Appendix II: Temperature Controllers

Appendix III: Material Entrainment at Different Fluidization Velocity Factor

Minimum fluidization velocity (m/s)	**λ**	**Superficial velocity (kg/h)**	**Material carried over**
0.125 m/s	1	5.06	None
	1.25	6.33	None
	1.5	7.59	None
	1.75	8.86	None
	2	10.13	Biomass
	2.25	11.39	Biomass
	2.75	13.92	Biomass and sand

Appendix IV: Parameters for the Fluidization Velocity Factor of 1.5

Air flow rate kg/h	ER	Air/kg-Biomass	Biomass kg/h
7.59	0.15	1.037	7.32
7.59	0.2	1.383	5.49
7.59	0.25	1.729	4.39
7.59	0.3	2.075	3.66
7.59	0.35	2.421	3.14

Appendix V: Parameters for the Fluidization Velocity Factor Of 2

Air flow rate kg/h	ER	Air/kg-Bio	Biomass kg/h
10.13	0.15	1.037	9.76
10.13	0.2	1.383	7.32
10.13	0.25	1.729	5.86
10.13	0.3	2.075	4.88
10.13	0.35	2.421	4.18

Appendix VI: Standard Allowable Stress

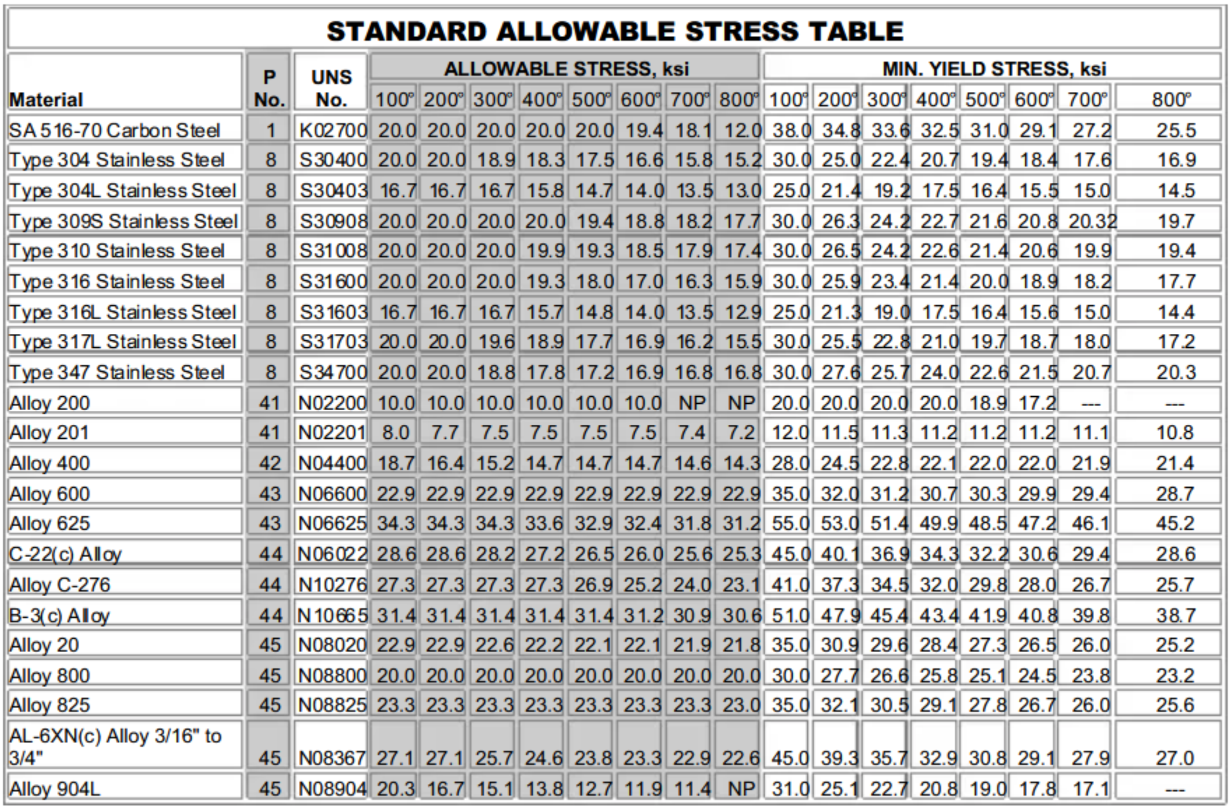

STANDARD ALLOWABLE STRESS TABLE

Material	P No.	UNS No.	ALLOWABLE STRESS, ksi								MIN. YIELD STRESS, ksi							
			100°	200°	300°	400°	500°	600°	700°	800°	100°	200°	300°	400°	500°	600°	700°	800°
SA 516-70 Carbon Steel	1	K02700	20.0	20.0	20.0	20.0	20.0	19.4	18.1	12.0	38.0	34.8	33.6	32.5	31.0	29.1	27.2	25.5
Type 304 Stainless Steel	8	S30400	20.0	20.0	18.9	18.3	17.5	16.6	15.8	15.2	30.0	25.0	22.4	20.7	19.4	18.4	17.6	16.9
Type 304L Stainless Steel	8	S30403	16.7	16.7	16.7	15.8	14.7	14.0	13.5	13.0	25.0	21.4	19.2	17.5	16.4	15.5	15.0	14.5
Type 309S Stainless Steel	8	S30908	20.0	20.0	20.0	20.0	19.4	18.8	18.2	17.7	30.0	26.3	24.2	22.7	21.6	20.8	20.32	19.7
Type 310 Stainless Steel	8	S31008	20.0	20.0	20.0	19.9	19.3	18.5	17.9	17.4	30.0	26.5	24.2	22.6	21.4	20.6	19.9	19.4
Type 316 Stainless Steel	8	S31600	20.0	20.0	20.0	19.3	18.0	17.0	16.3	15.9	30.0	25.9	23.4	21.4	20.0	18.9	18.2	17.7
Type 316L Stainless Steel	8	S31603	16.7	16.7	16.7	15.7	14.8	14.0	13.5	12.9	25.0	21.3	19.0	17.5	16.4	15.6	15.0	14.4
Type 317L Stainless Steel	8	S31703	20.0	20.0	19.6	18.9	17.7	16.9	16.2	15.5	30.0	25.5	22.8	21.0	19.7	18.7	18.0	17.2
Type 347 Stainless Steel	8	S34700	20.0	20.0	18.8	17.8	17.2	16.9	16.8	16.8	30.0	27.6	25.7	24.0	22.6	21.5	20.7	20.3
Alloy 200	41	N02200	10.0	10.0	10.0	10.0	10.0	10.0	NP	NP	20.0	20.0	20.0	20.0	18.9	17.2	---	---
Alloy 201	41	N02201	8.0	7.7	7.5	7.5	7.5	7.5	7.4	7.2	12.0	11.5	11.3	11.2	11.2	11.2	11.1	10.8
Alloy 400	42	N04400	18.7	16.4	15.2	14.7	14.7	14.7	14.6	14.3	28.0	24.5	22.8	22.1	22.0	22.0	21.9	21.4
Alloy 600	43	N06600	22.9	22.9	22.9	22.9	22.9	22.9	22.9	22.9	35.0	32.0	31.2	30.7	30.3	29.9	29.4	28.7
Alloy 625	43	N06625	34.3	34.3	34.3	33.6	32.9	32.4	31.8	31.2	55.0	53.0	51.4	49.9	48.5	47.2	46.1	45.2
C-22(c) Alloy	44	N06022	28.6	28.6	28.2	27.2	26.5	26.0	25.6	25.3	45.0	40.1	36.9	34.3	32.2	30.6	29.4	28.6
Alloy C-276	44	N10276	27.3	27.3	27.3	27.3	26.9	25.2	24.0	23.1	41.0	37.3	34.5	32.0	29.8	28.0	26.7	25.7
B-3(c) Alloy	44	N10665	31.4	31.4	31.4	31.4	31.4	31.2	30.9	30.6	51.0	47.9	45.4	43.4	41.9	40.8	39.8	38.7
Alloy 20	45	N08020	22.9	22.9	22.6	22.2	22.1	22.1	21.9	21.8	35.0	30.9	29.6	28.4	27.3	26.5	26.0	25.2
Alloy 800	45	N08800	20.0	20.0	20.0	20.0	20.0	20.0	20.0	20.0	30.0	27.7	26.6	25.8	25.1	24.5	23.8	23.2
Alloy 825	45	N08825	23.3	23.3	23.3	23.3	23.3	23.3	23.3	23.0	35.0	32.1	30.5	29.1	27.8	26.7	26.0	25.6
AL-6XN(c) Alloy 3/16" to 3/4"	45	N08367	27.1	27.1	25.7	24.6	23.8	23.3	22.9	22.6	45.0	39.3	35.7	32.9	30.8	29.1	27.9	27.0
Alloy 904L	45	N08904	20.3	16.7	15.1	13.8	12.7	11.9	11.4	NP	31.0	25.1	22.7	20.8	19.0	17.8	17.1	---